



UNIVERSITÀ DEGLI STUDI DI NAPOLI
“FEDERICO II”

TESI DI DOTTORATO
IN FISICA FONDAMENTALE ED APPLICATA
CICLO XIX

**Dynamics of $\eta \rightarrow \pi^+ \pi^- \pi^0$
with KLOE experiment**

Dr. Tiziana Capussela

Coordinator: Prof. Gennaro Miele

**Advisors: Prof. Marco Napolitano
Dr. Fabio Ambrosino**

Contents

Introduction	1
1 DAΦNE and KLOE	3
1.1 <i>CP</i> violation in the neutral kaon system	3
1.2 The DAΦNE accelerator	6
1.2.1 DAΦNE achievements	7
1.3 The KLOE experiment	9
1.3.1 The drift chamber	11
1.3.2 The electromagnetic calorimeter	13
1.4 The trigger	18
1.4.1 The EMC trigger	19
1.4.2 The DC trigger	21
1.5 The data acquisition	21
2 η physics at KLOE	25
2.1 Measurement of the ratio $Br(\phi \rightarrow \eta'\gamma)/Br(\phi \rightarrow \eta\gamma)$	25
2.2 Measurement of the branching fraction $\eta \rightarrow \pi^0 \gamma\gamma$	29
2.3 η mass measurement	30
2.4 Basics of Chiral Perturbation Theory	32
2.4.1 Chiral symmetry	33
2.4.2 Spontaneous Symmetry breaking and Effective Lagrangian	35
2.5 $\eta \rightarrow \pi^+ \pi^- \pi^0$ decay	38

2.6	Brief review of experimental and theoretical results on the Dalitz plot parameters	40
3	Reconstruction procedure and Event Classification at KLOE	43
3.1	Track reconstruction	43
3.1.1	Pattern recognition	44
3.1.2	Track fit	44
3.1.3	Vertex fit	46
3.2	Cluster reconstruction	46
3.3	The KLOE Event Classification EVCL	47
3.3.1	Stream 4: Charged/neutral radiative decays	49
3.4	Background rejection (FILFO)	51
3.5	A minimum bias EVCL filter for ϕ radiative decays	53
4	Analysis of $\eta \rightarrow \pi^+ \pi^- \pi^0$	55
4.1	Selection of $\eta \rightarrow \pi^+ \pi^- \pi^0$ decays	55
4.1.1	Selection cuts	56
4.2	Selection efficiency	58
4.3	Resolution and efficiency on Dalitz-plot variables	62
4.4	Fit of Dalitz-plot procedure	69
4.5	Results of fit on MonteCarlo	69
5	Results	73
5.1	Analysis on data	73
5.2	Results of fit on 2000 – 2001 statistics	74
5.3	Results of fit on whole statistics	76
5.3.1	Check on cubic term ' f '	80
5.4	Systematic uncertainties	84
5.4.1	Resolution and binning	84
5.4.2	Efficiency evaluation	87
5.4.3	Background contamination	93
5.4.4	Effect of EVCL procedure	96
5.4.5	Time stability	96

5.4.6 Radiative correction	98
5.5 Results	99
Conclusions	103
Appendix	105
Bibliography	118

Introduction

The KLOE experiment has completed its data taking in March 2006 at DAΦNE, the e^+e^- collider of the Laboratori Nazionali di Frascati, operating at the ϕ resonance peak ($\sqrt{s} \simeq 1020$ MeV).

DAΦNE delivered an integrated luminosity greater than 2.5 fb^{-1} on the peak of the ϕ resonance and of about 0.25 fb^{-1} off peak.

The entire KLOE data set corresponds to more than $8 \cdot 10^9$ Φ mesons. This statistics is enough to perform a considerable number of interesting physics measurements, like studies on radiative Φ decays in scalar and pseudoscalar mesons, analysis of rare kaon decays, V_{us} extraction.

In this thesis, using the decay chain:

$$\phi \rightarrow \eta\gamma \rightarrow \pi^+ \pi^- \pi^0 \rightarrow \pi^+ \pi^- 3\gamma$$

the analysis of the dynamic of $\eta \rightarrow \pi^+ \pi^- \pi^0$ decay through a fit to the Dalitz plot density distribution is reported.

The Dalitz plot is a bidimensional diagram in which the point density is proportional to the square of the transition amplitude.

The decay of the isoscalar η into three pions accours primarily due to strong isospin violation and so the decay amplitude $A_{\eta \rightarrow \pi^+ \pi^- \pi^0}$ is inversely proportional to the quark mass ratio

$$Q^2 \equiv \frac{m_s^2 - \hat{m}^2}{m_d^2 - m_u^2} \quad (1)$$

with $\hat{m} = \frac{1}{2}(m_u + m_d)$ the average of the u, d quark mass.

From a fit to the Dalitz plot density distribution we obtain a precise measurement of the slope parameters that can improve the knowledge of the decay amplitude and allows to test theoretical predictions at level of precision needed to extract the quark mass ratio from the decay rate.

This thesis is divided into five chapters.

The first chapter is dedicated to a brief description of the DAΦNE collider and of the KLOE detector. The trigger and the data acquisition system are also pointed out.

In the second chapter, a short review is given of some KLOE measurements on light meson spectroscopy based on 2001–2002 statistics. The theoretical aspects connected to the Dalitz plot distribution of the $\eta \rightarrow \pi^+ \pi^- \pi^0$ decay are described and a review of the experimental and theoretical results on the Dalitz plot parameter is given at the end of the chapter.

The third chapter provides a general description of the offline data reconstruction procedures and of the streaming algorithms used for the event classification, with more attention to the case of $\phi \rightarrow \eta \gamma$ with $\eta \rightarrow \pi^+ \pi^- \pi^0$ events.

The fourth chapter gives an accurate description of the method applied to fit the Dalitz plot density distribution. Firstly the criteria used to select $\eta \rightarrow \pi^+ \pi^- \pi^0$ decay are described and particular attention is paid in optimizing the rejection of the main sources of background.

A very large MonteCarlo sample is used to tune the cuts applied in the analysis and to evaluate the resolution and efficiency on Dalitz plot variables. The procedure of fit has been tested on MonteCarlo and the results for the fitted slope parameters are discussed.

The five chapter is devoted to the measurement of the slope parameters using the 2001–2002 statistics ($\sim 450 \text{ pb}^{-1}$) corresponding to about 1.3 millions of $\eta \rightarrow \pi^+ \pi^- \pi^0$ events in the Dalitz plot. The analysis finds evidences for an unexpected large cubic slope never measured before.

The contributions to the total errors on these parameters are discussed and quantified. Finally a comment on the obtained results is reported.

Chapter 1

DAΦNE and KLOE

The KLOE experiment [1] is located at the Frascati ϕ -factory DAΦNE. The experiment has been designed to perform precision tests on CP violation in the system of neutral kaons, in particular the primary goal was to measure $\Re\left(\frac{\epsilon'}{\epsilon}\right)$ with an accuracy of 10^{-4} .

In March 2006 has completed its data taking integrating a luminosity of $\sim 2.5 \text{ fb}^{-1}$ at the ϕ resonance peak. The entire KLOE data set corresponding to more than $10^9 \phi$ mesons is not sufficient for the measurement of $\Re\left(\frac{\epsilon'}{\epsilon}\right)$ with the desired accuracy, it allows other interesting physics measurements: rare Kaon decays, V_{us} extraction, light scalar and pseudoscalar meson decays.

In this chapter, a short description of the CP violation phenomenology and the characteristics of the DAΦNE collider and the KLOE detector are given. The trigger logic scheme and the data acquisition system are also discussed.

1.1 CP violation in the neutral kaon system

The largest part of ϕ mesons decay into pairs of charged or neutral kaons, as can be observed in tab.1.1. In 1955 Gell-Mann and Pais [3] pointed out that K^0 and \bar{K}^0 mesons are different particles in the strong interactions, but they can transform into each other by means of second-order weak interactions. The quantum state for a neutral kaon can be described by a linear combination of $|K^0\rangle$ and $|\bar{K}^0\rangle$ with

Canale	<i>BR</i>
$K^+ K^-$	$49.2 \pm 0.6 \%$
$K_L^0 K_S^0$	$34.0 \pm 0.5 \%$
$\rho\pi + \pi^+ \pi^- \pi^0$	$15.3 \pm 0.4 \%$
$\eta\gamma$	$1.301 \pm 0.024 \%$
$\pi^0\gamma$	$(1.25 \pm 0.07) \times 10^{-3}$
e^+e^-	$(2.97 \pm 0.04) \times 10^{-4}$
$\mu^+\mu^-$	$(2.86 \pm 0.19) \times 10^{-4}$
ηe^+e^-	$(1.15 \pm 0.10) \times 10^{-4}$
$\pi^+ \pi^-$	$(7.3 \pm 1.3) \times 10^{-5}$

Table 1.1: Branching ratio of principal decays of ϕ [65].

coefficients α and β , whose evolution is described by an effective 2×2 Hamiltonian:

$$i \frac{\partial}{\partial t} \begin{pmatrix} \alpha(t) \\ \beta(t) \end{pmatrix} = H \begin{pmatrix} \alpha(t) \\ \beta(t) \end{pmatrix} = \left(M - \frac{i}{2} \Gamma \right) \begin{pmatrix} \alpha(t) \\ \beta(t) \end{pmatrix} \quad (1.1)$$

where the matrices M and Γ are hermitian. By imposing CPT conservation, the masses and the decay rates have to coincide for $|K^0\rangle$ and $|\bar{K}^0\rangle$:

$$M_{11} = M_{22}, \quad \Gamma_{11} = \Gamma_{22} \quad (1.2)$$

while imposing CP conservation the matrix elements to be invariant under the exchange of the indices 1 and 2 if the phase convention such that $CP|K^0\rangle = |\bar{K}^0\rangle$ is observed, then adding:

$$M_{12} = M_{21} = M_{12}^*, \quad \Gamma_{12} = \Gamma_{21} = \Gamma_{12}^* \quad (1.3)$$

The CP invariance in the neutral kaon system can be likewise expressed independently of the phase convention as:

$$|M_{12}^* - \frac{i}{2}\Gamma_{12}^*| = |M_{12} - \frac{i}{2}\Gamma_{12}| \Leftrightarrow \arg\left(\frac{M_{12}}{\Gamma_{12}}\right) = 0 \quad (1.4)$$

If CP was conserved, the eigenstates of the Hamiltonian should be the masses (M_S and M_L) and the widths (Γ_S and Γ_L) of the K_S and the K_L physical states.

In such hypothesis, mass and CP eigenstates should be the same:

$$CP|K_{1,2}\rangle = \pm|K_{1,2}\rangle, \quad |K_{1,2}\rangle = \frac{1}{\sqrt{2}}[|K^0\rangle \pm |\bar{K}^0\rangle] \quad (1.5)$$

where the $|K_1\rangle$ is allowed to decay into 2-pion final states and $|K_2\rangle$ into 3-pion states, which are respectively even and odd CP eigenstates. In 1964 CP violation was observed [4] by measuring a fraction $\sim 2 \cdot 10^3$ of K_L mesons (supposed to be exactly the $|K_2\rangle$ state) decaying into $\pi^+\pi^-$. Therefore, mass eigenstates are obtained by mixing the $|K_1\rangle$ and $|K_2\rangle$ CP eigenstates:

$$|K_{S,L}\rangle = \frac{|K_{1,2}\rangle + \tilde{\varepsilon}|K_{2,1}\rangle}{\sqrt{2(1 + |\tilde{\varepsilon}|^2)}} \quad (1.6)$$

with the parameter $\tilde{\varepsilon}$ defined as:

$$\frac{1 + \tilde{\varepsilon}}{1 - \tilde{\varepsilon}} = \sqrt{\left(\frac{M_{12} - i\Gamma_{12}/2}{M_{12}^* - i\Gamma_{12}^*/2}\right)} \quad (1.7)$$

This is the so-called ‘‘indirect CP violation’’, which has to be ascribed to $K_L \leftrightarrow K_S$ oscillations with strangeness S undergoing into $\Delta S = 2$ transitions. A second possible CP-violating effect can be produced by $\Delta S = 1$ weak transitions (‘‘direct CP violation’’) from the odd CP eigenstate $|K_2\rangle$ to a 2-pion final state. Direct CP violation in $\pi\pi$ final states can be parametrized by decomposing K^0 and \bar{K}^0 amplitudes in isospin I components:

$$A_I e^{i\delta_I} \equiv \langle I | CP^{-1} H_{weak} CP | K^0 \rangle \quad (1.8)$$

where δ_I is the phase shift between the $|\pi\pi\rangle$ physical state and the isospin eigenstate $|I\rangle$. CP symmetry allows to obtain

$$A_I e^{i\delta_I} = \langle I | CP^{-1} H_{weak} CP | \bar{K}^0 \rangle = A_I^* e^{i\delta_I} \quad (1.9)$$

so that A_0 can be set to a real value and only the difference between the weak phases, $\delta_2 - \delta_0$, becomes relevant for CP violation. By introducing the K_S and K_L decay widths

$$\eta_{+-} = \frac{\langle \pi^+ \pi^- | H_{weak} | K_L \rangle}{\langle \pi^+ \pi^- | H_{weak} | K_S \rangle}, \quad \eta_{00} = \frac{\langle \pi^0 \pi^0 | H_{weak} | K_L \rangle}{\langle \pi^+ \pi^- | H_{weak} | K_S \rangle} \quad (1.10)$$

and using the experimental observation ($\Delta I = 1/2$ rule) that the final state $|I = 0\rangle$ is favoured with respect to $|I = 2\rangle$, η_{+-} and η_{00} can be expressed as

$$\eta_{+-} \simeq \varepsilon + \varepsilon', \quad \eta_{00} \simeq \varepsilon - 2\varepsilon' \quad (1.11)$$

where

$$\varepsilon \simeq \tilde{\varepsilon}\varepsilon' \equiv e^{i(\delta_2 - \delta_0 + \pi/2)} \Im m A_2 / (A_0 \sqrt{2}) \quad (1.12)$$

The double ratio, defined as

$$R \equiv \left| \frac{\eta_{+-}}{\eta_{00}} \right|^2 = \frac{\Gamma(K_L \rightarrow \pi^0 \pi^0) / \Gamma(K_L \rightarrow \pi^+ \pi^-)}{\Gamma(K_S \rightarrow \pi^0 \pi^0) / \Gamma(K_S \rightarrow \pi^+ \pi^-)} \quad (1.13)$$

represents a powerful experimental method to extract information on the direct CP violation parameter ε' by means of the relation:

$$R \simeq 1 + 6\Re\left(\frac{\varepsilon'}{\varepsilon}\right) \quad (1.14)$$

$Im(\varepsilon'/\varepsilon)$ is expected to be small since the phases of ε and ε' are almost the same[65], therefore implying $\Re(\varepsilon'/\varepsilon) \simeq \varepsilon'/\varepsilon$. The statistical accuracy in the measurement of R is mainly driven by the $K_L \rightarrow \pi\pi$ decay statistics (about 3 orders of magnitude less than $K_L \rightarrow 3\pi$ decays):

$$\frac{\Delta R}{R} \simeq \sqrt{\frac{3}{2} \frac{1}{N(K_L \rightarrow \pi^0 \pi^0)}} \quad (1.15)$$

where the factor $N(K_L \rightarrow \pi^+ \pi^-) / N(K_L \rightarrow \pi^0 \pi^0) \sim 2$ has been taken into account. All measurements of $\Re(\varepsilon'/\varepsilon)$ have been performed at fixed target experiment (E731[5], NA31[6], KTeV[7], NA48[8]), unambiguously showing the presence of direct CP violation.

DAΦNE allows to produce $\phi \rightarrow K^0 \bar{K}^0$ decays, corresponding to coherent superpositions of $K_L K_S$ states; since the kaons are produced with a well defined momentum (~ 110 MeV) in the ϕ -meson rest frame, the detection of a K_S (K_L) tags the presence of a K_L (K_S) emitted in the opposite direction, so that very clear neutral kaon beams are produced. Given the $K_S K_L$ rates at DAΦNE and the KLOE detector performances, an accuracy of 10^{-4} on ε'/ε requires to collect 4.4×10^4 pb $^{-1}$.

1.2 The DAΦNE accelerator

The *Double Anular ϕ -factory for Nice Experiments* [9], DAΦNE is an electron-positron collider at the energy of the ϕ meson resonance ($M_\phi = 1019.460 \pm 0.019$

MeV [65]). The peak cross section is $\sigma(e^+e^- \rightarrow \phi) \simeq 3.1\mu\text{b}$.

Beside KLOE, two other experiments have been designed to run at DAΦNE : DEAR and FINUDA to study atomic and nuclear physics. A layout of the DAΦNE accelerator complex is sketched in fig. 1.1.

The injection system of the DAΦNE complex is provided by a 60m long linear accelerator (LINAC), that can accelerate e^+ and e^- up to 550 MeV. Then, particles are sent to a 33 m long accumulator ring, where they are relaxed to the injection conditions required by the collider. Two separate rings are used to store electron and positron beams, which in the project should have been constituted by up to 120 bunches each.

In the rings, shifted in the horizontal plane (see fig.1.1), the two beams circulate simultaneously and collide at the two interaction points (IP's) with a horizontal half crossing angle of ± 12.5 mrad, which results in a small momentum component ($\sim 13\text{MeV}$ in the horizontal plane) of the ϕ mesons produced. The dimensions of the bunches at the IP are typically:

$$\sigma_x \times \sigma_y \times \sigma_z = 2\text{mm} \times 20\mu\text{m} \times 30\text{mm} \quad (1.16)$$

The number of particles ($\sim 8.9 \times 10^{10}$) stored in a bunch is limited by the beam-beam interaction, which introduces a strong non-linearity in the beam dynamics, leading to beam blow-up and loss. The minimum bunch crossing period is $T_{bunch} = 2.7$ ns, corresponding to a crossing frequency of about 370 MHz.

1.2.1 DAΦNE achievements

The operation of DAΦNE with the KLOE experimental detector was successfully concluded in March 2006. Since April 1999 it delivered an integrated luminosity greater than 2.5 fb^{-1} on the peak of the ϕ resonance and of about 0.25 fb^{-1} off-peak (1000 MeV) mostly to reduce the systematic error on the hadronic cross section near threshold for 2-pion production [10], . Further a scan of the ϕ resonance (1010, 1018, 1023 and 1030 MeV) with high statistic has been performed for precise measurement of the ϕ line-shape.

As shown in fig.1.2 the machine performances have been continuously improving. The best peak luminosity obtained during the last KLOE run 2004 ÷ 2006 was $1.5 \cdot 10^{32}$

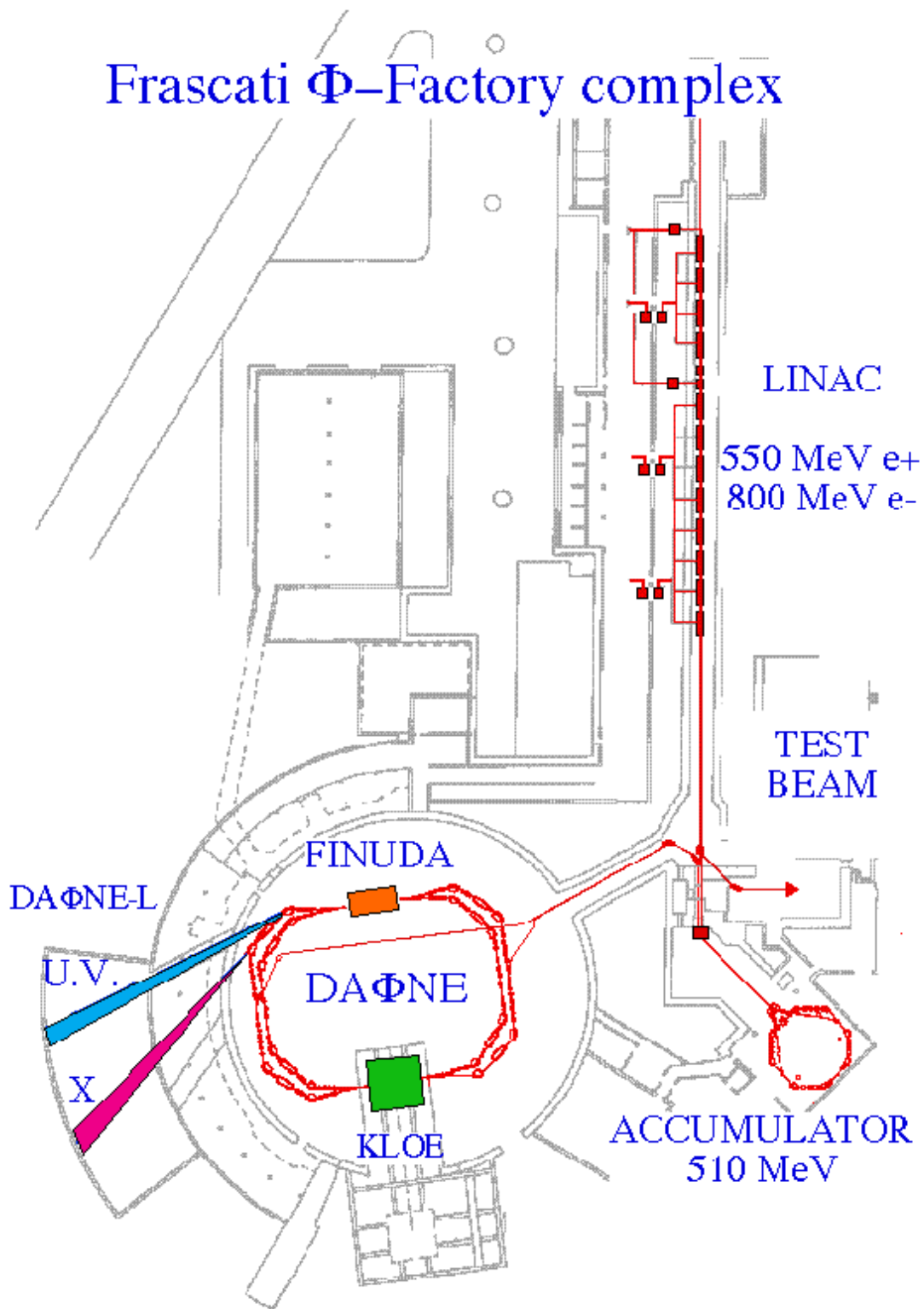


Figure 1.1: A sketch of the DAΦNE complex at the Laboratori Nazionali di Frascati of I.N.F.N.

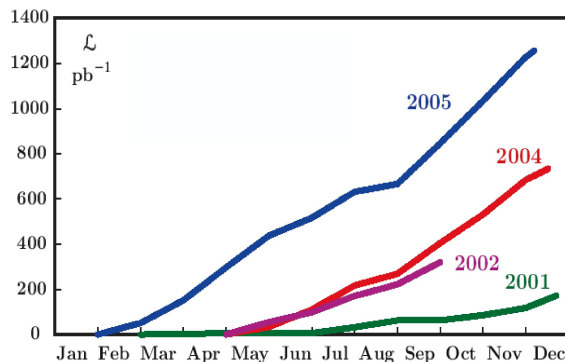


Figure 1.2: Integrated luminosity in pb^{-1} as function of the number of days of data taking for the years 2001 ÷ 2005.

$\text{cm}^{-2}\text{s}^{-1}$, with typical currents in collision of ~ 1.4 A for positrons and ~ 1.7 A for electrons, in 109 bunches.

Actually the KLOE detector has been moved out from the interaction region and its low-beta section substituted with a standard magnetic structure allowing for an easy vertical separation of the beams.

1.3 The KLOE experiment

The layout of the KLOE (K LOng Experiment) experiment has been driven by the measurement of $\Re(\varepsilon'/\varepsilon)$ with an accuracy of 10^{-4} .

The dimensions of the apparatus have been imposed by the K_L decay length: as in a ϕ -factory neutral kaons are produced with $\beta \simeq 0.216$, and considering their lifetimes[65], the decay length $\lambda = \beta\gamma c\tau$ of the K_L and K_S mesons are found to be $\lambda(K_L) \simeq 3.43$ m and $\lambda(K_S) \simeq 5.6$ mm.

For this reason KLOE has to provide a large and uniform geometrical acceptance over the whole volume in order to detect the charged and the neutral products of the K_L . Due to the low momenta of the kaons, the momenta of all the decay products basically range between 20 and 300 MeV, then one fundamental goal of the KLOE detector is to efficiently reconstruct particles having low momentum and energy. The detector [1][2]

is composed of a large cylindrical drift chamber (DC) and a hermetic electromagnetic calorimeter (EMC). A solenoidal magnetic field of about 0.52 T is provided by a superconducting coil and an iron yoke surrounding the whole apparatus, as shown in fig.1.3. The beam pipe is a sphere of 10 cm radius and 0.5 mm thickness around

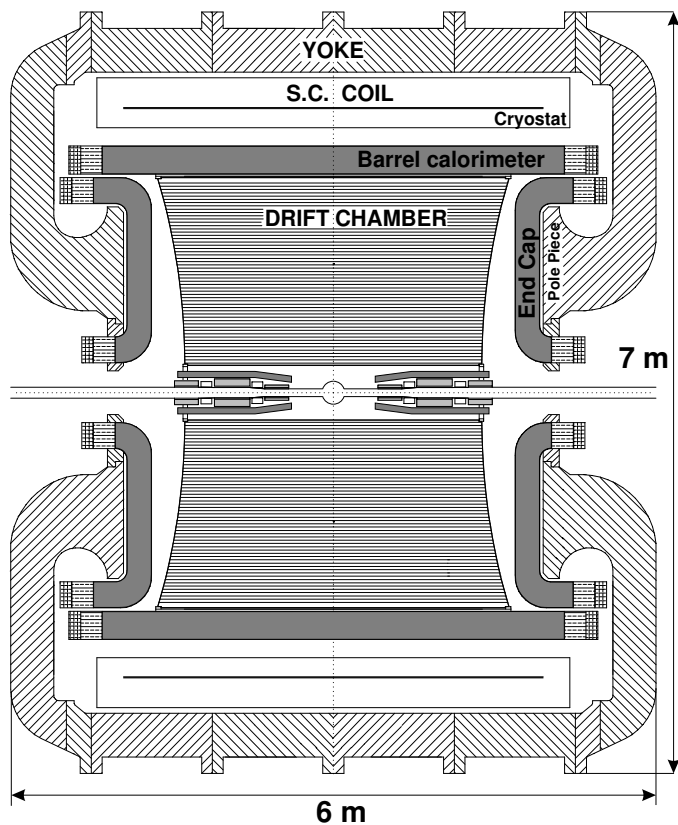


Figure 1.3: Section of the KLOE detector

the IP; it is made of an aluminum-beryllium alloy which minimizes the probability of both multiple scattering and K_S regeneration. Two low- β quadrupole triplets are inserted in the inner cylinder of the DC, on both sides of the interaction region; they are instrumented with compact lead-scintillating tile calorimeters, QCAL [13] that improve the geometrical acceptance for the low-energy photons.

1.3.1 The drift chamber

The KLOE DC [14] is a big cylindrical drift chamber with internal radius of 25 cm, external radius of 2 m and length of 3.3 m. These dimensions and all the choices for the chamber have been driven by requirement to have a large and uniform tracking volume to detect charged decay products and reconstruct vertices within 1 mm.

The chamber is filled with 12582 single sense wire almost square cells arranged in 58 circular and coaxial layers. Consecutive layers have stereo angles of opposite signs and absolute values varying with the radius, from 60 mrad to 150 mrad going outward, in order to minimize the distortion in the cell shape along the chamber radius. The ratio between the number of sense wires and field wires is 1:3 for a total of 52140 wires (including the two guard layers).

This solution ensures the highest homogeneity in filling the sensitive volume, see fig.1.4, thus obtaining high and uniform track and vertex reconstruction efficiencies.

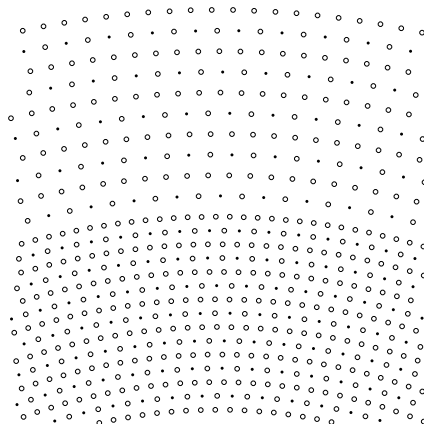


Figure 1.4: A detail of the configuration of the drift cell at $z = 0$, in a region between the small cells and the big ones. The empty circles represent the field wires, full dots are the sense wires.

The cell dimension is $2 \times 2 \text{ cm}^2$ in the innermost 12 layers and $3 \times 3 \text{ cm}^2$ in the outermost 46. A picture of the completely strung DC is shown in fig.1.5.

The gas mixture used to fill the detector is 90% He and 10% $i\text{C}_4\text{H}_{10}$, with a total gas radiation length of $\sim 1300 \text{ m}$, which becomes $\sim 900 \text{ m}$ considering the contribution of the wires ($25 \mu\text{m}$ diameter for the tungsten sense wires and $80 \mu\text{m}$ for the aluminum

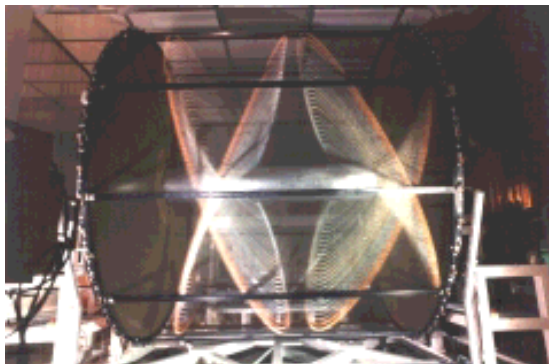


Figure 1.5: Photograph of the KLOE drift chamber after assembly and stringing.

field wires), in order to minimize multiple scattering, photon conversion before the calorimeter and K_S regeneration. Also the choice of carbon-fiber/epoxy for the mechanical structures of the DC was designed to improve transparency to low-energy photons and to reduce to minimum K_S regeneration in the inner tube.

The average spatial resolution within the chamber is $150 \mu\text{m}$ in the (r, ϕ) plane and 2 mm in the z coordinate.

The measured momentum resolution, obtained using Bhabha events (i.e. for 510 MeV electrons and positrons), is lower than 1.5 MeV in the range of polar angle between 50° and 130° , see fig.1.6.

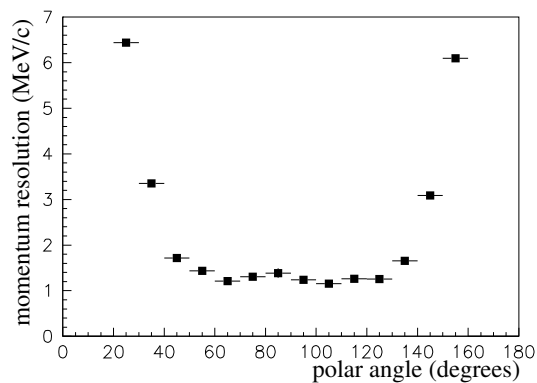


Figure 1.6: Momentum resolution as function of polar angle .

The momentum resolution for large-angle tracks is

$$\frac{\sigma_{p_T}}{p_T} \leq 0.4\%. \quad (1.17)$$

Cosmic ray tracks (i.e. track candidates in the DC with ≥ 96 hit cells) are used to study the cell efficiency, see fig.1.7. The “software” efficiency is obtained by requiring

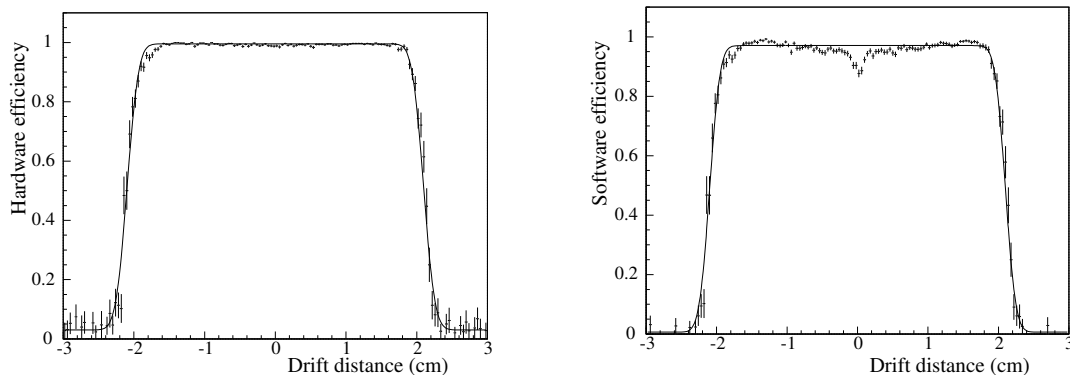


Figure 1.7: Software (left) and hardware (right) efficiencies as functions of the drift distance.

that the hit found in the cell is used in the track fit, and is measured as 97%, with a slight decrease for small drift distances due to worse resolution near the wire and to faults of the pattern recognition algorithm in resolving the left-right ambiguity. The “hardware” efficiency is considered as the ratio between the number of hits found in a cell and the number of tracks passing through it: for both small and big cells, this efficiency has been measured to be higher than 99% and to be constant over the whole volume of the chamber.

1.3.2 The electromagnetic calorimeter

The KLOE EMC [15] is a high-granularity lead/scintillating-fiber calorimeter. It consists of a barrel and two endcaps (fig. 1.8).

The barrel has a cylindrical shape with radius of 2 m and length of 4.4 m; it is composed of 24 trapezoidal-shaped modules, ~ 23 cm thick, in which the fibers run

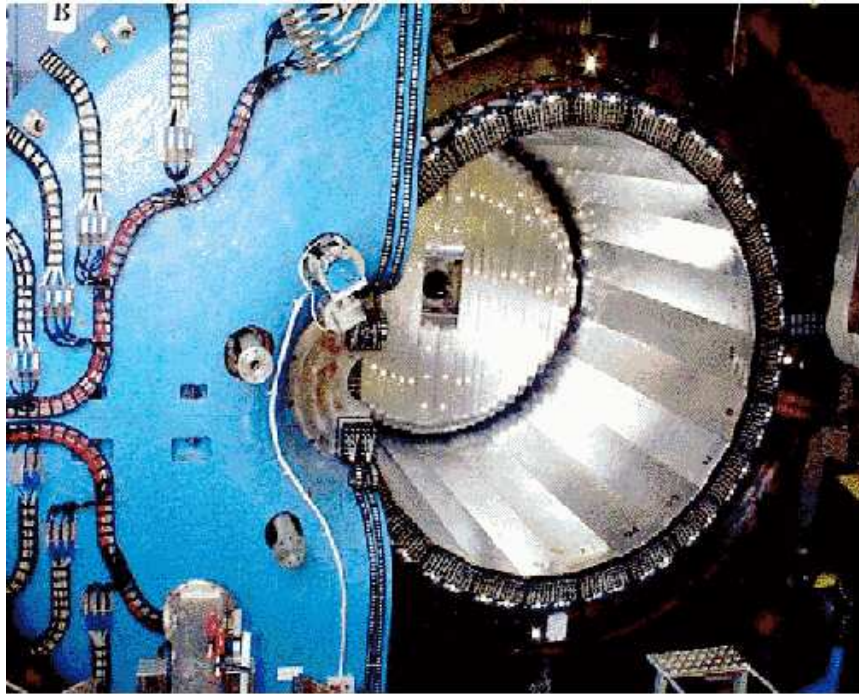


Figure 1.8: A picture of the KLOE electromagnetic calorimeter before inserting the drift chamber.

along the z direction. The endcaps are 32 C-shaped modules in which the fibers are disposed perpendicularly to the z axis; a 98% coverage of the full solid angle is achieved. Each module is obtained by alternating 0.5 mm thick lead foils to layers of 1 mm diameter scintillating fibers (see fig.1.9); in each module 200 layers are glued together. The resulting volume ratio for fibers:lead:glue is given by 48:42:10, while the average density of 5 g cm^{-3} provides a radiation length $X_0 \simeq 1.5 \text{ cm}$, in such a way that the total depth of the calorimeter corresponds to $\simeq 15 X_0$. At both sides of the calorimeter the modules are read via light guides coupled with photomultipliers, contained in aluminum tubes. The total number of channels used for the readout is 4880. In the barrel the channels are disposed in 5 planes (so determining a column along the azimuthal direction) of 12 cells for each module, while in the two endcaps the columns (from 2 to 6 depending on the module position) are arranged horizontally.

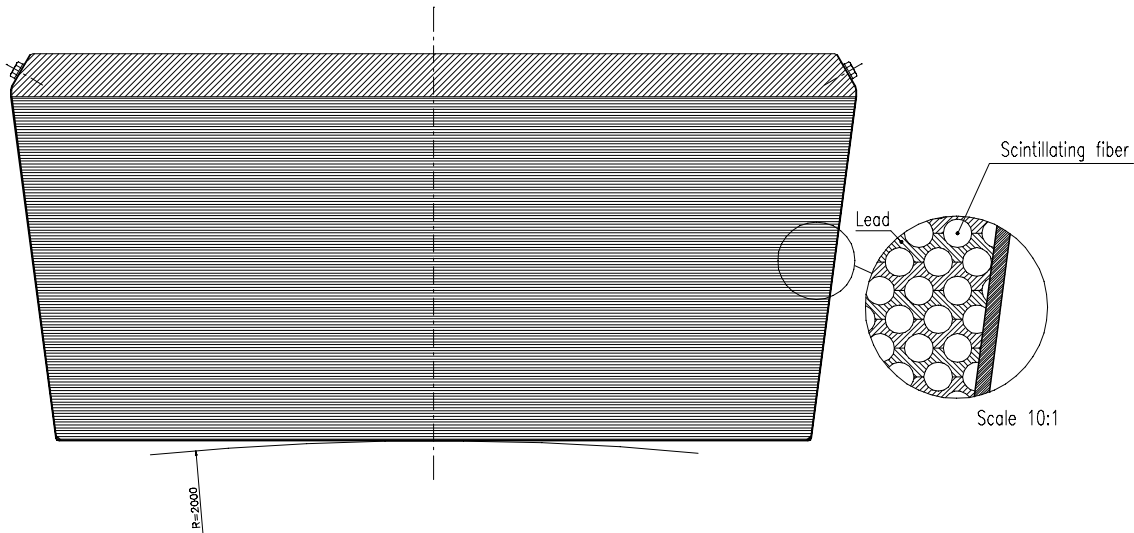


Figure 1.9: Schematic view of the fiber-lead modules in the KLOE electromagnetic calorimeter.

The readout granularity is $\sim 4.4 \times 4.4 \text{ cm}^2$, corresponding to a spatial resolution of $\sim 1.3 \text{ cm}$ on the transverse position of the cluster apex. The time difference measured at the two module ends by TDC's is used to compute the coordinate along the fiber. The energy deposit in each cell is derived by measuring the charge signal at each side by means of ADC's. Then, the z coordinate is constructed from the difference between the signal arrival times, and its resolution depends on the number of collected photoelectrons:

$$\sigma_z \simeq \frac{9 \text{ mm}}{\sqrt{E(\text{GeV})}}. \quad (1.18)$$

The linearity of the energy response and the energy resolution are extracted from radiative Bhabha events and from $\phi \rightarrow \pi^+ \pi^- \pi^0$ events: the track momenta reconstructed by the DC are used to estimate the photon energy, E_γ , which is compared with the energy E_{clu} measured by the calorimeter.

In fig.1.10 (top) the quantity $(E_{clu} - E_\gamma)/E_\gamma$ is plotted as a function of E_γ . The plot, obtained from radiative Bhabha events, shows that the linearity of energy is better than 1% over 70 MeV and that at lower energies deviations up to the 5% level are

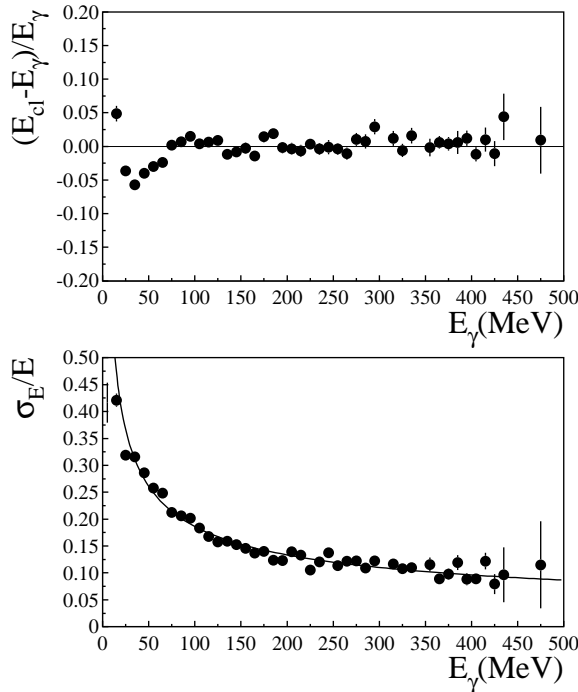


Figure 1.10: Up: plot of $(E_{clu} - E_\gamma)/E_\gamma$ for radiative Bhabha events. Down: energy resolution $\sigma(E)/E$. The solid line is the fit to the usual $a/\sqrt{E(\text{GeV})}+b$ parametrization.

evident, to be probably ascribed to the loss of shower fragments in the cluster reconstruction. In the lower plot of fig. 1.10 the energy resolution $\sigma(E)/E$ is obtained for each 10 MeV energy interval by fitting the distribution of $E_{clu} - E_\gamma$ with a Gaussian and extracting $\sigma(E)$ as its standard deviation. A fit with the function $a/\sqrt{E(\text{GeV})}+b$ produces a negligible constant b , while the stochastic term $a = 5.7\%$ proves that the energy resolution is mainly dominated by sampling fluctuations. The time resolution as a function of E_γ is studied through the analysis of some radiative ϕ decays fig.1.11. The agreement between the various channels is found to be satisfactory down to 100 MeV. In the intrinsic time resolution of the calorimeter[15]

$$\sigma_t = \frac{54 \text{ ps}}{\sqrt{E(\text{GeV})}} \oplus 100 \text{ ps} \quad (1.19)$$

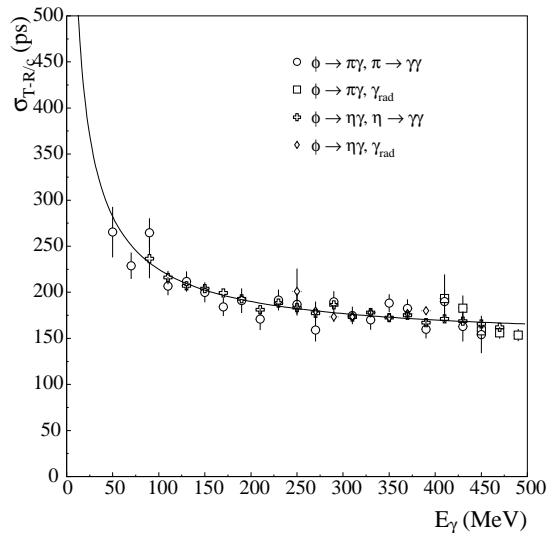


Figure 1.11: Time resolution versus the photon energy E_γ for radiative ϕ decays.

the first contribution is due to the sampling fluctuations (in agreement with test beam data [24]) and the second constant term is to be added in quadrature. Beside the various calorimeter miscalibrations (which amount to ~ 50 ps), the finite length in the beam direction of the luminous point produce a spread in the collision time and determines a further effect ~ 125 ps, to be added in eq. 1.19.

The photon detection efficiency ε_γ has been studied on different typologies of events in which energy and direction of γ 's can be easily extracted by means of DC tracking information and by suitably closing kinematics. Clusters are searched for in the EMC within a 3σ cone with axis on the expected flight direction of the photon. The results of ε_γ are illustrated in fig. 1.12 for three different categories of events: $e^+e^- \rightarrow e^+e^-\gamma$, $\phi \rightarrow \pi^+\pi^-\pi^0$ and $K_L \rightarrow \pi^+\pi^-\pi^0$. A reasonable agreement among these three samples over all the energy range can be observed. In particular, for the first two analyses, based on samples of photons emitted from the IP, the detection efficiency is more than 97% and nearly constant for $E_\gamma > 70$ MeV, while a loss is evident at lower values of E_γ .

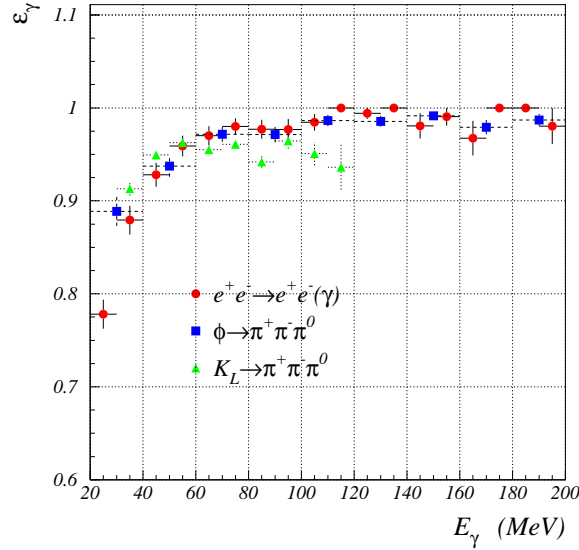


Figure 1.12: Photon detection efficiency versus the photon energy E_γ , for radiative Bhabha, $\phi \rightarrow \pi^+\pi^-\pi^0$ and $K_L \rightarrow \pi^+\pi^-\pi^0$ events.

1.4 The trigger

The events of physical interest for KLOE, i.e. ϕ decays, are only a small fraction of the events occurring at the DAFNE accelerator. The largest contributions to KLOE background, few MHz, are given by Coulomb scattering and gas bremsstrahlung in the vacuum chamber gas, and by Touschek particles in the beam.

Besides, Bhabha scattering occurs with a ~ 35 kHz event rate at the project luminosity of $5 \times 10^{32} \text{cm}^2 \text{s}^{-1}$ in the polar angle range $20^\circ < \theta < 160^\circ$. Also cosmic rays penetrating through the detector represent a relevant background for KLOE, ~ 3 kHz.

The main goal of the KLOE trigger system [16] is to retain all ϕ decays, to reject Bhabha and cosmic ray events (to be used in downscaled samples for calibration), and to reduce machine background to minimum.

In addition, it has to work in continuous mode, due to the small bunch crossing period of DAFNE, and to produce a valid signal for starting the data acquisition system

(DAQ). The KLOE trigger uses information based on the topology of the clusters in the EMC (energies and positions) and on the hits in the DC (number and spatial distribution) and is composed by two levels.

The level T1 (fast trigger) provides an immediate signal, within ~ 200 ns after the event; it is synchronized with the DAFNE radiofrequency and acts as a common START for ADC's and TDC's connected to the EMC.

The level T2 is generated during a longer lapse of time after T1 signal ($\sim 1.5 \mu\text{s}$) and is distributed to the DC TDC's; it acts as a common STOP and a START signal for the DAQ. About $\sim 2.6 \mu\text{s}$ are typically required to form the trigger and the detectors signals; during this time interval the generation of new T1 signal is inhibited. Apart from the two levels of trigger signals, the EMC provides separate signals with different thresholds for detecting Bhabha's and cosmic-rays.

1.4.1 The EMC trigger

For the EMC trigger adjacent columns of cells are grouped together into about 200 trigger sectors. The sectors are arranged in two series: "normal" and "overlap", being the columns of each series staggered by half a sector width. The signals coming from the photomultipliers corresponding to a sector are summed at each side, shaped and finally discriminated according to two distinct energy thresholds: ~ 30 MeV and ~ 20 MeV. The use of this logic scheme, shown in fig. 1.13, is optimized to reduce the effects of non-uniformity in response versus the coordinate along the direction of the fibers, due to the light attenuation in the fibers. The two thresholds can be programmed and different profiles can be applied. The high rate of accidental clusters (particularly in the endcaps) due to machine background, imposes the use of higher thresholds in the regions closer to the beam (hot and warm trigger regions), while the profiles for the ones at larger radius are similar to those of the barrel (cold trigger region).

The typical threshold values applied for ϕ events range from 50 MeV in the cold region, up to 150 MeV for warm and hot regions in the endcaps. The sufficient condition for an EMC trigger is verified if two or more trigger sectors happen to be fired (in a ~ 70 ns time window) and if at least one of them is in the barrel. The EMC trigger operates in the first level mode (T1 \equiv T2).

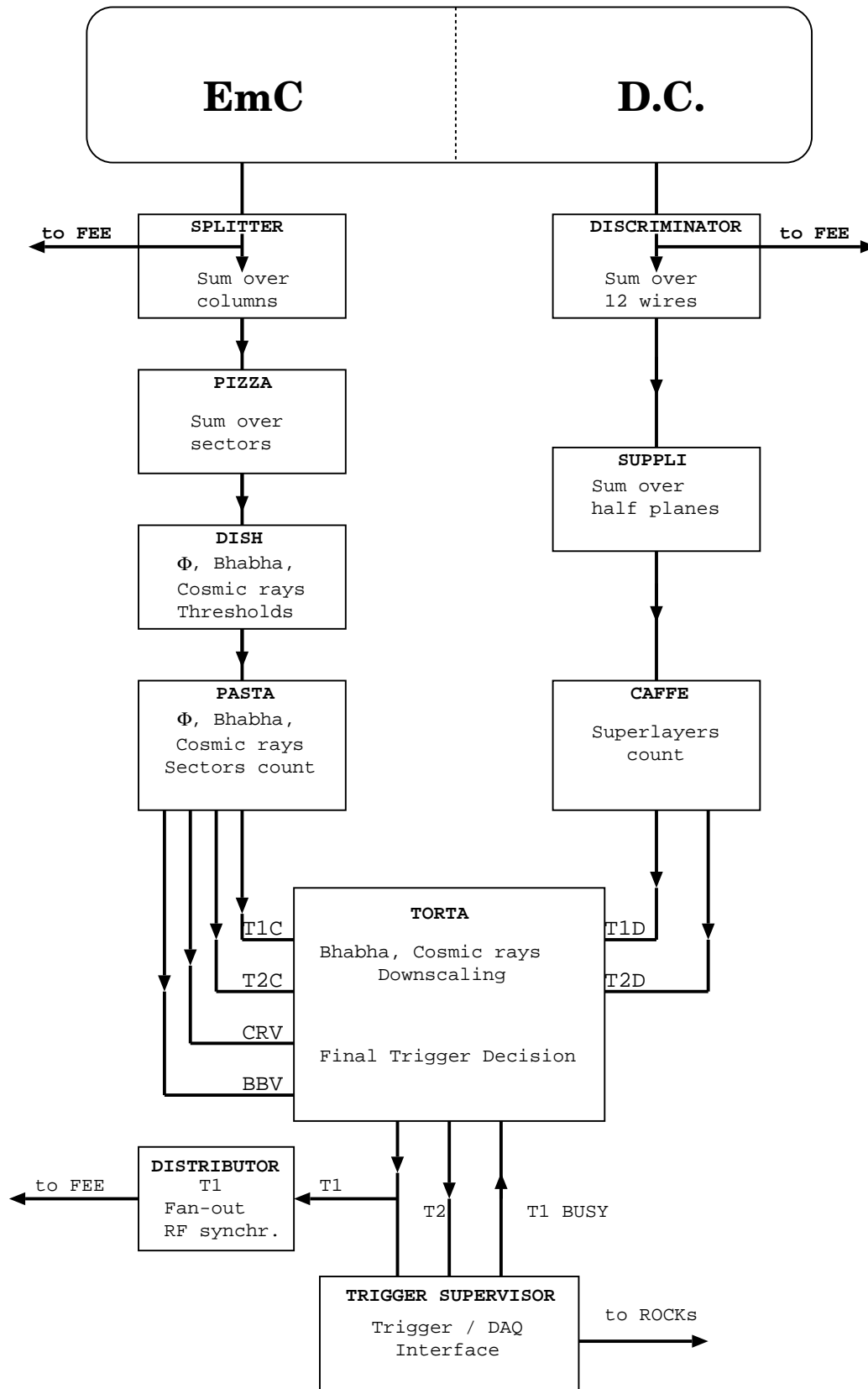


Figure 1.13: Logic scheme of a trigger sector.

1.4.2 The DC trigger

In order to define the DC trigger, hits in the chamber are grouped into 9 concentric superlayers, obtained from contiguous plane signals. The sum of the signals is clipped to a given threshold (therefore limiting the occurrence of spiraling low-momentum particles induced by DAΦNE), and finally a total number of at least 15 hits in a 250 ns window is required for the production of a T1 signal.

If the number of hits exceeds 125 in an interval of 850 ns following the previous time window, then the DC condition for the T2 signal is satisfied. Time intervals of $\sim 1 \mu\text{s}$ are typically needed for the DC signals to be formed. Finally, the trigger requires for the first level the OR between the EMC trigger and the DC T1 condition; in case T1 is given by the EMC trigger, the T2 signal is automatically generated $\sim 1.5 \mu\text{s}$ later, while if the DC T1 condition is verified the T2 signal is then obtained by the logical OR between the EMC trigger and the DC T2 condition.

1.5 The data acquisition

The main goal of the KLOE Data Acquisition (DAQ) system [17] was to collect data at a maximum rate of 50 Mb/s from the ~ 13000 channels of the DC, the ~ 5000 ADC's and TDC's channels of the EMC and of the trigger system¹. The DAQ system is required to be exible and the integrity of the events during the acquisition has to be continuously checked online, with a dead time which is constant and is independent of event topologies.

The KLOE DAQ is based on two levels of high-speed data concentration for bu ering data coming from the Front-End Electronics (FEE) connected to the detector and an online farm of CPU's for recording events, as shown in fig. 1.14.

The first level (L1) of DAQ is arranged in 10 chains (4 are dedicated to the acquisition of the EMC, 4 of the DC and 2 of the trigger). These chains are composed of up to six VME crates, each one with 16 slave boards and a Read Out Controller (ROCK) collecting information from the FEE via the AUX-bus, a custom protocol developed specifically for the KLOE DAQ. All the ROCK's in a chain are connected

¹Given an average event size of 5 kb, this through put corresponds to 10 kHz, constituted by ϕ decays, Bhabha and cosmic-ray events.

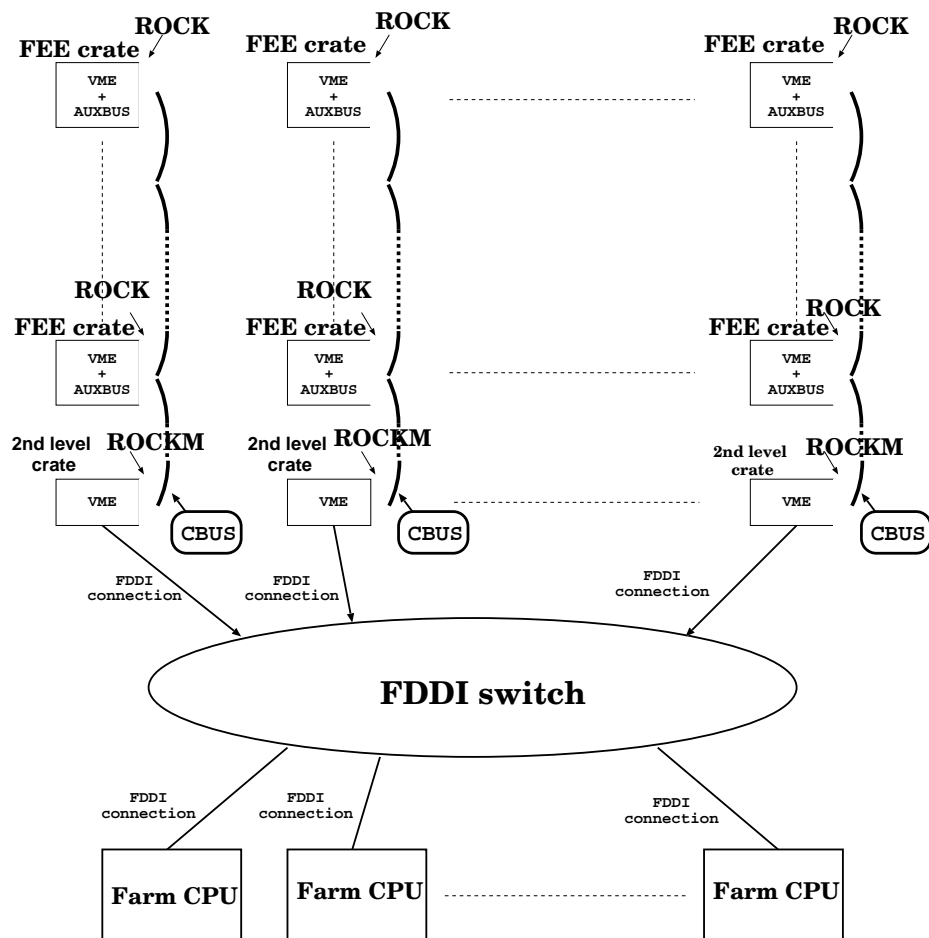


Figure 1.14: The architecture of the Data Acquisition System.

to a controller manager (ROCKM) through a custom fast bus (C-bus).

In the second level (L2), the ROCKM's build pieces of events produced by the FEE and tagged by a trigger number (sub-events), which are acquired in streams by VME processors, equipped with FDDI interfaces. Two software processes – the Collector and the Sender – running on the processors asynchronously, manage the read-out activity: the Collector accesses to ROCKM memory and pushes data frames belonging to different triggers in a FIFO-structured shared memory (circular buffer), while the Sender retrieves from the queue a given amount of sub-events and transmits it to the online farm via a fast FDDI connection.

A Data Flow Control process (DFC) provides the addresses of the online farm CPU's, guaranteeing that all sub-events with the same trigger number are sent to the same CPU online farm. The Receiver process is in charge of catching these sub-events and putting them in a circular buffer; subsequently the Builder process merges them together to build a whole event in a YBOS format [25].

Events are saved on tape and on disks by the Recorder process. Also another process –the Spy-Daemon– reads formatted events and writes them in a spy buffer to perform various monitoring and calibration tasks at a third level (L3) (e.g. Bhabha and $\gamma\gamma$ events are written on the L3bha buffer, cosmic-ray events are written on the L3cos buffer).

The uniformity and the stability of the acquired data and of the detector performances are controlled continuously by a number of dedicated processes. Among the procedures implemented, the Trgmon exploits the pattern of the acquired information from the trigger chains to fastly check luminosity, data/background rates and other relevant quantities; histogram-servers and event-display also use the shared memory mechanism to fetch data.

Some procedures are performed run by run, like the measurements of the beam energies and (the Trkmon process using Bhabha's) and the monitor of the general quantities of the experiment through dedicated histogram browsers, while other jobs are done periodically, like the drift chamber and the calorimeter energy/time calibrations.

Chapter 2

η physics at KLOE

At the ϕ -factory, visible cross section for ϕ production is about $3.3 \mu\text{b}$ and the η meson is produced in the 2-body decay $\phi \rightarrow \eta\gamma$ with a branching ratio of 1.3%.

The entire KLOE data set correspond to more than $10^8 \eta$ meson, thus a rather rich program of η decay studies is feasible with the KLOE detector. The η decays such as $\eta \rightarrow 3\pi$, the subject of this work, $\eta \rightarrow \pi^0 \gamma\gamma$, and $\eta \rightarrow \pi^+ \pi^- \gamma$ allow important tests of the Chiral Perturbation Theory: the precise measurement of these decays, which is presently going on at KLOE, will add significant knowledge in this sector.

Moreover the rare decay $\phi \rightarrow \eta'\gamma$ can be used to exploit the direct relation between the ratio $R = Br(\phi \rightarrow \eta'\gamma)/Br(\phi \rightarrow \eta\gamma)$ and the $\eta - \eta'$ mixing angle: the value of this angle is related to the presence of a valence gluon content in the η' meson.

In this chapter some analysis on light meson spectroscopy in the KLOE experiment are described. An overview of the Chiral Perturbation Theory is given with an emphasis on what can be learned for the $\eta \rightarrow \pi^+ \pi^- \pi^0$.

2.1 Measurement of the ratio

$$Br(\phi \rightarrow \eta'\gamma)/Br(\phi \rightarrow \eta\gamma)$$

The ratio of the branching ratios $R = Br(\phi \rightarrow \eta'\gamma)/Br(\phi \rightarrow \eta\gamma)$ is related to the $\eta - \eta'$ mixing angle. The value of this angle is related to the presence of a valence gluon content in the η' meson [36]. Here we describe a preliminary KLOE measurement of this ratio by using the final state $\pi^+ \pi^- \gamma$.

The final state $\pi^+ \pi^- 7\gamma$ can be given by two different decay chains:

$$\phi \rightarrow \eta' \gamma, \eta' \rightarrow \pi^+ \pi^- \eta, \eta \rightarrow 3\pi^0$$

$$\phi \rightarrow \eta' \gamma, \eta' \rightarrow \pi^0 \pi^0 \eta, \eta \rightarrow \pi^+ \pi^- \pi^0$$

The following requirements are used for the signal events:

- 1 charged vertex in a cylinder with a 4 cm radius and a 16 cm length around the interaction point;
- 7 clusters in the calorimeter with time $|t-r/c| < 5\sigma_t$ where (σ_t is the calorimeter time resolution) and angle $\theta_\gamma > 21^\circ$ respect to the beam direction. The angular cut is used to reject machine background that produces accidental clusters in the lower angular region of the calorimeter;
- all the events identified as a K_S, K_L pair are rejected.

A kinematic fit is performed imposing energy-momentum conservation and the χ^2 of the kinematic fit is used as a selection variable.

At the end of the selection procedure 3750 events are identified. The background has been estimated using a Monte Carlo simulation of the all physical processes that can be identified as signal together with the full simulation of the detector response. The main background channels are:

$$\begin{aligned} K_S \rightarrow \pi^+ \pi^-, K_L \rightarrow 3\pi^0 & \quad K_S \rightarrow \pi^0 \pi^0, K_L \rightarrow \pi^+ \pi^- \pi^0 \\ K_S \rightarrow \pi^+ \pi^- \gamma, K_L \rightarrow \pi^0 \pi^0 \pi^0 & \end{aligned} \quad (2.1)$$

The first 2 processes emulate the signal if an additional cluster is present, either from machine background or from cluster splitting in the calorimeter.

The total number of estimated background events is 345, that gives a number of signal events N_{signal} :

$$N_{signal} = N_{observed} - N_{expbkg} = 3405 \pm 65_{stat.} \pm 28_{syst.} \quad (2.2)$$

The systematic error comes from the variation of the background estimated as a function of the rate of accidental clusters in the detector.

The number of $\phi \rightarrow \eta\gamma$ decays is determined by counting the number of $\eta \rightarrow 3\pi^0$

decays ($N_{\eta \rightarrow 3\pi^0} = 1665000 \pm 1300$). The ratio of the two branching ratios is extracted using the following formula:

$$R = \frac{Br(\phi \rightarrow \eta' \gamma)}{Br(\phi \rightarrow \eta \gamma)} = \frac{N(\eta' \rightarrow \pi^+ \pi^- \gamma)}{N(\eta \rightarrow 3\pi^0)} \frac{\varepsilon_{\eta \rightarrow 3\pi^0} Br(\eta \rightarrow 3\pi^0)}{Br_{charged} \varepsilon_{charged} + Br_{neutral} \varepsilon_{neutral}} K_\rho \quad (2.3)$$

where:

$$\begin{aligned} Br_{charged} &= Br(\eta' \rightarrow \pi^+ \pi^- \eta) \cdot Br(\eta \rightarrow 3\pi^0) \\ Br_{neutral} &= Br(\eta' \rightarrow \pi^0 \pi^0 \eta) \cdot Br(\eta \rightarrow \pi^+ \pi^- \pi^0) \end{aligned} \quad (2.4)$$

The factor K_ρ is a correction factor to the observed decay rate due to the interference between $\phi \rightarrow \eta(\eta')\gamma$ and $\rho \rightarrow \eta(\eta')\gamma$. The main source of systematic error comes from the uncertainty on the $\eta' \rightarrow \pi^+ \pi^- \eta$ and $\eta' \rightarrow \pi^0 \pi^0 \eta$ branching ratios (3%). Using the expression for R we obtain the preliminary result:

$$R = (4.77 \pm 0.07_{stat} \pm 0.19_{sys}) \cdot 10^{-3}$$

Using the current PDG [65] value for $BR(\phi \rightarrow \eta \gamma)$ we extract the:

$$BR(\phi \rightarrow \eta' \gamma) = (6.20 \pm 0.11_{stat} \pm 0.25_{sys}) \cdot 10^{-5}$$

The value obtained for R can be related directly to the pseudoscalar mixing angle in the flavour basis. Using the approach by Bramon et al.[37], where the SU(3) breaking is taken into account via constituent quark mass ratio m_s/\bar{m} , and we take into account a correction induced by the OZI-rule, which reduce the VP wave-function overlaps [38], via the two parameters Z_{NS} and Z_S :

$$R = \frac{BR(\phi \rightarrow \eta' \gamma)}{BR(\phi \rightarrow \eta \gamma)} = \cot^2 \varphi_P \left(1 - \frac{m_s}{\bar{m}} \frac{Z_{NS}}{Z_S} \frac{\tan \varphi_V}{\sin 2\varphi_P} \right)^2 \left(\frac{p_{\eta'}}{p_\eta} \right)^3$$

where $\varphi_V = 3.4^\circ$ is the deviation from ideal mixing for vector mesons and $p_{\eta(\eta')}$ is the radiative photon momentum in the ϕ center of mass. We find the following results:

$$\varphi_P = (41.4 \pm 0.3_{stat} \pm 0.7_{sys} \pm 0.6_{th})^\circ$$

This φ_P value is equivalent to the mixing angle of $\theta_P = (-13.2 \pm 0.3_{stat} \pm 0.7_{sys} \pm 0.6_{th})^\circ$ in the octet-singlet basis. The mixing angle value has been obtained neglecting possible gluonium contents of the η' meson. A gluonium component of the η' can be parametrized as following

$$|\eta' \rangle = X_{\eta'} \frac{1}{\sqrt{(2)}} |u\bar{u} + d\bar{d}\rangle + Y_{\eta'} |s\bar{s}\rangle + Z_{\eta'} |gluonium\rangle$$

via the $Z_{\eta'}$ parameter. The normalization gives:

$$X_{\eta'}^2 + Y_{\eta'}^2 + Z_{\eta'}^2 = 1$$

A possible gluonium content of the η' is revealed by

$$Z_{\eta'}^2 > 0 \Leftrightarrow X_{\eta'}^2 + Y_{\eta'}^2 < 1$$

Constraints based on simple $SU(3)$ ideas can be used to check the assumption of no gluonium contents of the η' meson. If $Z_{\eta'} = 0$ one has $Y_{\eta'} = \cos \varphi_P$, which is a reasonable approximation if the gluonium component is small. In fig.2.1 we plot allow band corresponding to $SU(3)$ constraints and our measurement of $\cos \varphi_P$, in the $X_{\eta'}, Y_{\eta'}$ plane. The circumference $X_{\eta'}^2 + Y_{\eta'}^2 = 1$ correspond to zero gluonium in the η' .

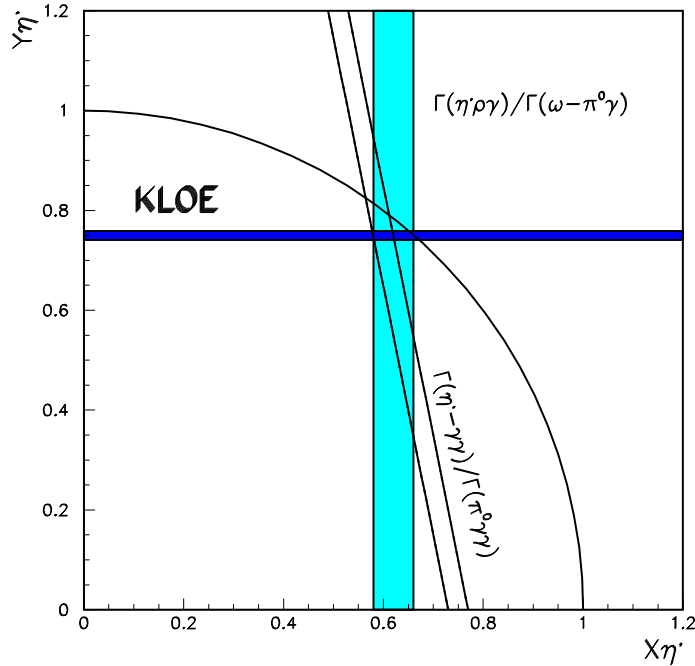


Figure 2.1: Bounds on X and Y from $SU(3)$ calculations and experimental branching fractions. The three constraints: $\frac{\Gamma(\eta' \rightarrow \gamma\gamma)}{\Gamma(\pi^0 \rightarrow \gamma\gamma)}$; $\frac{\Gamma(\eta' \rightarrow \rho\gamma)}{\Gamma(\omega \rightarrow \pi^0\gamma)}$; $\frac{\Gamma(\phi \rightarrow \eta'\gamma)}{\Gamma(\phi \rightarrow \eta\gamma)}$.

We find

$$X_{\eta'}^2 + Y_{\eta'}^2 = 0.92 \pm 0.06$$

2.2 Measurement of the branching fraction

$$\eta \rightarrow \pi^0 \gamma \gamma$$

The $\eta \rightarrow \pi^0 \gamma \gamma$ decay has been measured by several experiments in the past. The experimental value of this branching fraction decreased with time, in step with the increase in machine luminosities and in the available statistics of the η meson samples produced, showing that the main issue in the measurement of this branching fraction measurement is the correct estimate of the background. The 2006 Review of Particle Physics [65] list only the measurement from the GAMS experiment [41], $(7.2 \pm 1.4) \times 10^{-4}$. Two more measurements have been published by the Crystal Ball collaboration. These two measurements are different analyses of the same data sample; they find the values: $(3.5 \pm 0.7_{stat.} \pm 0.6_{syst.}) \times 10^{-4}$ [42] and $(2.7 \pm 0.9_{stat.} \pm 0.5_{syst.}) \times 10^{-4}$ [43]. At KLOE the $\eta \rightarrow \pi^0 \gamma \gamma$ proceeds through the decay chain:

$$\phi \rightarrow \gamma \eta, \eta \rightarrow \pi^0 \gamma \gamma, \pi^0 \rightarrow \gamma \gamma \quad (2.5)$$

Therefore there are 5 γ in the final state. The main background processes are:

$$\begin{aligned} \phi \rightarrow \gamma f_0, f_0 \rightarrow \pi^0 \pi^0, \pi^0 \rightarrow \gamma \gamma \quad \phi \rightarrow \gamma a_0, a_0 \rightarrow \eta \pi^0, \eta \rightarrow \gamma \gamma, \pi^0 \rightarrow \gamma \gamma \\ e^+ e^- \rightarrow \pi^0 \omega, \omega \rightarrow \pi^0 \gamma, \pi^0 \rightarrow \gamma \gamma \quad \phi \rightarrow \eta \gamma, \eta \rightarrow 3\pi^0, \pi^0 \rightarrow \gamma \gamma \end{aligned} \quad (2.6)$$

The background composition in the data sample is determined at an early stage of the analysis where the signal contribution is negligible, by fitting the spectrum of the invariant mass of all pairs of photons ($m_{\gamma\gamma}$) as shown in fig.2.2. Further analysis criteria are used to reject background coming from the $\eta \rightarrow 3\pi^0$ channel when one or more pairs of photons merge in the calorimeter. A likelihood function has been built to identify merged clusters. At the last stage of the analysis, the spectrum of the invariant mass $m_{4\gamma}$ is used to extract the number of signal events. The spectrum shown in fig.2.2 is fitted with the MC expected distributions of the background and of the signal. The number of signal events is $N_{sig} = 68 \pm 23$. To extract the branching fraction, we have counted the number of $\eta \rightarrow 3\pi^0$ events in the same data sample: $N_{\eta \rightarrow 3\pi^0} = 2288882$. The efficiency of the $\eta \rightarrow \pi^0 \gamma \gamma$ analysis has been computed by MC, using a flat phase space assumption for the $\pi^0 \gamma \gamma$ dynamics. The efficiencies are $\varepsilon_{\eta \rightarrow \pi^0 \gamma \gamma} = 4.63 \pm 0.09\%$, and $\varepsilon_{\eta \rightarrow 3\pi^0} = 0.378 \pm 0.08_{syst} \pm 0.01_{stat}$. Therefore we can write:

$$\frac{Br(\eta \rightarrow \pi^0 \gamma \gamma)}{Br(\eta \rightarrow 3\pi^0)} = \frac{N(\eta \rightarrow \pi^0 \gamma \gamma) \cdot \varepsilon_{\eta \rightarrow 3\pi^0}}{N(\eta \rightarrow 3\pi^0) \cdot \varepsilon_{\eta \rightarrow \pi^0 \gamma \gamma}} = (2.43 \pm 0.82) \times 10^{-4} \quad (2.7)$$

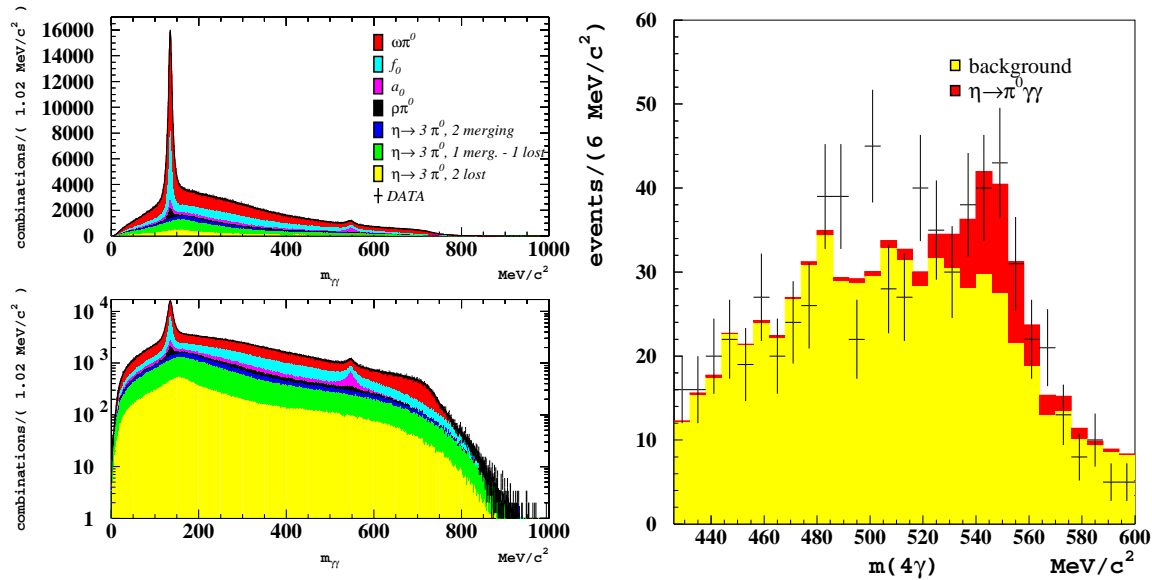


Figure 2.2: Left: $m_{\gamma\gamma}$ distribution used to determine the background content; Right: $m_{4\gamma}$ distribution: DATA, dots with error bars, MC signal and MC background are normalised according the fit result.

Using the value of $Br(\eta \rightarrow 3\pi^0)$ reported in [40] we obtain the preliminary KLOE result:

$$Br(\eta \rightarrow \pi^0 \gamma\gamma) = (8.4 \pm 2.7_{stat} \pm 1.4_{syst}) \times 10^{-5} \quad (2.8)$$

This value is lower than the previously published values and it is in agreement with ChPT prediction at order p^6 with VMD resonance saturation assumption for the \mathcal{L}_6 Lagrangian [44, 45].

2.3 η mass measurement

Recently a new η mass measurement has been performed by the GEM collaboration [46] that measures a mass value that is 0.5 MeV below the previous NA48 measurement [68], but it is in agreement with the previous η mass measurements [40]. For this reason KLOE is performing a new measurement of the η mass using a completely different approach. The mass is measured studying the decay $\phi \rightarrow \eta\gamma, \eta \rightarrow \gamma\gamma$. To improve the energy response of the calorimeter a kinematic fit is performed imposing

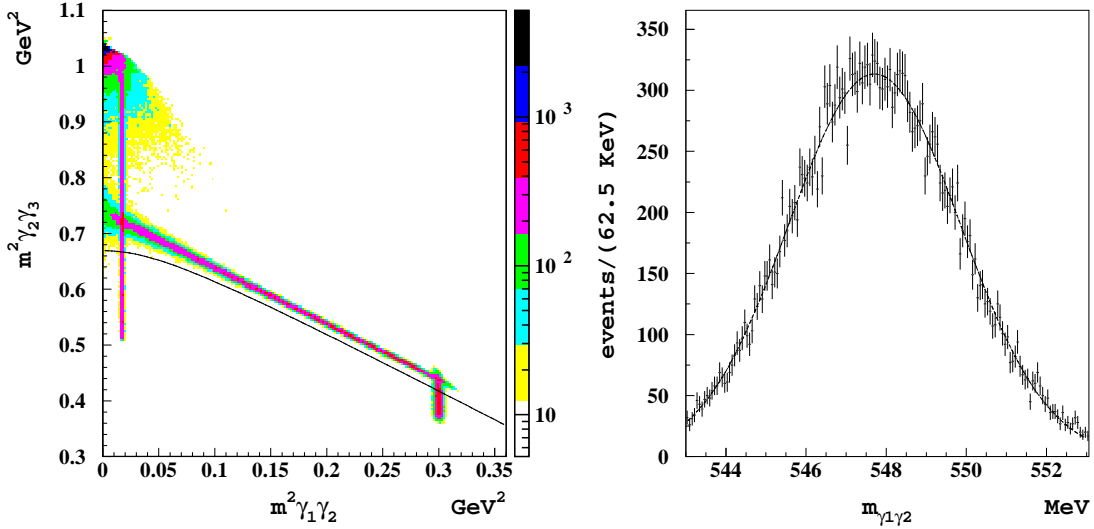


Figure 2.3: Left: Dalitz plot of the 3γ final state, the cut chosen to reject background is shown, Right: $m_{\gamma\gamma}$ distribution.

energy-momentum conservation. A cut in the Dalitz plot of the 3γ final state is performed in order to reduce the background mainly due to $e^+e^- \rightarrow \gamma\gamma$, $e^+e^- \rightarrow e^+e^-(\gamma)$, $\phi \rightarrow \pi^0 \gamma$, fig. 2.3. A sharp peak around the η mass is found with negligible background ($\sigma_{peak} \sim 2$ MeV), fig. 2.3. The 2001 - 2002 data taking has been divided into 8 periods, each corresponding to about 50 pb^{-1} of collected data. In fig. 2.4 the measurements obtained in the 8 periods are shown. The statistical error has been computed by fitting the 8 measurements with a constant. The fit give the value $M_\eta = 547765 \pm 5_{stat}$ keV. The systematic error has been studied by studying the effect of energy, time, vertex position and \sqrt{s} miscalibration on the measured value of the η mass. All the measurement lie in the estimated systematic band. The preliminary result obtained is:

$$m_\eta = 547822 \pm 5_{stat} \pm 69_{syst} \text{ keV} \quad (2.9)$$

As a check of the method we have measured also the mass of the π^0 by using the decay $\phi \rightarrow \pi^0 \gamma$ obtaining $m_{\pi^0} = 134990 \pm 6_{stat.} \pm 30_{syst.}$ keV, that is fully in agreement with the value reported in [40] $m_{\pi^0}^{PDG} = 134976.6 \pm 0.6$ keV.

The preliminary measurement differs from the NA48 measurement, ($m_\eta^{NA48} = 547843 \pm 30_{stat.} \pm 41_{syst.}$ keV) by only 0.24 standard deviations. It disagrees with the GEM

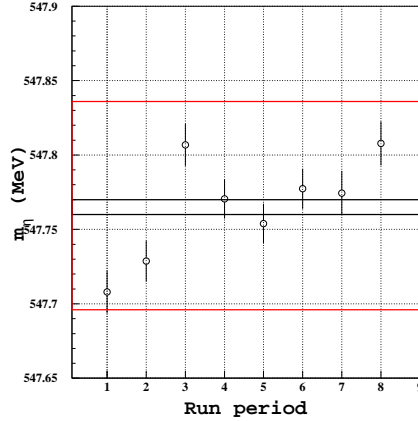


Figure 2.4: η mass measurement in the several periods. The systematic band, red rectangle, is shown.

measurement ($m_\eta^{GEM} = 547311 \pm 28_{stat.} \pm 32_{syst.}$ keV) by 7 standard deviations.

2.4 Basics of Chiral Perturbation Theory

Chiral perturbation theory (ChPT) provides a systematic framework for investigating strong-interaction processes at *low* energies, as opposed to a perturbative treatment of quantum chromodynamics (QCD) at high momentum transfers in terms of the “running coupling constant.” The basis of ChPT is the global $SU(3)_L \times SU(3)_R$ symmetry of the QCD Lagrangian in the limit of massless u , d , and s quarks. This symmetry is assumed to be spontaneously broken down to $SU(3)_V$ giving rise to eight massless Goldstone bosons. In the following the foundations of ChPT, namely the symmetries of QCD and their consequences in terms of effective theory is given.

2.4.1 Chiral symmetry

The QCD Lagrangian obtained from the gauge principle is:

$$L_{QCD} = -\frac{1}{2}\text{tr}G_{\mu\nu}G^{\mu\nu} + \sum_{f=u,d,s} \bar{q}_f (i\gamma_\mu D^\mu - m_f) q_f \quad (2.10)$$

where:

$$G_{\mu\nu} = \partial_\mu A_\nu - \partial_\nu A_\mu - ig[A_\mu, A_\nu] \quad (2.11)$$

$$D_\mu = (\partial_\mu - igA_\mu) \quad (2.12)$$

and the color field is given by¹

$$A_\mu = \sum_{a=1}^8 A_\mu^a \frac{\lambda^a}{2} \quad (2.13)$$

In order to fully exhibit the global symmetries of lagrangian, we consider the chirality matrix $\gamma_5 = \gamma^5 = i\gamma^0\gamma^1\gamma^2\gamma^3$, $\{\gamma^\mu, \gamma_5\} = 0$, $\gamma_5^2 = 1$,² and introduce projection operators

$$P_R = \frac{1}{2}(1 + \gamma_5) = P_R^\dagger, \quad P_L = \frac{1}{2}(1 - \gamma_5) = P_L^\dagger, \quad (2.14)$$

where the indices R and L refer to right-handed and left-handed, respectively, as will become more clear below. Obviously, the 4×4 matrices P_R and P_L satisfy a completeness relation,

$$P_R + P_L = 1, \quad (2.15)$$

are idempotent, i.e.,

$$P_R^2 = P_R, \quad P_L^2 = P_L, \quad (2.16)$$

and respect the orthogonality relations

$$P_R P_L = P_L P_R = 0. \quad (2.17)$$

The combined properties of Eqs. (2.15) – (2.17) guarantee that P_R and P_L are indeed projection operators which project from the Dirac field variable q to its chiral components q_R and q_L ,

$$q_R = P_R q, \quad q_L = P_L q. \quad (2.18)$$

We recall in this context that a chiral (field) variable is one which under parity is transformed into neither the original variable nor its negative.³ Under parity, the

¹ λ^a (with $a = 1, \dots, 8$) are the $SU(3)$ Gell-Mann matrices, operating in color space.

²Unless stated otherwise, we use the convention of Ref. [19].

³In case of fields, a transformation of the argument $\vec{x} \rightarrow -\vec{x}$ is implied.

quark field is transformed into its parity conjugate,

$$P : q(\vec{x}, t) \mapsto \gamma_0 q(-\vec{x}, t),$$

and hence

$$q_R(\vec{x}, t) = P_R q(\vec{x}, t) \mapsto P_R \gamma_0 q(-\vec{x}, t) = \gamma_0 P_L q(-\vec{x}, t) \neq \pm q_R(-\vec{x}, t),$$

and similarly for q_L .⁴ The QCD Lagrangian in the chiral limit, where $m_s = m_u = m_d = 0$, can be written as:

$$L_{QCD}^0 = -\frac{1}{2} \text{tr} G_{\mu\nu} G^{\mu\nu} + \sum_{l=u,d,s} (\bar{q}_{R,l} i \gamma_\mu D^\mu q_{R,l} + \bar{q}_{L,l} i \gamma_\mu D^\mu q_{L,l}) \quad (2.19)$$

Due to the flavor independence of the covariant derivative L_{QCD}^0 is invariant under

$$\begin{pmatrix} u_L \\ d_L \\ s_L \end{pmatrix} \rangle U_L \begin{pmatrix} u_L \\ d_L \\ s_L \end{pmatrix} \quad \begin{pmatrix} u_R \\ d_R \\ s_R \end{pmatrix} \rangle U_R \begin{pmatrix} u_R \\ d_R \\ s_R \end{pmatrix} \quad (2.20)$$

where $U_{R,L}$ are the unitary 3×3 matrices:

$$U_{R,L} = \exp \left(-i \sum_{a=1}^8 \theta_a^{R,L} \frac{\lambda_a}{2} \right) \quad (2.21)$$

L_{QCD}^0 is said to have a classical global $SU(3)_L \times SU(3)_R$ symmetry.

Applying Noether's theorem from such an invariance one would expect a total of 16 conserved currents. The currents associated with the transformations of the left-handed or right-handed quarks

$$\begin{aligned} L^{\mu,a} &= \bar{q}_L \gamma^\mu \frac{\lambda^a}{2} q_L, & \partial_\mu L^{\mu,a} &= 0, \\ R^{\mu,a} &= \bar{q}_R \gamma^\mu \frac{\lambda^a}{2} q_R, & \partial_\mu R^{\mu,a} &= 0. \end{aligned} \quad (2.22)$$

The eight currents $L^{\mu,a}$ transform under $SU(3)_L \times SU(3)_R$ as an $(8,1)$ multiplet, i.e., as octet and singlet under transformations of the left and right-handed fields,

⁴Note that in the above sense, also q is a chiral variable. However, the assignment of handedness does not have such an intuitive meaning as in the case of q_L and q_R .

respectively. Similarly, the right-handed currents transform as a $(1, 8)$ multiplet under $SU(3)_L \times SU(3)_R$. Instead of these chiral currents one often uses linear combinations,

$$V^{\mu,a} = R^{\mu,a} + L^{\mu,a} = \bar{q}\gamma^\mu \frac{\lambda^a}{2}q, \quad (2.23)$$

$$A^{\mu,a} = R^{\mu,a} - L^{\mu,a} = \bar{q}\gamma^\mu \gamma_5 \frac{\lambda^a}{2}q, \quad (2.24)$$

transforming under parity as vector and axial-vector current densities, respectively,

$$P : V^{\mu,a}(\vec{x}, t) \mapsto V_\mu^a(-\vec{x}, t), \quad (2.25)$$

$$P : A^{\mu,a}(\vec{x}, t) \mapsto -A_\mu^a(-\vec{x}, t). \quad (2.26)$$

For each conserved currents, the conserved charges are respectively:

$$Q_L^a(t) = \int d^3x q_L^\dagger(\vec{x}, t) \frac{\lambda^a}{2} q_L(\vec{x}, t), \quad a = 1, \dots, 8 \quad (2.27)$$

$$Q_R^a(t) = \int d^3x q_R^\dagger(\vec{x}, t) \frac{\lambda^a}{2} q_R(\vec{x}, t), \quad a = 1, \dots, 8 \quad (2.28)$$

which correspond to the vector charges:

$$Q^{V,a} = Q_R^a + Q_L^a \quad (2.29)$$

and, the axial charges:

$$Q^{A,a} = Q_R^a - Q_L^a \quad (2.30)$$

2.4.2 Spontaneous Symmetry breaking and Effective Lagrangian

We saw that the QCD lagrangian possesses a $SU(3)_L \times SU(3)_R$ symmetry in the chiral limit in which the light quark masses vanish. One would naively expect that hadrons organize themselves into approximately degenerate multiplets fitting the dimensionalities of irreducible representations of the group $SU(3)_L \times SU(3)_R$. While the eight vector charges annihilate the ground state

$$Q^{V,a}|0\rangle = 0 \quad (2.31)$$

the $Q^{A,a}$ do not annihilate the ground state

$$Q^{A,a}|0\rangle \neq 0 \quad (2.32)$$

i.e., the ground state of QCD is not invariant under “axial” transformations.

According to Goldstone’s theorem [18], to each axial generator Q_A^a , which does not annihilate the ground state, corresponds a massless Goldstone boson field $\phi^a(x)$ with spin 0, whose symmetry properties are tightly connected to the in question. The Goldstone bosons have the same transformation behavior under parity,

$$\phi^a(\vec{x}, t) \xrightarrow{P} -\phi^a(-\vec{x}, t), \quad (2.33)$$

i.e., they are pseudoscalars, and transform under the subgroup $H = SU(3)_V$, which leaves the vacuum invariant, as an octet:

$$[Q_V^a, \phi^b(x)] = if_{abc}\phi^c(x). \quad (2.34)$$

In the present case, we expect eight Goldstone bosons. In the hadron spectrum such massless 0^- states do not exist because the exact chiral invariance is broken by the small quark mass terms which we have neglected up to this point. Thus what we have are eight very light (but not massless) pseudo-Goldstone bosons ($\pi^\pm, \pi^0, K^\pm, K^0, \bar{K}^0, \eta$) which make up the pseudoscalar octet. Since such states are lighter than their other hadronic counterparts, we have a situation where in effective field theory can be applied—provided one is working at energy-momenta small compared to the ~ 1 GeV scale which is typical of hadrons, one can describe the interactions of the pseudoscalar mesons using an effective Lagrangian. Actually this has been known since the 1960’s, where a good deal of work was done with a *lowest order* effective chiral Lagrangian[20]

$$\mathcal{L}_2 = \frac{F_\pi^2}{4} \text{Tr}(\partial_\mu U \partial^\mu U^\dagger) + \frac{m_\pi^2}{4} F_\pi^2 \text{Tr}(U + U^\dagger). \quad (2.35)$$

where the subscript 2 indicates that we are working at two-derivative order or one power of chiral symmetry breaking—*i.e.* m_π^2 . Here:

$$U(x) = \exp\left(i\frac{\phi(x)}{F_\pi}\right), \quad (2.36)$$

$$\phi(x) = \sum_{a=1}^8 \lambda_a \phi_a(x) \equiv \begin{pmatrix} \pi^0 + \frac{1}{\sqrt{3}}\eta & \sqrt{2}\pi^+ & \sqrt{2}K^+ \\ \sqrt{2}\pi^- & -\pi^0 + \frac{1}{\sqrt{3}}\eta & \sqrt{2}K^0 \\ \sqrt{2}K^- & \sqrt{2}\bar{K}^0 & \frac{2}{\sqrt{3}}\eta \end{pmatrix} \quad (2.37)$$

where $F_\pi = 92.4$ is the pion decay constant. This Lagrangian is *unique*. It also has predictive power. Expanding to second order in the fields we find the well known Gell-Mann-Okubo formula for pseudoscalar masses[21]

$$3m_\eta^2 + m_\pi^2 - 4m_K^2 = 0 . \quad (2.38)$$

and is well-satisfied experimentally. Expanding to fourth order in the fields we also reproduce the well-known and experimentally successful Weinberg $\pi\pi$ scattering lengths. However, when one attempts to go beyond tree level, in order to unitarize the results, divergences arise and that is where the field stopped at the end of the 1960's. The solution, as proposed a decade later by Weinberg[22] and carried out by Gasser and Leutwyler[23], is to absorb these divergences in phenomenological constants, just as done in QED. What is different in this case is that the theory is nonrenormalizable in that the forms of the divergences are *different* from the terms that one started with. That means that the form of the counterterms that are used to absorb these divergences must also be different, and Gasser and Leutwyler wrote down the most general counterterm Lagrangian that one can have at one loop, involving *four-derivative* interactions

$$\begin{aligned} \mathcal{L}_4 = & \sum_{i=1}^{10} L_i \mathcal{O}_i = L_1 \left[\text{tr}(D_\mu U D^\mu U^\dagger) \right]^2 + L_2 \text{tr}(D_\mu U D_\nu U^\dagger) \cdot \text{tr}(D^\mu U D^\nu U^\dagger) \\ & + L_3 \text{tr}(D_\mu U D^\mu U^\dagger D_\nu U D^\nu U^\dagger) + L_4 \text{tr}(D_\mu U D^\mu U^\dagger) \text{tr}(\chi U^\dagger + U \chi^\dagger) \\ & + L_5 \text{tr}(D_\mu U D^\mu U^\dagger (\chi U^\dagger + U \chi^\dagger)) + L_6 \left[\text{tr}(\chi U^\dagger + U \chi^\dagger) \right]^2 \\ & + L_7 \left[\text{tr}(\chi^\dagger U - U \chi^\dagger) \right]^2 + L_8 \text{tr}(\chi U^\dagger \chi U^\dagger + U \chi^\dagger U \chi^\dagger) \\ & + i L_9 \text{tr}(F_{\mu\nu}^L D^\mu U D^\nu U^\dagger + F_{\mu\nu}^R D^\mu U^\dagger D^\nu U) + L_{10} \text{tr}(F_{\mu\nu}^L U F^{R\mu\nu} U^\dagger) \end{aligned} \quad (2.39)$$

the constants $L_i, i = 1, 2, \dots, 10$ are arbitrary (not determined from chiral symmetry alone) and $F_{\mu\nu}^L, F_{\mu\nu}^R$ are external field strength tensors defined via

$$F_{\mu\nu}^{L,R} = \partial_\mu F_\nu^{L,R} - \partial_\nu F_\mu^{L,R} - i[F_\mu^{L,R}, F_\nu^{L,R}], \quad F_\mu^{L,R} = V_\mu \pm A_\mu. \quad (2.40)$$

The bare parameters L_i which appear in this Lagrangian are not physical quantities, but an empirical numbers for each of this ten parameters as been obtained [23].

The important question to ask at this point is why stop at order four derivatives? Clearly if two-loop amplitudes from \mathcal{L}_2 or one-loop corrections from \mathcal{L}_4 are calculated, divergences will arise which are of six-derivative character. Why not include these? The answer is that the chiral procedure represents an expansion in energy-momentum. Corrections to the lowest order (tree level) predictions from one loop corrections from \mathcal{L}_2 or tree level contributions from \mathcal{L}_4 are $\mathcal{O}(E^2/\Lambda_\chi^2)$ where $\Lambda_\chi \sim 4\pi F_\pi \sim 1$ GeV is the chiral scale. Thus chiral perturbation theory is a *low energy* procedure. It is only to the extent that the energy is small compared to the chiral scale that it makes sense to truncate the expansion at the one-loop (four-derivative) level. Realistically this means that we deal with processes involving $E < 500$ MeV, and, for such reactions the procedure is found to work very well.

2.5 $\eta \rightarrow \pi^+ \pi^- \pi^0$ decay

The decay of the isoscalar η into three pions occurs primarily due to a strong isospin violation and so is in principle a process sensitive to the up-down quark mass difference. The electromagnetic corrections to the decay are small (Sutherland's theorem [48]) and modify neither rate nor the Dalitz plot distributions noticeably [49].

To lowest order in the chiral expansion the decay amplitude is given by [50]:

$$A(s, t, u) = \frac{1}{Q^2} \frac{m_K^2}{m_\pi^2} (m_\pi^2 - m_K^2) \frac{M(s, t, u)}{3\sqrt{3}F_0^2} \quad (2.41)$$

where

$$Q^2 \equiv \frac{m_s^2 - \hat{m}^2}{m_d^2 - m_u^2} = \frac{m_K^2}{m_\pi^2} \frac{m_K^2 - m_\pi^2}{(m_{K^0}^2 - m_{K^+}^2)_{QCD}} \quad (2.42)$$

is a combination of quark masses and $\hat{m} = \frac{1}{2}(m_u + m_d)$ is the average u, d quark mass, $F_0 = 92.4$ MeV is the pion decay constant and $M(s, t, u)$ contains all the dependence of the amplitude on the Mandelstam invariants. Since the decay rate is proportional to Q^{-4} ,

$$\Gamma(\eta \rightarrow \pi^+ \pi^- \pi^0) \propto |A|^2 \propto Q^{-4} \quad (2.43)$$

the transition $\eta \rightarrow 3\pi$ represents in principle an extremely sensitive probe, allowing a determination of Q . Of course, in order to extract the quark mass ratio from the

decay width, one has to provide an accurate description of $M(s, t, u)$.

At lowest order

$$M(s, t, u) = \frac{3s - 4m_\pi^2}{m_\eta^2 - m_\pi^2}. \quad (2.44)$$

a well known result, already obtained using Current Algebra. To cross-check the validity of the theoretical description one can use the Dashen theorem ⁵ [51] to determine Q :

$$Q_{Dashen}^2 = \frac{m_K^2}{m_\pi^2} \frac{m_K^2 - m_\pi^2}{m_{K^0}^2 - m_{K^+}^2 + m_{\pi^+}^2 - m_{\pi^0}^2} \quad (2.45)$$

and integrate $M(s, t, u)$ over the phase space to predict the decay width, which has been determined quite accurately. Numerically, $Q_{Dashen} = 24.1$ and the corresponding prediction for the decay rate using LO result eq.(2.44) is:

$$\Gamma^{theo} (\eta \rightarrow \pi^+ \pi^- \pi^0) = 88 \text{ eV} \quad (2.46)$$

in strong contradiction to the experimental result[65]:

$$\Gamma^{exp} (\eta \rightarrow \pi^+ \pi^- \pi^0) = 291 \pm 22 \text{ eV}. \quad (2.47)$$

A one-loop calculation within conventional chiral perturbation theory (χ PT) [53], improve the result considerably

$$\Gamma^{theo} (\eta \rightarrow \pi^+ \pi^- \pi^0) \simeq 167 \pm 50 \text{ eV}. \quad (2.48)$$

but still fails in being in agreement with phenomenological value.

Further corrections discussed in the literature [52] may slightly increase the theoretical result, but cannot account for the large discrepancy to the data. On the other hand, a significant violation of the Dashen theorem (and thus a different value for Q) could easily account for the discrepancy, but can be demonstrated only after comparison of the theoretical prediction for $M(s, t, u)$ with the experimental findings for the dynamics of the decay. The above discussion motivates a precise measurement of the $\eta \rightarrow 3\pi$ dynamics via the study of the Dalitz plot, object of this thesis.

⁵The Dashen theorem states that in the chiral limit the electromagnetic part of the kaon and pion electromagnetic mass shifts are the same: $(m_{\pi^+}^2 - m_{\pi^0}^2)_{em} = (m_{K^+}^2 - m_{K^0}^2)_{em}$

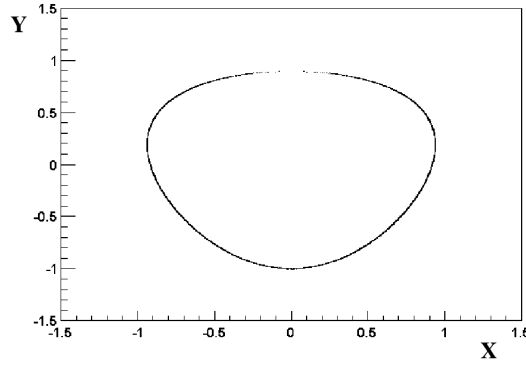


Figure 2.5: Relevant phase-space for the decay $\eta \rightarrow \pi^+ \pi^- \pi^0$.

2.6 Brief review of experimental and theoretical results on the Dalitz plot parameters

The dynamics of the $\eta \rightarrow \pi^+ \pi^- \pi^0$ decay can be studied with the usual method of the Dalitz plot analysis. It is based on the fact that in the centre of mass system, a 3-body decay has 2 free parameters. The choice of this pair of variables can be done in several way. Conventionally one uses the kinetic energies of the particles T_+ , T_- and T_0 in the η rest frame and defines:

$$X = \sqrt{3} \frac{T_+ - T_-}{Q_\eta} = \frac{\sqrt{3}}{2M_\eta Q_\eta} (u - t) \quad (2.49)$$

$$Y = \frac{3T_0}{Q_\eta} - 1 = \frac{3}{2M_\eta Q_\eta} [((m_\eta - m_{\pi^0})^2 - s)] - 1 \quad (2.50)$$

$$Q_\eta = m_\eta - 2m_{\pi^+} - m_{\pi^0} \quad (2.51)$$

where X and Y are respectively define in the range $[-1, 1]$ and $[-1, 0.895]$.

In the $X - Y$ plane the accessible phase-space is limited to the region shown in fig.2.5. The shape of the contour show that we are in an intermediate situation respect to the fully relativistic situation (a circle) and the non relativistic one (a triangle). The amplitude decay $A(X, Y)$ is then expanded about the center of Dalitz-plot as:

$$|A(X, Y)|^2 \simeq 1 + aY + bY^2 + cX^2. \quad (2.52)$$

The amplitude is symmetric in X , therefore no odd power of X occurs in $|A(X, Y)|^2$. The theoretical and experimental measurements of the slopes parameters are listed in Tab.2.1 and 2.2. Unfortunately both experimental and theoretical scenario are not

	a	b	c
<i>tree</i>	-1.00	0.25	0.00
<i>one-loop</i> [53]	-1.33	0.42	0.08
<i>dispersive</i> [54]	-1.16	0.26	0.10
<i>tree dispersive</i> [52]	-1.10	0.31	0.001
<i>absolute dispersive</i> [52]	-1.21	0.33	0.04

Table 2.1: Theoretical results for the slope parameters of the various approximations.

	N_η	a	b	c
<i>Layter</i> [55]	80884	-1.08 ± 0.14	0.034 ± 0.027	0.046 ± 0.031
<i>Gormley</i> [56]	30000	-1.17 ± 0.02	0.21 ± 0.03	0.06 ± 0.04
<i>Crystal Barrel</i> [57]	1077	-0.94 ± 0.15	0.11 ± 0.27	
<i>Crystal Barrel</i> [58]	3230	-1.22 ± 0.07	0.22 ± 0.11	0.06 fixed

Table 2.2: Experimental results for the slope parameters.

clear. All the measurements are characterized by quite large uncertainties, moreover the parameter values are difficult to compare because making assumptions on the values of the quadratic slope significantly alters the fitted results of the others. A new measurement of the spectral shape, with higher statistics, would allow to determine whether the existing disagreement between experimental findings and the theoretical predictions based on χ PT are caused by an inaccurate value for the $d - u$ quark mass difference or to the importance of higher order final state interaction effects.

Chapter 3

Reconstruction procedure and Event Classification at KLOE

In this chapter we will describe the reconstruction procedure with the event classification technique adopted at the KLOE experiment.

The reconstruction of charged particles trajectories and of neutral energy clusters with high efficiency and good resolution on their parameters plays a key role for succeeding in the main physics analysis at KLOE.

A study of the performance of the reconstruction package is presented in the first part of this chapter.

In order to perform the analysis of the huge amount of data, that KLOE has acquired, within reasonable times and computing power, an Event Classification program has been designed. It selects different topologies of events using only the information coming from the reconstruction chain, and store them on different data streams. Its main features for the $\eta \rightarrow \pi^+ \pi^- \pi^0$ analysis is described in the second part of the chapter.

3.1 Track reconstruction

The algorithms used at KLOE to reconstruct charged tracks are mostly based on those developed by the ARGUS Collaboration [26], adapted to the KLOE detector. The reconstruction is performed into three steps, i.e.:

- Pattern Recognition (PR): groups the measured drift chamber hits into track candidates and gives a first estimate of the track parameters;
- Track Fit (TF): evaluate precisely the track parameters by means of an iterative procedure;
- Vertex Fit (VF): finds the position of the charged vertices by means of an iterative procedure.

In the following section we will give some details on these steps.

3.1.1 Pattern recognition

The KLOE drift chamber has a peculiar structure: the wires make alternatively positive and negative stereo angles with respect to the z direction.

When projected onto the xy plane, the hits are distributed on 2 nearby curves, one made up by the hits which fire the *positive* stereo angle wires and the other one by the hits firing the *negative* wires.

The pattern recognition procedure first combine the hits of each *view* separately, defining 2 track candidates for each view, and using only 2D information. The 2D candidates are then matched and merged to define the final track candidate. The z information is extracted from the merging of the two views. A first evaluation of the parameters describing the trajectory is given.

3.1.2 Track fit

The KLOE track fit [27], [28], [29] is a least-square fit of the track candidates coming from the pattern recognition. The fit yields parameters \vec{q} which minimises¹ the quadratic form:

$$\chi^2 = [\vec{d}_{meas} - \vec{d}(\vec{q})]^T W [\vec{d}_{meas} - \vec{d}(\vec{q})] \quad (3.1)$$

¹The vector of parameters for a fit to an helix has dimension five, a possible choice of the parameters being the track curvature $k = Q/P_t$, the value of $\cot \theta = P_z/P_t$, and of $\phi = P_y/P_x$, d_0 and z_0 at the first point. In case multiple scattering is considered the scattering angles are treated as additional parameters and the vector has dimension > 5 .

where \vec{d}_{meas} are the measured drift distances and $\vec{d}(\vec{q})$ are the theoretical distances of closest approach and W is the inverse covariance matrix of the measured coordinates. The minimisation is performed using an iterative procedure in which the track model is linearised.

The positions of the track points and their tangents are determined by using the values of the position and momentum of the first point (coming from the pattern recognition) and recurrent relations giving the momenta and positions of successive hits. Energy loss and multiple scattering suffered by particle in crossing the chamber are taken in account.

The track fit procedure contains also some additional features designed to increase the performance of the hits assignment using the parameters available at the TF level, more refined than the ones available at PR level.

These are:

- **Hit Addition:** a try is made to add hits that were not associated to any track candidate by the pattern recognition. Each hit is added or not on the basis of its contribution to the χ^2 .
- **Hit rejection:** hits associated to tracks by the pattern recognition may be removed if their contribution to the χ^2 is too large.
- **Track Joining:** [30] since the pattern recognition groups the hits to form the track candidates going from the outer part to the inner part of the drift chamber, long tracks may be not identified as a whole and split into separated candidates. One then tries to put these stumps together in order to recover the original track.
- **Track splitting:** in a non negligible percentage of cases, a track candidate coming from the pattern recognition algorithm is composed of two successive chains of hits belonging to different physical tracks. An algorithm has been developed [31] in order to correct this situation.

3.1.3 Vertex fit

After reconstructing tracks, the vertex fit [32] aims to reconstruct the positions of the decay vertexes in the DC volume.

In order to reconstruct the ϕ decay vertex tracks are extrapolated toward the nominal interaction point, taking into account the energy losses on the DC inner walls. For the other vertexes an iterative procedure is used to obtain the point of closest approach for all tracks. Pairs of tracks are searched, whose trajectories show an acceptable crossing point, both in the $x - y$ plane and along the z coordinate. A χ^2 minimization is applied in order to obtain the best possible estimate of the vertex position, and if such procedure converges, the vertex is kept.

Vertexes are classified according to the quality of the fit. At this level, even more than one vertex can belong to a given track. A merging procedure is performed to join 2-tracks vertexes together, so obtaining vertexes with 3 or more tracks (this is particularly relevant for the $K^\pm \rightarrow \pi^\pm \pi^+ \pi^-$ decay). An hypothesis test which compares the 4-tracks vertexes versus the 2-tracks vertexes is done. On the bases of the χ^2 the two hypotheses are taped.

3.2 Cluster reconstruction

The reconstruction of the event begins from the calorimeter information. Groups of adjacent or close cells are merged together to build clusters by the clustering algorithm.

The cells are included in the cluster search only if times and amplitudes are available from both sides of the fibers. If a cell is missing just one of time and amplitude signals, it is named "incomplete" cell. For the barrel, an "incomplete" cell is recovered on the basis of the difference $\Delta\phi$ between its azimuth and that of the closest cluster. Incomplete cells are assigned to the cluster if $|\Delta\phi| < 3^\circ$. A similar procedure is used for the end-caps using the transverse coordinate x . The cluster energy E_{cl} , is the sum of the energies of all the cells assigned to it.

The cluster position (x_{cl}, y_{cl}, z_{cl}) , and the cluster time t_{cl} , are computed as energy-weighted averages of the cell variables:

$$x_{cl} = \frac{\sum_{cells} E_i x_i}{\sum_{cells} E_i}, \quad y_{cl} = \frac{\sum_{cells} E_i y_i}{\sum_{cells} E_i}, \quad z_{cl} = \frac{\sum_{cells} E_i z_i}{\sum_{cells} E_i}, \quad t_{cl} = \frac{\sum_{cells} E_i t_i}{\sum_{cells} E_i}.$$

The coordinate along the direction of the fibers is computed using the times at both sides, while the two orthogonal coordinates are taken from the nominal position of the cells.

A significant systematic effect induced by the clustering is the production of spurious clusters from the splitting of a unique energy deposit in the calorimeter. This effect is strongly dependent on the energy of the particle releasing its energy and on the position of the cluster in the EMC and affects the photon multiplicity observed by the detector in a given event.

For this reason it has been studied on well-define photons samples such as those produced in $e^+e^+ \rightarrow e^+e^+\gamma$ events and in ϕ radiative decays. The probability of having a cluster splitting is computed as a function of cluster energy and polar angle, and is finally used to unfold the true multiplicities from the observed ones.

After cluster reconstruction, an estimate of the reference time of the event (the absolute T_0) is given by assuming that the first cluster in time is due to a prompt photon coming from the origin; this photon must have at least 50 MeV and must lie farther than 60 cm from the collision axis. The hypothesis of the being a prompt cluster reasonably fits a large set of events as radiative ϕ decays.

3.3 The KLOE Event Classification EVCL

The aim of the Event Classification program [33], is to perform a fast identification of the ϕ decays at the same time data are acquired and to store them in different *streams*. In this way tapes with homogeneous data are available, and each different analysis run only on a reduced set of tapes, with a big saving in time and CPU power. The KLOE trigger acquires the events with an efficiency greater than 99%. At the same time, background events (cosmic rays, Bhabha events and machine background) have to be strongly rejected by the trigger, to avoid to overload the KLOE Data Acquisition. The raw data are immediately stored on tapes and processed.

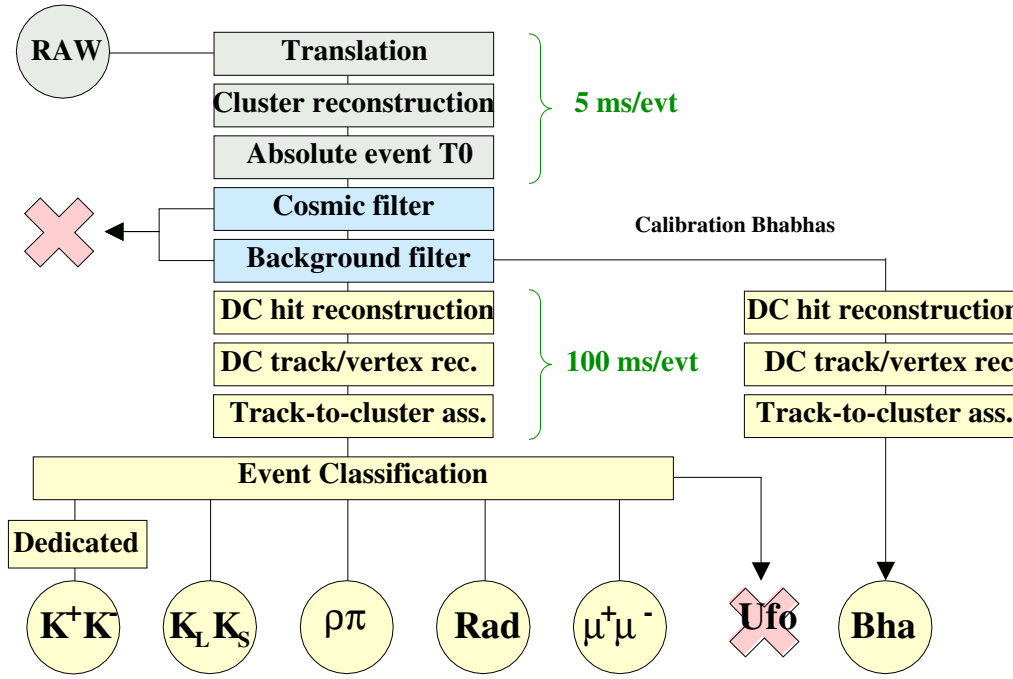


Figure 3.1: Event Classification block scheme.

The Event Classification procedure tags the event type and performs the splitting of the ϕ decays in different streams, fig.3.1.

A *stream* is a collection of events which are all selected by one definite algorithm. The four main streams are:

- **Stream 1:** $\phi \rightarrow K^+ K^-$;
- **Stream 2:** $\phi \rightarrow K_L K_S$;
- **Stream 3:** $\phi \rightarrow \rho\pi$, $\phi \rightarrow \pi^+ \pi^- \pi^0$;
- **Stream 4:** $\phi \rightarrow$ radiative events; ($\eta\gamma, \eta'\gamma, \pi^0\gamma, f^0\gamma, \dots$)

In addition to these there are other streams, in which Bhabha and cosmic events used for detectors calibration are stored for example. An event is assigned to a certain stream when at least one of its algorithms identifies it. When an event is flagged by two (or more) algorithms of *different* streams the strategy followed is to write this

event in all these streams, in order not to lose efficiency. The identification process provides a lot of informations about the particles present in the events, which are collected in a compact way in the ECLO bank, Event CLassification Object (particles) bank. This bank consists of a set of words, one for each particle tagged by some algorithm, and these words content a number that identifies the particle (the particle ID as the GEANT convention), the bank number of the fitted track, for charged particle, the bank number of the reconstructed cluster, for neutral particle; the bank number of the vertex connected to the track or to the cluster. Another information accessible in the ECLO bank is the tagging ID, which have two meanings: it contents the stream number and a flag that specify the algorithm that selected the event.

3.3.1 Stream 4: Charged/neutral radiative decays

We can define the following set of variables:

- $P_\Sigma = |\vec{p}_1| + |\vec{p}_2|$
- $\delta E = |\vec{p}_1 + \vec{p}_2| - (M_\phi - \sqrt{m_\pi^2 + |\vec{p}_1|^2} - \sqrt{m_\pi^2 + |\vec{p}_2|^2})$
- $\beta = r_{cl}/cT_{cl}$
- N_{pnc} number of neutral cluster with $0.9 < \beta < 1.1$ and $E > 7$ MeV

The P_Σ variable allow discrimination with respect to the $K^+ K^-$ and to the $K_S K_L$ events. The δE quantity is zero only in the case of $\pi^+ \pi^- \gamma$ final state, and allow to separate the three pions final state from other final states characterised by two charged tracks with high momentum and one prompt photon ($\pi^+ \pi^- \gamma$, $\mu^+ \mu^- \gamma$ or $e^+ e^- \gamma$). The selection procedure is the following:

- one and only one charged vertex in the interaction region
- cut on the plane P_Σ vs. δE depending on the specific final state (see fig 3.2)
- $0 < N_{pnc} < 3$.AND. $E_{prompt} > 50$ MeV

The cuts are tuned for each of the different final states:

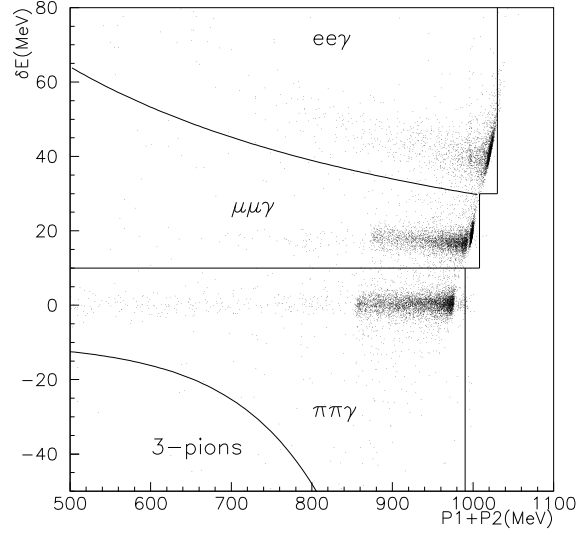


Figure 3.2: Scatter-plot of δE vs. P_{Σ} for $\pi^+\pi^-\gamma$, $\mu^+\mu^-\gamma$ and $e^+e^-(\gamma)$ events. The MC generation of $\pi^+\pi^-\gamma$ and $\mu^+\mu^-\gamma$ is done only for events with $E_{\gamma} < 100$ MeV, so the 2 bands are clearly artificially cut. The low P_{Σ} tail of $\pi^+\pi^-\gamma$ events is due to $\rho^{\pm}\pi^{\pm}$ where $\rho^{\pm} \rightarrow \pi^{\pm}\gamma$ that are included in the $\pi^+\pi^-\gamma$ sample.

- $\pi^+\pi^-\gamma$, $\mu^+\mu^-\gamma$ and $e^+e^-\gamma$

The scatter plot of the δE vs. P_{σ} (see fig. 3.2) shows very well the cuts that must be applied in order to identify these three decays. The quantity δE is zero only for $\pi^+\pi^-\gamma$ final states, while it gets positive values for $\mu^+\mu^-\gamma$ and $e^+e^-\gamma$.

- $\pi^+\pi^- + n\gamma$ with $n \geq 2$

Among the many possible final states belonging to this category the developed algorithm selects the most relevant from the analysis point of view, i.e. $\eta\gamma$, $a_0\gamma$ and $\eta'\gamma$. Again cuts in the $\delta E - P_{\sigma}$ plane are applied (see fig. 3.3). Due to the similar kinematics the decay chain $\eta'\gamma \rightarrow \rho\gamma\gamma$ can be easily (50 % of times) misidentified as a three pion final state.

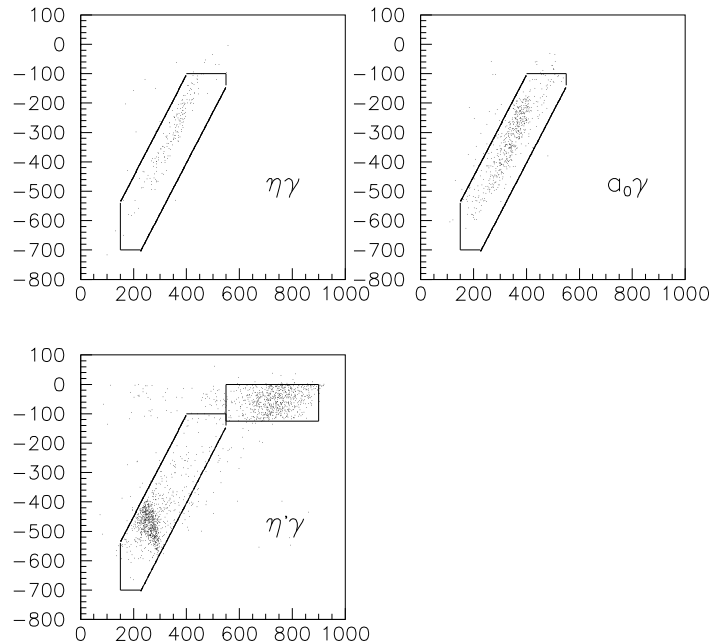


Figure 3.3: Scatter-plot of δE vs. P_{Σ} for $\eta\gamma$, $a_0\gamma$ and $\eta'\gamma$ events. The allowed area for radiative decays are shown. The second area for the $\eta'\gamma$ case partly overlaps the 3-pion area.

3.4 Background rejection (FILFO)

Before the track fit process, which is the most time consuming from the CPU viewpoint, data need to be filtered from the residual sources of background. To attain this goal, a dedicated procedure, FILFO[34], has been developed: it is based on algorithms which work on elementary and unreconstructed quantities to identify and reject cosmic-ray and machine background events that have not been ruled out at the trigger level. Main categories of background are:

- cosmic rays
- Bhabha scattering
- machine background

Cosmic rays rejection. Cosmic rays rate with the calorimeter trigger only is ~ 2.6 kHz and after the cosmic veto is reduced to ~ 700 Hz.

Simple considerations on the nature of the cosmic radiation help to its rejection. Cosmic rays come from outside of the detector and then the time on the outer plane of the earliest cluster must be smaller than the time of the last plane of the same cluster. The excellent time resolution of the calorimeter allows to see this tiny time difference that is smaller than 1 ns.

In addition cosmic rays that pass the magnet iron yoke are mainly penetrating particles, namely muons, that can be identified looking at the ratio between the energy deposited in the outer and in the inner calorimeter plane.

These simple ideas have been improved trying to minimize the inefficiency on ϕ decays. In particular constraints on the time difference between the first two clusters in time and at the number of hits in the drift chamber can identify a particle crossing all the detector. Also the shower depth defined as:

$$D = \frac{\sum i \cdot E_i}{E_{clus}} \quad (3.2)$$

give a more refined information than the simple ratio between the energy deposit in the first and the last plane. The efficiency in cosmic rejection is $\sim 95\%$ [35].

Bhabha rejection 'Normal' Bhabha events can be easily identified by the trigger veto and then rejected or selected for calibration purposes looking at the corresponding bit in the trigger mask. As particular category of Bhabha events in which the particles hit the quadrupoles or the calorimeter around the quadrupoles electromagnetic showers evade the trigger veto since their energy is partially absorbed by quadrupole material and partially spread out over more than one trigger sector.

Also in this case, by the way, the event topology keeps memory of Bhabha event characteristic. Events can be rejected for cuts on: a) the total number of clusters; b) the spread around the axis defined by the line connecting the energy centroids on the two endcaps; c) the energy of the two most energetic clusters.

Rejection efficiency on Bhabha events is of the order of $\sim 80\%$.

Machine background rejection. Machine backgrounds are mainly due to photons, electrons or positrons produced by some electromagnetic interaction involving the beams: the main sources are Coulomb scattering on residual gas inside the beam pipe, bremsstrahlung and intra-beam interactions (Touscheck effect).

All these processes mostly produce particles with very small inclination with respect to the beam pipe. Some particle at large angle is also observed but is mainly due to some interaction with quadrupoles inside the detector.

Selection cuts exploit: a) the polar angle with respect to the beam pipe of the two most energetic clusters; b) the energy weighted average polar angle; c) the number of planes hit by the most energetic cluster versus its energy; d) the number of the hits in the inner cells of the drift chamber with respect to the total number of hits; e) the total calorimeter energy when only few chamber wires have been hit.

The rejection efficiency of all these cuts depends on the machine background topology that varies from run to run, so it oscillates between 50 and 90%.

3.5 A minimum bias EVCL filter for ϕ radiative decays

In order to study the systematic bias introduced by FILFO and EVCL algorithm, see sec.5.4.4 a downscaled sample with less stringent event classification cuts for events in radiative stream has been produced [63].

We have produced streamed files without using both FILFO and EVCL for 2001 and 2002 data taking period. The integrated luminosity of all streamed files for the $\eta \rightarrow \pi^+ \pi^- \pi^0$ decay is $L_{int} \simeq 23 \text{ pb}^{-1}$.

The selection uses calorimetric informations and retains events with the following requirements:

- at least 3 clusters in time, with a time window of $5 \sigma_{T_{clu}}$, and a cutoff of 5 ns;

- only clusters over 18° ;
- a cut on the total cluster energy $\sum E_{all_clu} > 500$ MeV, with no requirements on track to cluster association, including out of time clusters.

On a MC sample the efficiency of minimum bias algorithm versus the standard radiative stream has been studied. We find that the minimum bias efficiency on events selected by radiative stream is 84%; if we look at the events not selected by radiative stream, we find that minimum bias recover 54% of them. That means that the minimum bias events could be a good sample to test standard EVCL performance.

Chapter 4

Analysis of $\eta \rightarrow \pi^+ \pi^- \pi^0$

The study of the $\eta \rightarrow \pi^+ \pi^- \pi^0$ dynamic, through a fit to the Dalitz plot distribution, is presented. The Dalitz plot distribution is conventionally described in terms of two variables $X \propto T_+ - T_-$ and $Y \propto T_0$ (where T is the kinetic energy of pions in the η -rest frame) and it is parametrized as following:

$$|A(X, Y)|^2 = 1 + aY + bY^2 + cX + dX^2 + eXY$$

In this chapter we refer only to the MonteCarlo simulation. The selection criteria for the analysis are defined in section 4.1 while the evaluations of resolution and efficiencies involved in the measurement are reported in section 4.3.

After a short description of the method applied to fit the Dalitz plot distribution, the results on MonteCarlo sample are discussed in detail in section 4.5.

4.1 Selection of $\eta \rightarrow \pi^+ \pi^- \pi^0$ decays

At KLOE η is produced through the process $\phi \rightarrow \eta\gamma$, so to study the dynamic of $\eta \rightarrow \pi^+ \pi^- \pi^0$ the final state is $\pi^+ \pi^- \gamma\gamma\gamma$ which corresponds to a BR value of:

$$BR_{TOT} = BR(\phi \rightarrow \eta\gamma) \times BR(\eta \rightarrow \pi^+ \pi^- \pi^0) \times BR(\pi^0 \rightarrow \gamma\gamma) = 2.9 \cdot 10^{-3} \quad (4.1)$$

There is no combinatorial problem in the photon pairing because the $\phi \rightarrow \eta\gamma$ is characterized by a high energy monochromatic recoil photon, $E_{\gamma_{rec}} \sim 363$ MeV, very

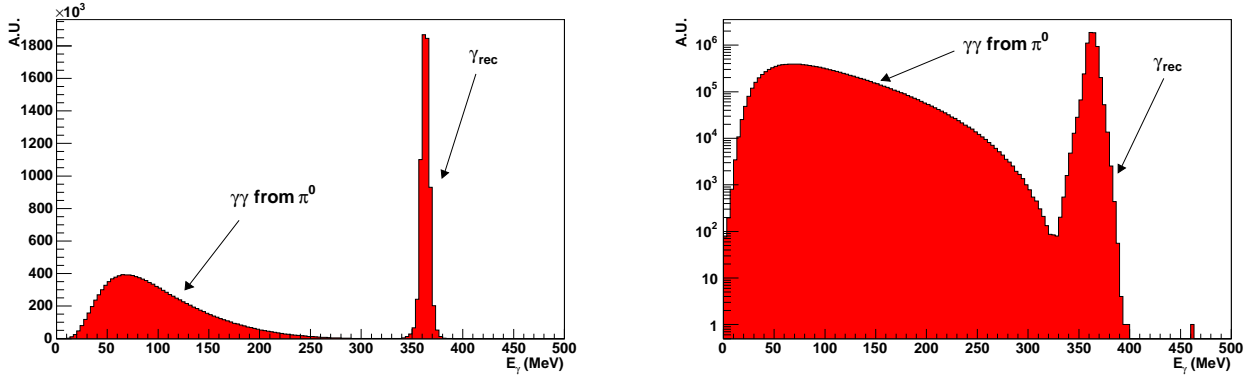


Figure 4.1: MonteCarlo photon energy spectrum. Left: linear scale; Right: log scale.

well separated from the energy of the photons coming from π^0 decay (see fig. 4.1). Background events can rise from:

1. $\phi \rightarrow K_S K_L$ events with one charged vertex where at least one photon is lost and the K_L is decaying near the interaction point (IP).
2. $\phi \rightarrow \pi^+ \pi^- \pi^0$ events with an additional photon in the detected due to accidental photons or splitting of clusters in the electromagnetic calorimeter.

4.1.1 Selection cuts

The events selection is performed through the following step:

1. Events are selected starting from the radiative stream with charged particles, cfr.3.3.1.
2. One charged vertex is required inside the cylindrical region $r < 4$ cm, $|z| < 8$ cm and 3 prompt neutral clusters ¹ (pnc) with $\theta_\gamma > 21^\circ$ and $E_\gamma > 10$ MeV.

¹A pnc is defined as a cluster in the EmC with no associated track coming from the Drift Chamber (DC) and $|(t - \frac{r}{c})| < 5\sigma_t$ where t is the arrival time on the EmC, r is the distance of the cluster from the IP and c is the speed of light and $\sigma_t = 54 \text{ ps}/\sqrt{E(\text{GeV})} \oplus 147 \text{ ps}[60]$.

To reduce the problem of cluster splitting a cut on the opening angle between each couple of photons is done $\theta_{i,j} > 18^\circ$.

3. $E_{prompt}^2 < 800 \text{ MeV}$. This cut is already present in the EVCL algorithm. We repeat it at the analysis level to remove few events selected in the radiative stream by different algorithms.
4. A constrained kinematic fit is performed requiring 4-momentum conservation and the speed of light for each photon, without imposing mass constraint both on η and π^0 . See Appendix A for a details on kinematic fit.

A cut on the χ^2 probability is done, $\mathcal{P}(\chi^2) > 1\%$.

The effect of this fit on the event reconstruction is to improve significantly the resolution on photon energies and invariant masses. We note in passing that the distribution of the χ^2 variable of the fit shows a better agreement data - MonteCarlo than it was in the past [62](see fig. 4.2) due mainly to the improvements in MonteCarlo simulations.

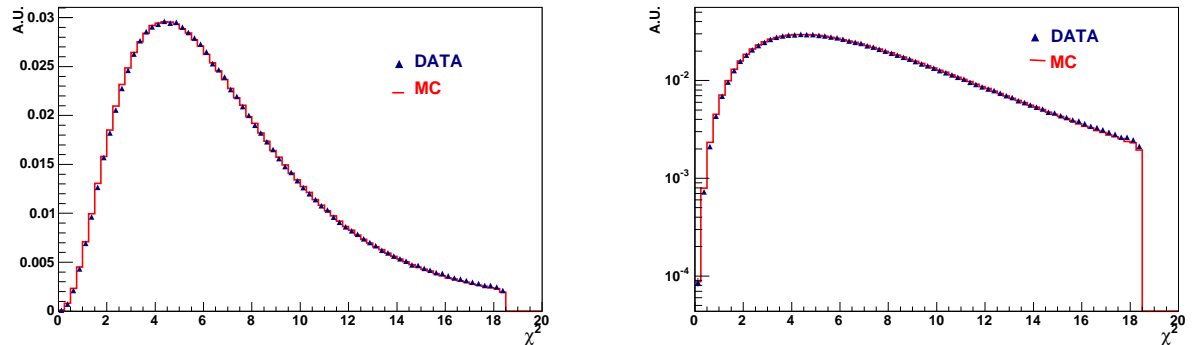


Figure 4.2: χ^2 distribution. Left: linear scale; Right: log scale.

5. Finally we require:

- $320 \text{ MeV} < E_{\gamma rec} < 400 \text{ MeV}$ (reduces the residual background from $\phi \rightarrow K_S K_L$ events).

²For every event the prompt energy is defined as the sum of the energies of all the pnc

- $E_{\pi^+} + E_{\pi^-} < 550$ MeV (reduces the residual background from $\phi \rightarrow \pi^+ \pi^- \pi^0$ events).
- $M_{\gamma\gamma} \in [110, 160]$ ³ (reduces the residual background from $\phi \rightarrow \eta\gamma$ events, with $\eta \rightarrow \pi^+ \pi^- \pi^0$ and $\pi^0 \rightarrow e^+e^-\gamma$; and from $\phi \rightarrow \eta\gamma$ events, with $\eta \rightarrow \pi^+ \pi^- \gamma$). Fig. 4.3 shows the comparison data MonteCarlo for the variable used in the cut, the observed discrepancy is due to the presence of background.

After this cuts the overall selection efficiency is $\varepsilon = (34.1 \pm 0.2)\%$

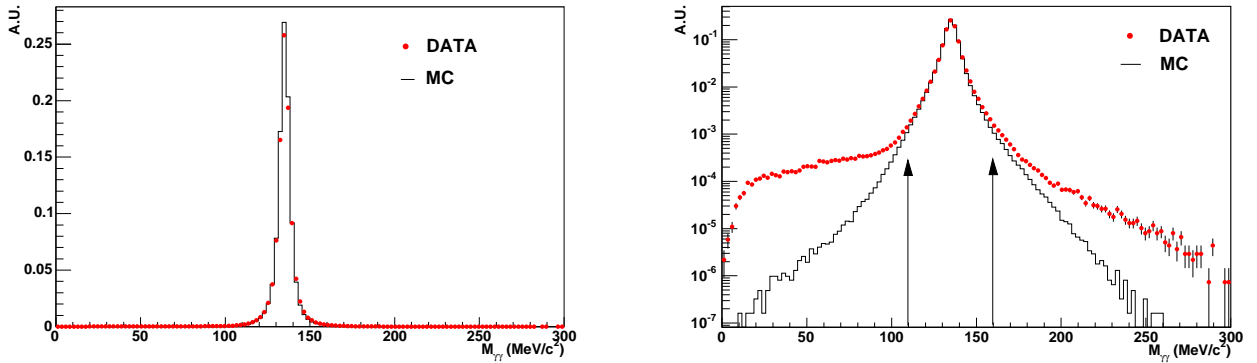


Figure 4.3: Data vs MonteCarlo comparison for the invariant mass of the two softest photons in $\pi^+ \pi^- \gamma\gamma$ events. Left: linear scale; Right: log scale. The arrows show the cut applied. The histograms are normalized to the same area.

4.2 Selection efficiency

For the different steps of selection the relative efficiencies are estimated. In particular:

- The trigger efficiency evaluated by MonteCarlo is 99.9%, so the effect of trigger in the uncertainties evaluation has been neglected. The good data-MonteCarlo agreement for the trigger sector multiplicities is shown in fig. 4.4.

³ $M_{\gamma\gamma}$ is the invariant mass of the two softest photons in $\pi^+ \pi^- \gamma\gamma$ events.

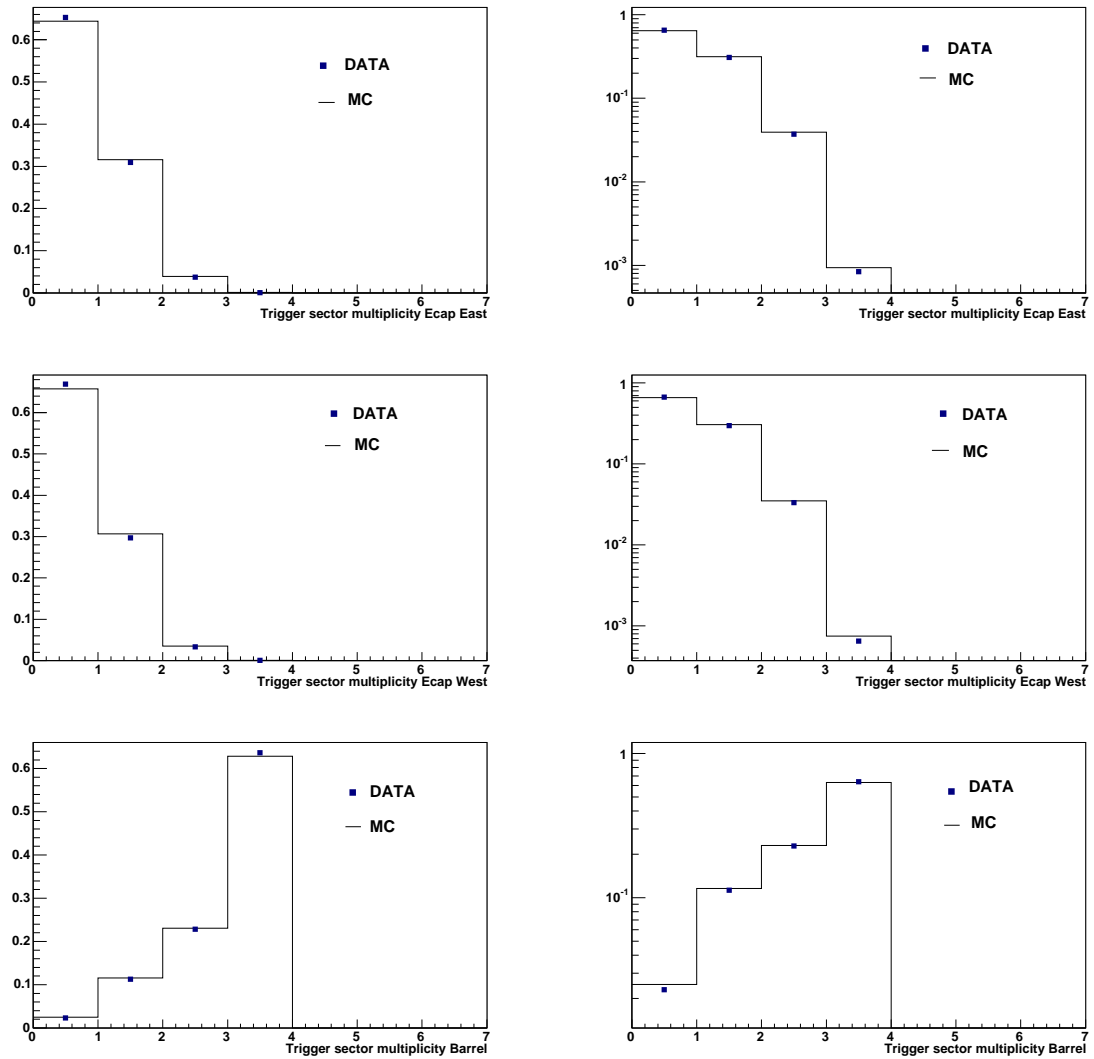


Figure 4.4: Trigger sector multiplicity. From top to bottom: endcap East, endcap West, barrel. Left: linear scale. Right: log scale.

- The effect of the event classification procedure (EVCL) and machine background filter (FILFO) is evaluated using a downscaled sample, minimum bias, with less stringent event classification cuts, cfr. 3.5.

The efficiency of minimum bias algorithm has been evaluated on a MonteCarlo sample, we find on events selected by the analysis

$$\varepsilon = (99.88 \pm 0.01)\% \quad (4.2)$$

this means that the minimum bias events provide a good sample to test the bias introduced by EVCL procedure. The selection procedure has been applied to this data sample without using the EVCL selection and the result has been compared to the selection procedure including EVCL applied on the same data set. A similar analysis has been done to check FILFO. While the FILFO algorithm is absolutely negligible, the EVCL procedure introduces an inefficiency of $\sim 1.5\%$ on the selected events. In the following, the effect of this bias on the parameters measurement will be analysed.

No difference between data and MonteCarlo on the overall efficiency is observed:

$$\varepsilon_{EVCL}^{data} = (98.53 \pm 0.07)\% \quad (4.3)$$

$$\varepsilon_{EVCL}^{MC} = (98.55 \pm 0.01)\%. \quad (4.4)$$

- The tracking and vertex efficiencies have been checked selecting $\phi \rightarrow \pi^+ \pi^- \pi^0$ from raw data. The $\phi \rightarrow \pi^+ \pi^- \pi^0$ decay is very useful for this kind of study, because it cover the $\pi^+ \pi^-$ momentum range under study.

We look for events characterized by two tracks in the chamber with momentum $50 \text{ MeV} < P < 400 \text{ MeV}$ and two prompt neutral cluster over 25σ . We ask for $|M_{\gamma\gamma} - M_{\pi}| < 20 \text{ MeV}$ and $850 \text{ MeV} < E_{tot} < 1200 \text{ MeV}$ for the total energy. The background contamination is at level of 1.5% . We studied the vertex efficiency as function of the minimum pion momentum; we compare the MC vertex efficiency with the one on data.

From the fit with a constant in the range $50 \text{ MeV} \div 250 \text{ MeV}$, we found

$$\frac{\varepsilon_{data}^{VTX}}{\varepsilon_{MC}^{VTX}} = 0.990, \quad (4.5)$$

see fig.4.5-bottom. The same has been done for the track efficiency, with ad-

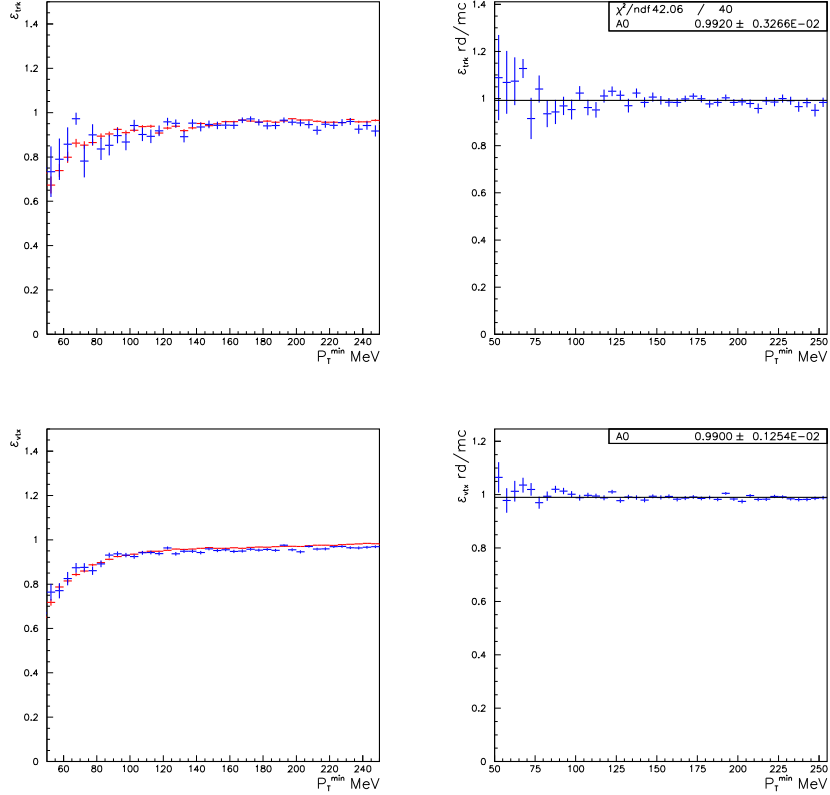


Figure 4.5: Left: Tracking (upper plot) and Vertex (lower plot) efficiency as function of minimum P_T of the two tracks. Right: Data (blue) MonteCarlo (red) ratio for the tracking (upper plot) and vertex (lower plot) efficiencies.

ditional cuts. We ask for other two clusters in the calorimeter with at least 100 MeV and $0.8 < \beta < 0.95$, in this way we close the event. We study the efficiency for a single track, so we ask at least one track in the DC with $200 \text{ MeV} < P < 400 \text{ MeV}$. Using this track and the two prompt neutral clusters we built the missing momentum. We look for a second track in a cone of 35° around the direction of the missing momentum. We compare the MonteCarlo track efficiency with the one on data.

From the fit with a constant in the range $50 \text{ MeV} \div 250 \text{ MeV}$, we found

$$\frac{\varepsilon_{data}^{TRK}}{\varepsilon_{MC}^{TRK}} = 0.992, \quad (4.6)$$

see fig.4.5-top. The data-MonteCarlo ratio of efficiencies is flat all over the momentum spectrum, thus introducing no bias in the Dalitz plot fit. We must stress that all the variables used in the fit are evaluated in the η rest frame, which is boosted with respect to the laboratory by about 363 MeV. This means that the content of each bin in momentum in the LAB frame is actually distributed all over the momentum range in the η cms used for the fit: any data-MonteCarlo discrepancy in the LAB system is further diluted by this effect.

The data-MonteCarlo ratio of the overall tracking and vertex efficiencies is :

$$\frac{(\varepsilon_{TRK}^2 \varepsilon_{VTX})_{data}}{(\varepsilon_{TRK}^2 \varepsilon_{VTX})_{MC}} = 0.974 \pm 0.006. \quad (4.7)$$

4.3 Resolution and efficiency on Dalitz-plot variables

The Dalitz-plot variables are evaluated using the measured momenta of the pions boosted in to the η rest frame. In particular, the four-momenta of the pions are obtained: for π^\pm , from the track parameters (curvature, azimuthal-angle ϕ and $\cotg \theta$) and for π^0 , from the information about the photons generated in the π^0 decay (E, x, y, z, t for each photons).

The resolution on the Dalitz variables (X, Y) is shown in fig. 4.6 where the differences between the reconstructed values (X_{rec}, Y_{rec}) and the true values (X_{gen}, Y_{gen}) are plotted. A sum of 4 gaussians nicely fits each of the two distribution. The width of the “core” gaussian

$$\delta X = 0.020 \qquad \delta Y = 0.026 \quad (4.8)$$

gives an estimate of the resolution.

In order to improve the resolution on Y variable we note that a second way to compute Y is possible. In fact, we can obtain the kinetic energy of π^0 from the π^+ and π^- energy:

$$T_0^{ch} = M_\eta - (E_{\pi^+} + E_{\pi^-}) - M_{\pi^0} \quad (4.9)$$

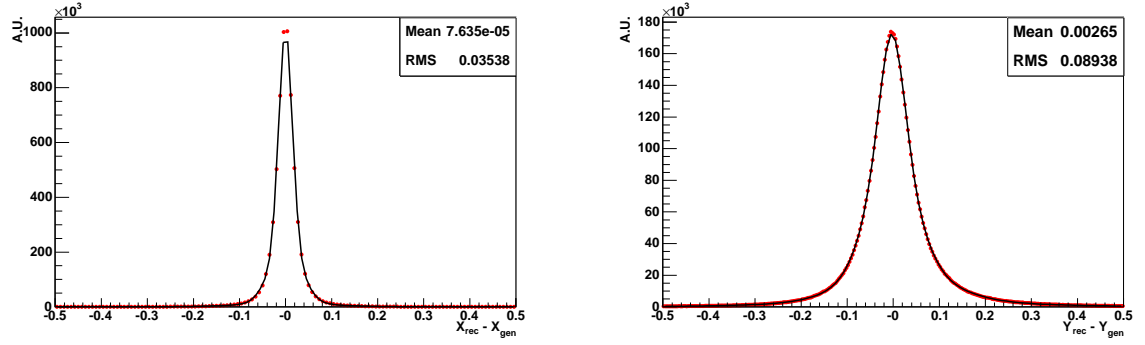


Figure 4.6: MonteCarlo distributions of resolutions: X (left) and Y (right). The curves are fitted to a sum of four gaussians.

so we define:

$$Y_{ch} = \frac{3T_0^{ch}}{Q_\eta} - 1 \quad (4.10)$$

which is slightly better in resolution (see fig. 4.7)

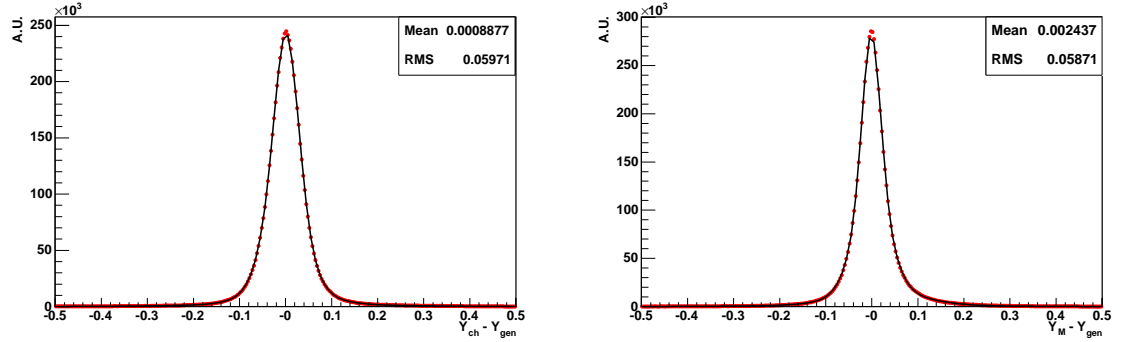


Figure 4.7: MonteCarlo distributions of resolutions: Y_{ch} (left) and Y_M (right). The curves are fitted to a sum of four gaussians.

$$\delta Y_{ch} = 0.025. \quad (4.11)$$

Finally, MonteCarlo studies demonstrate that the best evaluation of Y resolution

is given using the average between the two variables:

$$Y_M = \frac{Y_{ch} + Y}{2}. \quad (4.12)$$

and the corresponding resolution, see fig. 4.7, is:

$$\delta Y_M = 0.019 \quad (4.13)$$

No relevant improvement in the resolution values has been observed imposing the constraint on the invariant mass of π^0 . In the following Y will denote the Y_M variable, while we will refer to the variable obtained using only the photon energies as Y_0 .

Fig.4.8 shows the data-MonteCarlo comparison for the variable $Y_{ch} - Y_0$. Applying a

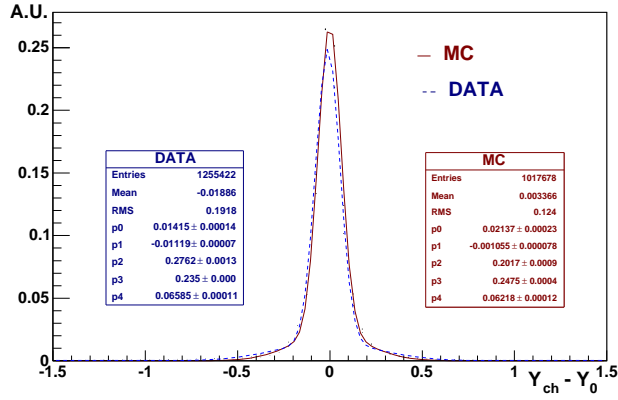


Figure 4.8: Data (continuous line) vs. MonteCarlo (shaded line) comparison for the variable $Y_{ch} - Y_0$. The curves are fitted to a sum of two Gaussians with the same mean. The shift of ~ 1.33 MeV is estimated from the difference between the mean value of the two fitting functions.

double-Gaussian fit with the same mean value, a shift of ~ 1.33 MeV is estimated. This is due to a wrong evaluation of invariant mass of three pions system ($\pi^+ \pi^- \pi^0$) which value on data (see fig. 4.9), in agreement with PDG [65]:

$$M_\eta = 547.75 \pm 0.12^{stat} MeV \quad (4.14)$$

is different with respect to the one on MonteCarlo simulation, $M_\eta = 547.30$ MeV. The data-MonteCarlo discrepancy on the M_η value cannot be considered as an energy

scale effect because for the same events no shift in the peak value of the $\gamma\gamma$ invariant mass is observed, see fig. 4.10.

As expected, correcting on data the M_η value the $Y_{ch} - Y_0$ shift is reduced to the

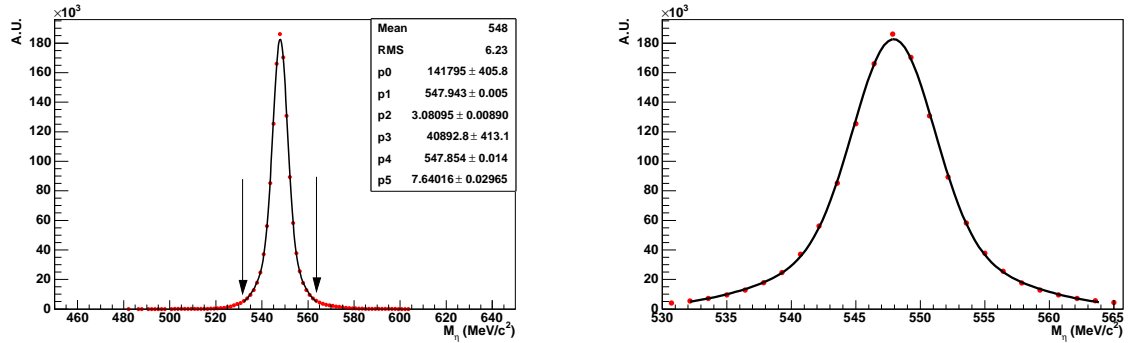


Figure 4.9: Distribution of the invariant mass of three pions system ($\pi^+ \pi^- \pi^0$) for the data sample used in this analysis. The arrows show the range of fit. Right: A zoom of the region of the fit.

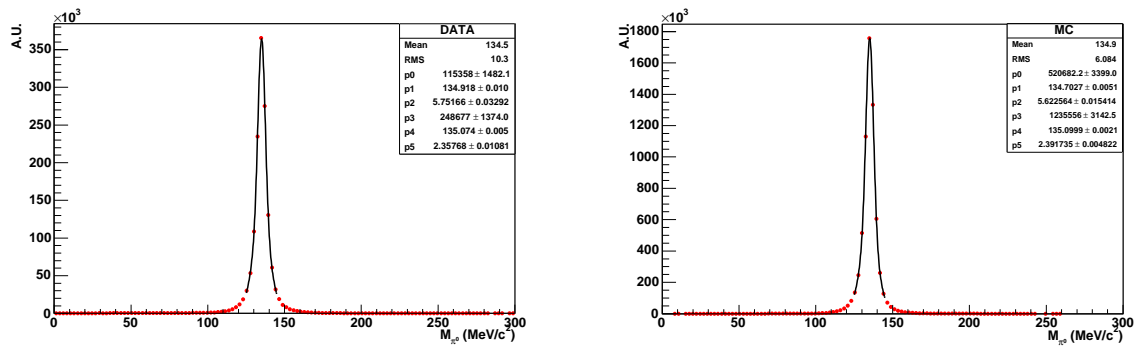


Figure 4.10: The invariant mass of the two softest photons in $\pi^+ \pi^- \gamma\gamma$ events. Left: Data distribution. Right: MonteCarlo distribution.

value ~ 0.03 MeV (fig. 4.11). Finally, in order to improve the agreement between data and MonteCarlo we add to the selection procedure the cut:

$$|Y_{ch} - Y_0| < 0.5. \quad (4.15)$$

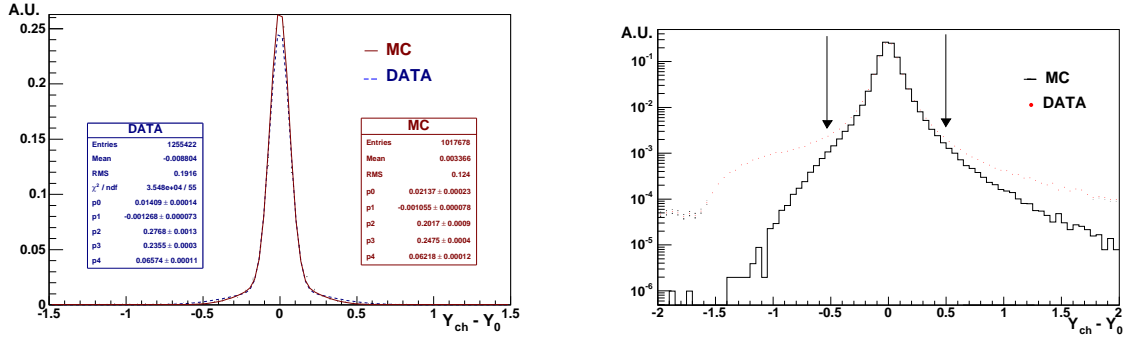


Figure 4.11: Data (continuous line) vs. MonteCarlo (shaded line) comparison for the variable $Y_{ch} - Y$ with the corrected value of M_{η} . Left: linear scale. Right: log scale. The shift of ~ 0.03 MeV is estimated from the difference between the mean value of the two fitting functions. The arrows show the position of the cut eq: (4.15)

This cut is almost fully efficient on signal. The final selection efficiency is $\varepsilon = (34.46 \pm 0.01)\%$. In the region characterized by $N_{binx} = N_{biny} \in [7, 20]$, or changing the linear dimensions of bins from $\Delta X = \Delta Y = 0.29$ to $\Delta X = \Delta Y = 0.10$, possible smearing effects are evaluated. These effects, being the linear dimensions of the bins used much larger than X and Y resolutions, cfr. eq. 4.8, 4.13, are negligible. In particular, fig. 4.12 shows the smearing matrix for X and Y variables in correspondence of a bin width choice:

$$\Delta X = \Delta Y = 0.13 \quad \text{or} \quad N_{binx} = N_{biny} = 16 \quad (4.16)$$

Along the straight lines:

$$X_{gen} = X_{rec} \quad Y_{gen} = Y_{rec} \quad (4.17)$$

there are distributed respectively $\sim 84\%$ and $\sim 76\%$ of events while the rest of events crosses from a bin to the adjacent ones.

The efficiency as function of Dalitz plot point $\varepsilon(X, Y)$ is defined, for each (X, Y) bin, as the ratio between the number of events generated that are fully reconstructed and selected, or equivalently as the plot obtained with the bin-by-bin division

$$\varepsilon(X, Y) = \frac{N_{rec}(X, Y)}{N_{gen}(X, Y)} \quad (4.18)$$

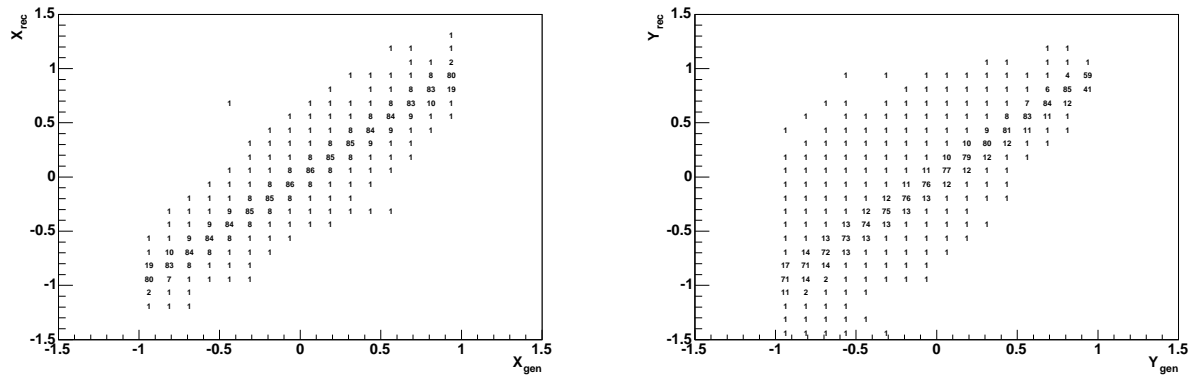


Figure 4.12: Smearing matrix distribution. Left: X variable; Right: Y variable.

where $N_{rec}(X, Y)$ is the reconstructed Dalitz distribution and $N_{gen}(X, Y)$ is the originally MonteCarlo generated Dalitz distribution. In fact it must be stressed that the definition of efficiency given above actually contains also the smearing effects integrated bin by bin over the MonteCarlo histogram. This approach is equivalent to the use of the complete four-dimensional smearing matrix as long as the parametrization of the Dalitz plot shape used in the simulation is in good agreement with the real one. As described later in this thesis, we have used a low statistics data sample to obtain a first estimate of the parameters in order to better the MonteCarlo description and then we have used the improved MonteCarlo for determining the final result on the full statistics. The $\varepsilon(X, Y)$ (see fig. 4.13) is almost flat in the central region of Dalitz-plot but presents few peaks on contour because in the corresponding bins the phase space is reduced and the contribution of nearby bins via the smearing effects is percentually larger. The projections of $\varepsilon(X, Y)$ on the X and Y axis are plotted in fig. 4.14. While the efficiency appears to behave quite independently of X and preserve the symmetry property, it decreases in an approximately linear way as Y grows in the allowed interval. This can be explained through simple arguments. The X variable is proportional to a difference between kinetic energies of π^+ and π^- which behave similarly in the Drift Chamber and since we don't ask the track to cluster association we expect no asymmetry in the efficiency, apart from the one coming from possible residual magnetic field effects. In the average, a large value for Y means a

low-momentum π^\pm in the decay: this reduce the probability to correctly reconstruct the vertex and explains the slight drop in efficiency as Y rises.

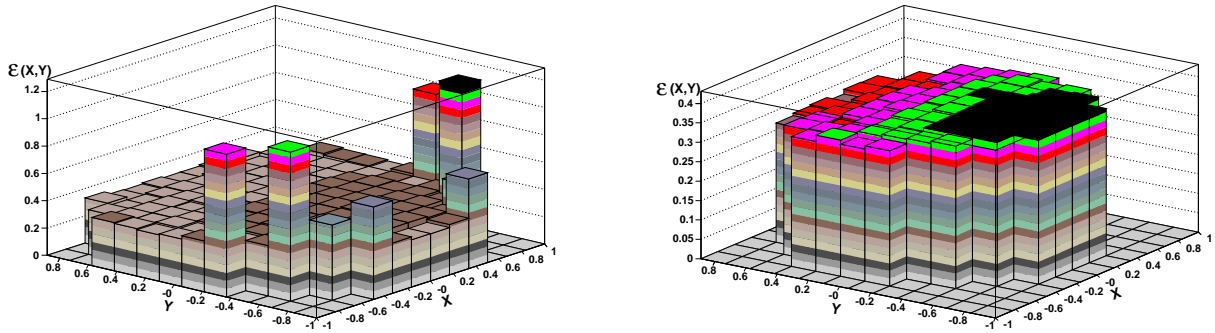


Figure 4.13: Efficiency as function of Dalitz-plot, before (left) and after (right) removing the bins crossed by Dalitz-plot contour.

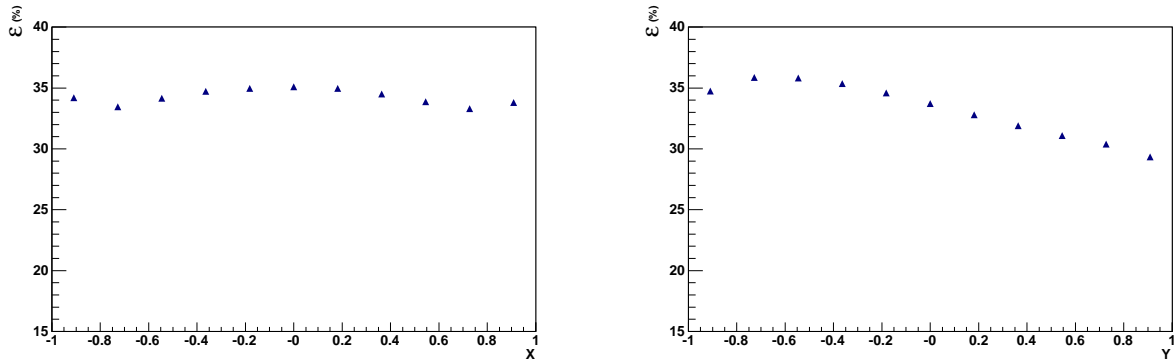


Figure 4.14: Left: Efficiency versus X . Right: Efficiency versus Y .

4.4 Fit of Dalitz-plot procedure

The fit is done using a least squares approach. Let $|A(X, Y)|^2$ the theoretical function

$$|A(X, Y)|^2 \simeq N(1 + aY + bY^2 + cX + dX^2 + eXY). \quad (4.19)$$

and N_{ij} the number of events in the bidimensional bin (i, j) , the χ^2 is:

$$\chi^2 = \sum_{i=1}^{N_{binx}} \sum_{j=1}^{N_{binx}} \left(\frac{\frac{N_{ij}}{\varepsilon_{ij}} - \int_{x_i^{min}}^{x_i^{max}} \int_{y_i^{min}}^{y_i^{max}} |A(X, Y)|^2 dPh^4(X, Y)}{\sigma_{ij}} \right)^2 \quad (4.20)$$

where for each bin (i, j) :

- ε_{ij} is the efficiency as function of Dalitz-plot,
- (x_i^{min}, x_i^{max}) and (y_j^{min}, y_j^{max}) are the boundary of bins in X and Y ,
- σ_{ij} is the statistical error on the ratio $\frac{N_{ij}}{\varepsilon_{ij}}$, according to:

$$\sigma_{ij} = \frac{N_{ij}}{\varepsilon_{ij}} \sqrt{\frac{1}{N_{ij}} + \left(\frac{(\delta\varepsilon)_{ij}}{\varepsilon_{ij}} \right)^2} \quad (4.21)$$

All the bins are included in the fit apart from the bins crossed by the Dalitz-plot contour, in which fluctuations of efficiency are present.

4.5 Results of fit on MonteCarlo

The procedure of fit described has been tested on MonteCarlo.

In order to exclude possible correlations that can affect the parameters evaluation the efficiency has been calculated on an independent sample. Initially we have analysed a sample of ~ 250000 pure $\phi \rightarrow \eta\gamma$ events, in which the phase space has been generated with these parameter values:

$$a = -1, \quad b = c = d = e = 0. \quad (4.22)$$

Fig. 4.15 shows how the fitted parameter values change with the number of degrees of freedom ⁵, ndf ; at the same time the binning for the Dalitz-plot change from $N_{binx} = N_{biny} = 7$ to $N_{binx} = N_{biny} = 20$, in correspondence the linear dimensions of bins change from $\Delta X = \Delta Y = 0.29$ to $\Delta X = \Delta Y = 0.10$. The choice of not increase further the binning is essentially driven by the resolution of the two variables X, Y (cfr. eq. 4.8, 4.13): smearing effects can negatively affect the agreement between the data and the theoretical function.

As can be observed, the fitting procedure allows to find correctly the MonteCarlo input parameters (in fig. 4.15 pointed out with the straight line) and moreover the measurements are almost ndf independent, to be precise binning independent.

Some parameters are strongly correlated, table 4.1 gives the correlation coefficients between the parameters. In particular b and d are anticorrelated with a , on the other hand c and e are less correlated to the other parameters. Thus we expect that fixing to zero the value of c and e the other ones will not change. In fact, see fig. 4.16, considerable variations are not present.

	a	b	c	d	e
a	1	-0.723	0.011	-0.442	-0.018
b		1	-0.056	0.311	0.053
c			1	0.052	-0.389
d				1	-0.065
e					1

Table 4.1: Correlation matrix from the Dalitz-plot fit.

⁵ ndf is the difference between the number of effective bins fitted, removing the bins crossed by Dalitz-plot contour, and parameters measured: $ndf = N_{bin}^{eff} - P$.

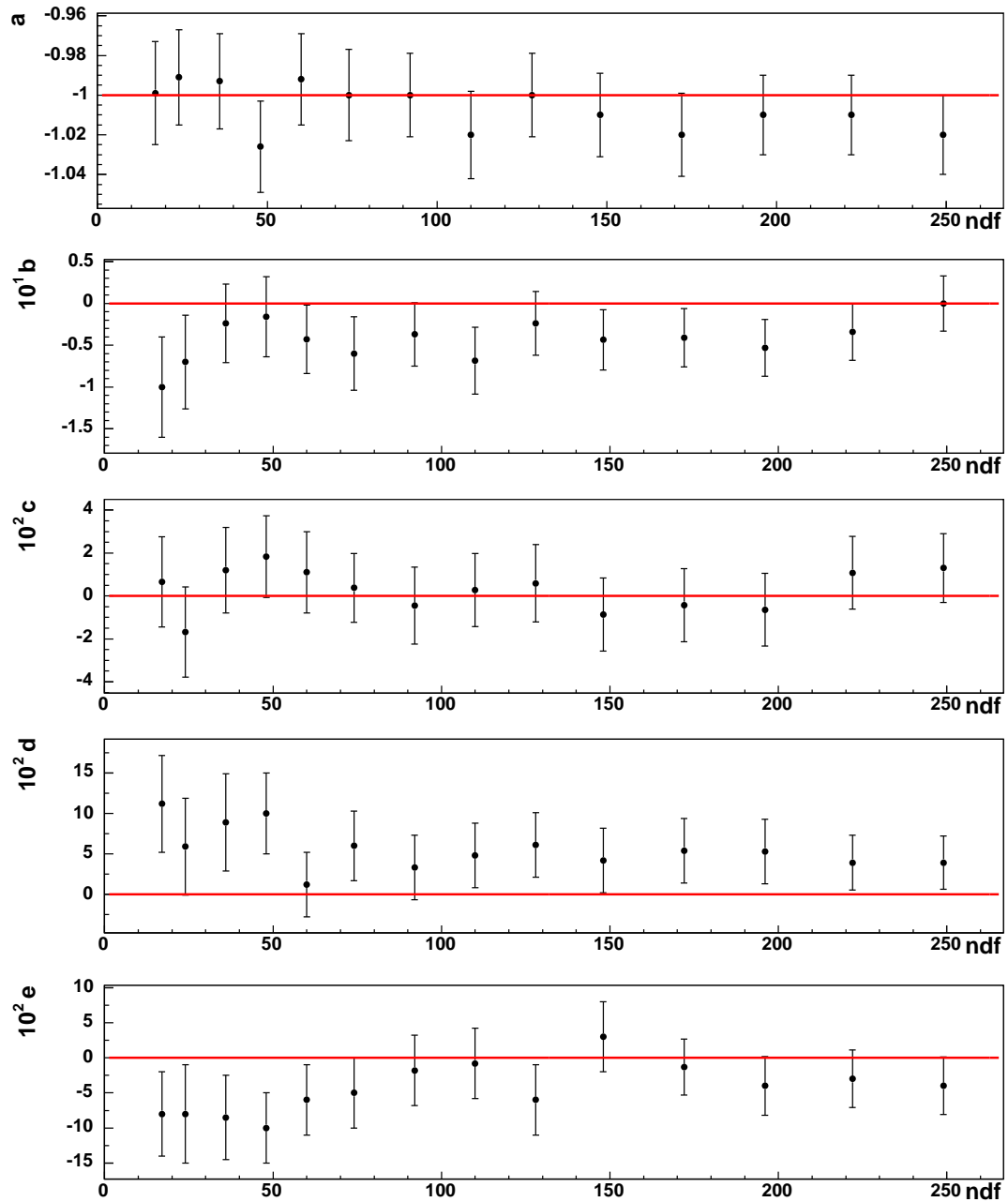


Figure 4.15: Results of the Dalitz-plot fit for different ndf . The results refer to a parametrization for the decay amplitude $|A(X, Y)|^2 \simeq 1 + aY + bY^2 + cX + dX^2 + eXY$. The MonteCarlo input parameters are pointed out with the straight line.

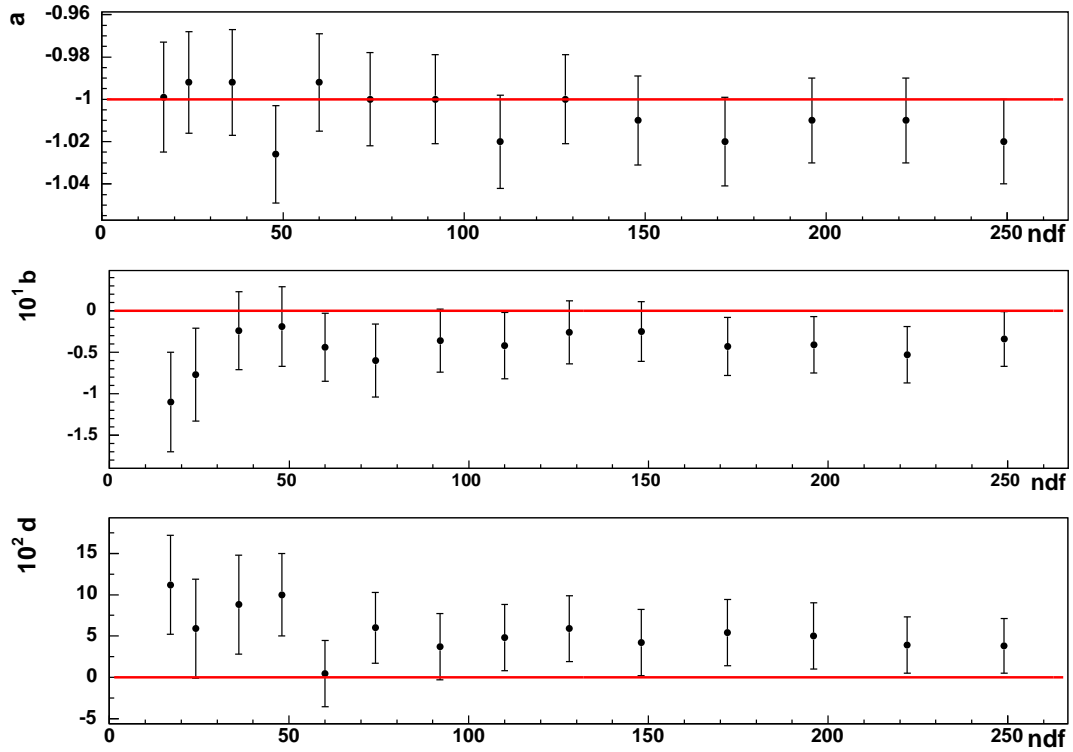


Figure 4.16: Results of the Dalitz-plot fit for different ndf . The results refer to a parametrization for the decay amplitude $|A(X, Y)|^2 \simeq 1 + aY + bY^2 + dX^2$. The fit is performed by setting to zero the parameter values c and e . The MonteCarlo input parameters are pointed out with the straight line.

Chapter 5

Results

In March 2006, the KLOE experiment was successfully concluded and a total integrated luminosity of about 2.5 fb^{-1} has been collected. The entire KLOE data set correspond to more $10^8 \eta$ meson thus the radiative ϕ decays make DAΦNE a clear η -factory.

In this chapter a precise measurement of the “slope parameters” of Dalitz plot density distribution is discussed. The 2001-2002 statistics ($\sim 450 \text{ pb}^{-1}$), corresponding to about 1.3 millions of $\eta \rightarrow \pi^+ \pi^- \pi^0$ events in the Dalitz plot is analyzed, (section 5.1). The various contributions to the systematic uncertainty and the final results are described in sections 5.4 and 5.5, respectively.

5.1 Analysis on data

In order to give a precise measurement of the slope parameters the statistics, $\int L dt = 451 \text{ pb}^{-1}$, collected in 2000 to 2002 data taking is analysed.

The total expected number of $\eta \rightarrow \pi^+ \pi^- \gamma \gamma$ events has been estimated using the visible cross section at ϕ peak [66], and the MC efficiency corrected for the data/MC ratio of efficiencies for low energy photons, and for the data/MC ratio of tracking and vertex efficiencies.

$$\sigma(\eta\gamma)_{\text{visible-peak}} = (40.2 \pm 1) \text{ nb} \quad (5.1)$$

$$N_{\text{exp}} = 1.35 \pm 0.04 \text{ Mevts} \quad (5.2)$$

Whereas, the number of events in the Dalitz-plot, see fig.5.1, is:

$$N_{found} = 1.337 \pm 0.001 \quad \text{Mevts} \quad (5.3)$$

We notice a difference at the level of 1.2%, and the two numbers are compatible within errors. Before analyzing the whole statistics, the procedure of fit has been applied on a data sample corresponding to $\int Ldt \sim 100 \text{ pb}^{-1}$ collected in 2000 and 2001.

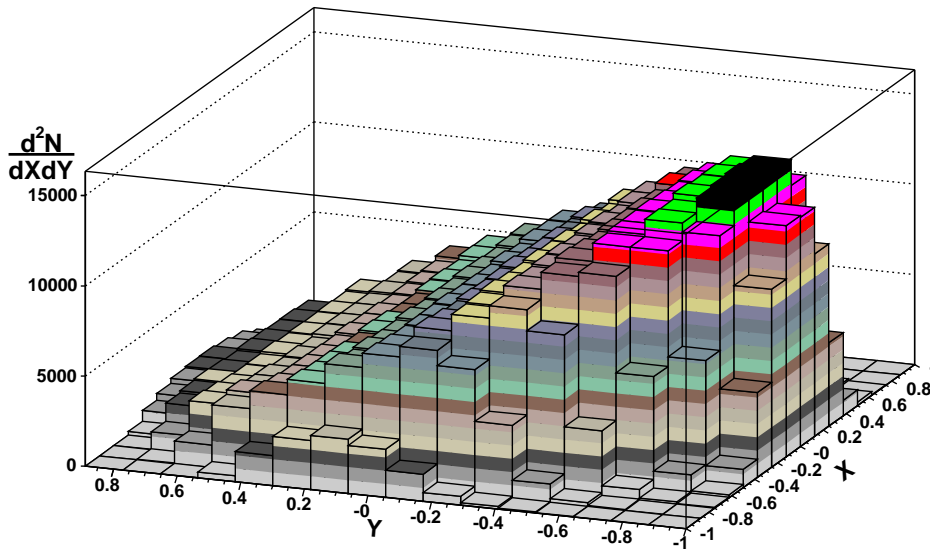


Figure 5.1: Dalitz-plot distribution observed on whole data sample. The plot contains 1.39 millions of events in 256 bins.

5.2 Results of fit on 2000 – 2001 statistics

As made for the MonteCarlo, we have estimated the parameter values for different ndf , see fig.5.2. After an initial instability essentially due to the low ndf available for the fit, the measures catch up a plateau region in which they are almost binning independent.

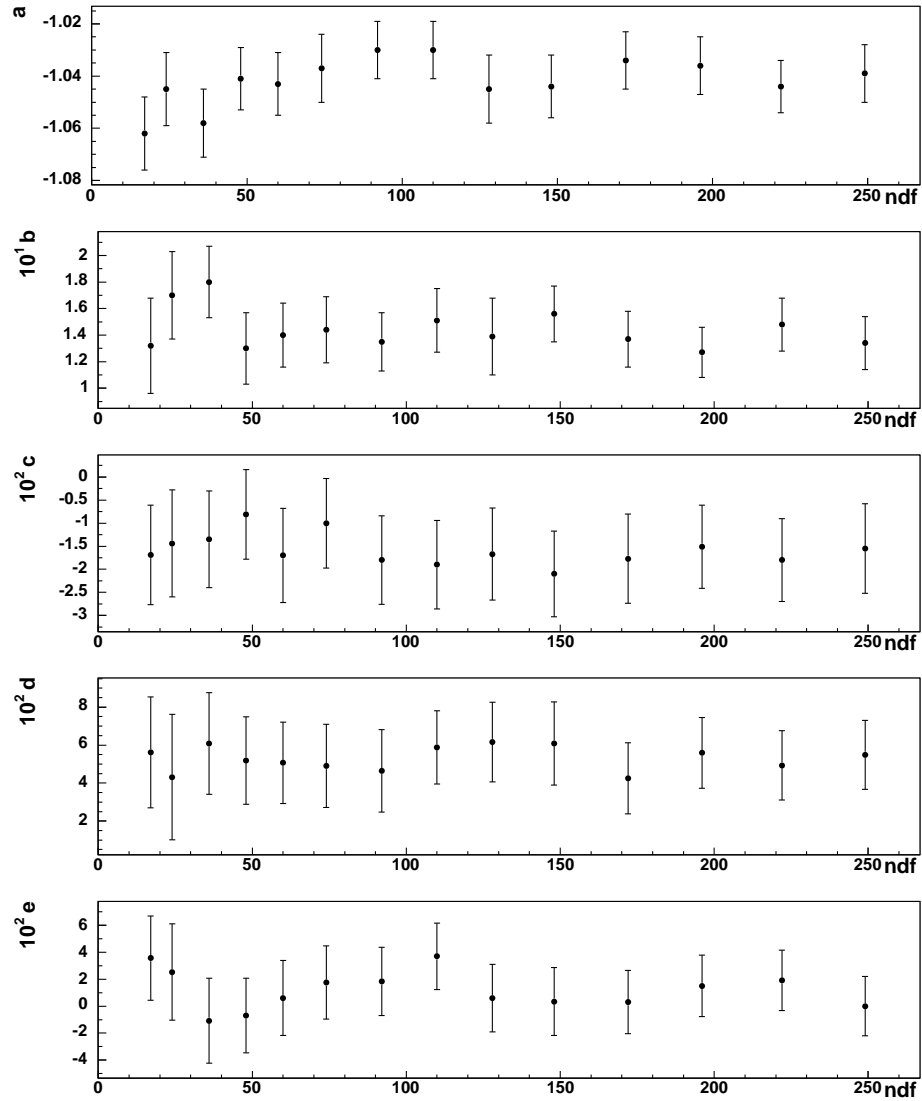


Figure 5.2: Results of the Dalitz-plot fit for different values of ndf . The results refer to a parametrization for the decay amplitude $|A(X, Y)|^2 \simeq 1 + aY + bY^2 + cX + dX^2 + eXY$.

ndf	P_{χ^2}	a	b	c	d	e
74	65%	-1.04 ± 0.01	0.14 ± 0.03	-0.001 ± 0.002	0.05 ± 0.02	-0.02 ± 0.03
76	68%	-1.04 ± 0.01	0.14 ± 0.03		0.06 ± 0.02	
77	52%	-1.03 ± 0.01	0.13 ± 0.02			

Table 5.1: Results of the fit for different parametrizations of $|A|^2$ and for a total of bins $N_{bin}^{eff} = 80$ corresponding to linear dimensions of bins equal to $\Delta X = \Delta Y = 0.17$.

In correspondence of $N_{bin}^{eff} = 80$ (or for linear dimensions of bins equal to $\Delta X = \Delta Y = 0.17$), where we found the better χ^2 probability, we give the final evaluation of the slope parameters, see table 5.1.

The quoted uncertainties on the parameters are those coming from the fit. The parameter values obtained fixing to zero the value of c and e have been inserted in the generator of the new MonteCarlo production used in the rest of this analysis, this allowed us to improve our simulation of the decay, with a more accurate determination efficiencies within each bin. We have checked our ability to reproduce the values inserted into the new improved MonteCarlo simulation.

The results are shown in fig. 5.3. We compare the values obtained in output from the fit with the ones used as input for the Monte Carlo production, and build a χ^2 variable, including the full covariance matrix as estimated by the fit. We get good agreement for each binning choice. In particular e.g. for the binning $N_{eff}^{bin} = 154$, which later we will show being the “best binning choice” on data, one finds a $\chi^2/dof = 3.1/5$ with a χ^2 probability of 68% : this gives us confidence that our fitting procedure does not introduce a bias in the estimation of parameters.

5.3 Results of fit on whole statistics

To fit the Dalitz plot distribution, the efficiency has been estimated using a sample of 18.7 millions of events from the new MonteCarlo production. Among these events $\sim 5\%$ are Initial State Radiation (ISR), in which a photon is emitted by the incoming electron or positron. No discrepancy with the previous measurements is observed when fitting with standard parametrization, see eq: (4.19). With the increased

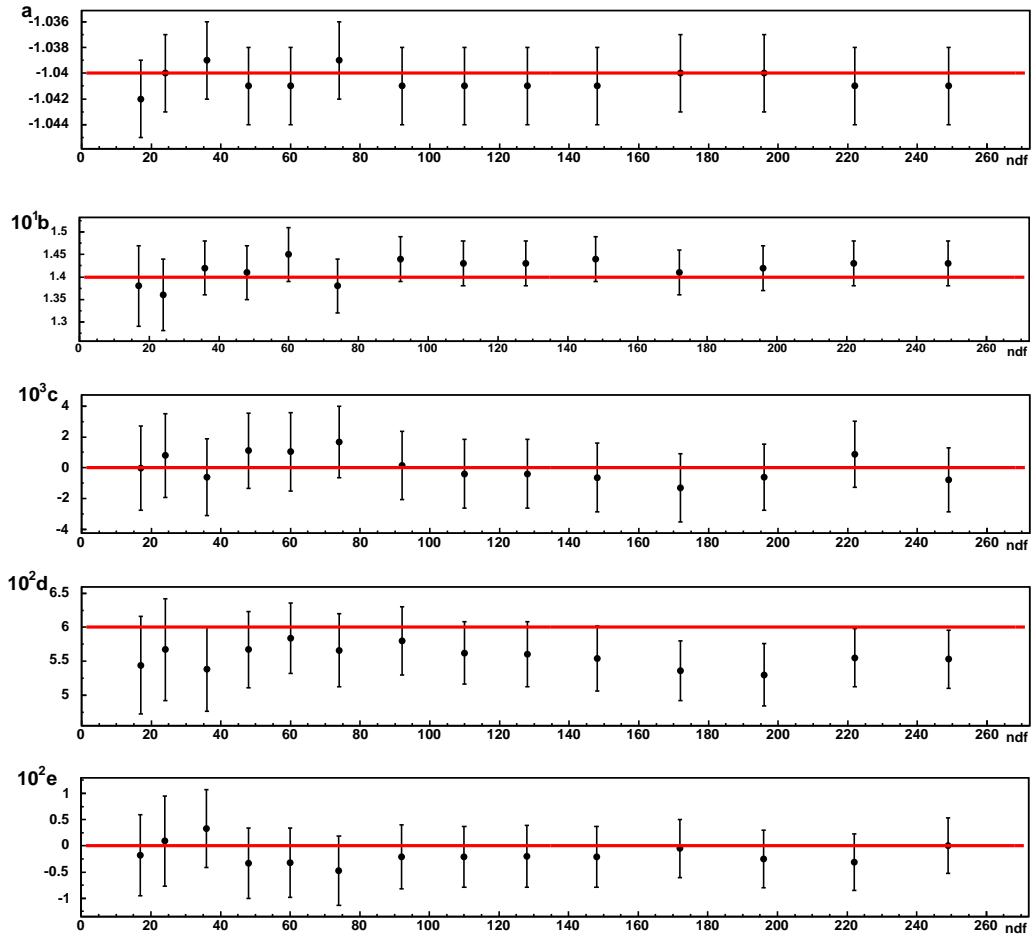


Figure 5.3: Results of the Dalitz-plot fit on the Monte Carlo improved simulation for different values of ndf . The results refer to a parametrization for the decay amplitude $|A(X, Y)|^2 \simeq 1 + aY + bY^2 + cX + dX^2 + eXY$. The horizontal lines show the values used as input for the simulation.

statistics, both data and MC, the theoretical model seems not to fit adequately the data: we found values of χ^2 probability very low, for each ndf . Consequently we have expanded the decay amplitude about the center of the Dalitz plot adding the cubic terms:

$$|A(X, Y)|^2 \simeq 1 + aY + bY^2 + cX + dX^2 + eXY + fY^3 + gX^3 + hX^2Y + lXY^2 \quad (5.4)$$

and we have used this theoretical function to fit the Dalitz plot distribution.

As we expected, for each ndf the values of χ^2 probability improve. Moreover we are sensitive to the cubic slope in Y , never measured before; all the other cubic terms different from f are consistent with zero.

The behaviour of the parameter values is shown in fig 5.4.

Again the parameters' values catch up a plateau region, characterized by $N_{bin}^{eff} \in [54, 202]^1$, in which they are almost binning independent.

The final fit results are reported in table 5.2, in correspondence of $N_{bin}^{eff} = 154$, where we found the better χ^2 probability, and for different parametrizations of $|A|^2$.

Par	$ndf = 147$	$ndf = 149$	$ndf = 150$	$ndf = 150$	$ndf = 151$
a	-1.090 ± 0.005	-1.090 ± 0.005	-1.069 ± 0.005	-1.041 ± 0.003	-1.026 ± 0.003
b	0.124 ± 0.006	0.124 ± 0.006	0.104 ± 0.005	0.145 ± 0.006	0.125 ± 0.006
c	0.002 ± 0.003				
d	0.057 ± 0.006	0.057 ± 0.006		0.050 ± 0.006	
e	-0.006 ± 0.007				
f	0.14 ± 0.01	0.14 ± 0.01	0.13 ± 0.01		
P_{χ^2}	73%	74%	$< 10^{-6}\%$	$< 10^{-8}\%$	$< 10^{-6}\%$

Table 5.2: Results of the fit for different parametrizations of $|A|^2$ and for a total of bins $N_{bin}^{eff} = 154$ corresponding to linear dimensions of bins equal to $\Delta X = \Delta Y = 0.13$.

Looking at values of χ^2 probability, it is evident that is necessary to fit including both d and f parameters. We clearly observe a quadratic slope in X and a cubic slope in Y different from zero. As expected from the C-invariance in the $\eta \rightarrow \pi^+ \pi^- \pi^0$ decay the parameters c and e are consistent with zero, moreover can be removed from the fit without affecting the other parameters. In any case a good stability of the parameter

¹The region $N_{bin}^{eff} \in [54, 202]$ corresponds to linear dimensions of bins changing from $\Delta X = \Delta Y = 0.20$ to $\Delta X = \Delta Y = 0.11$.

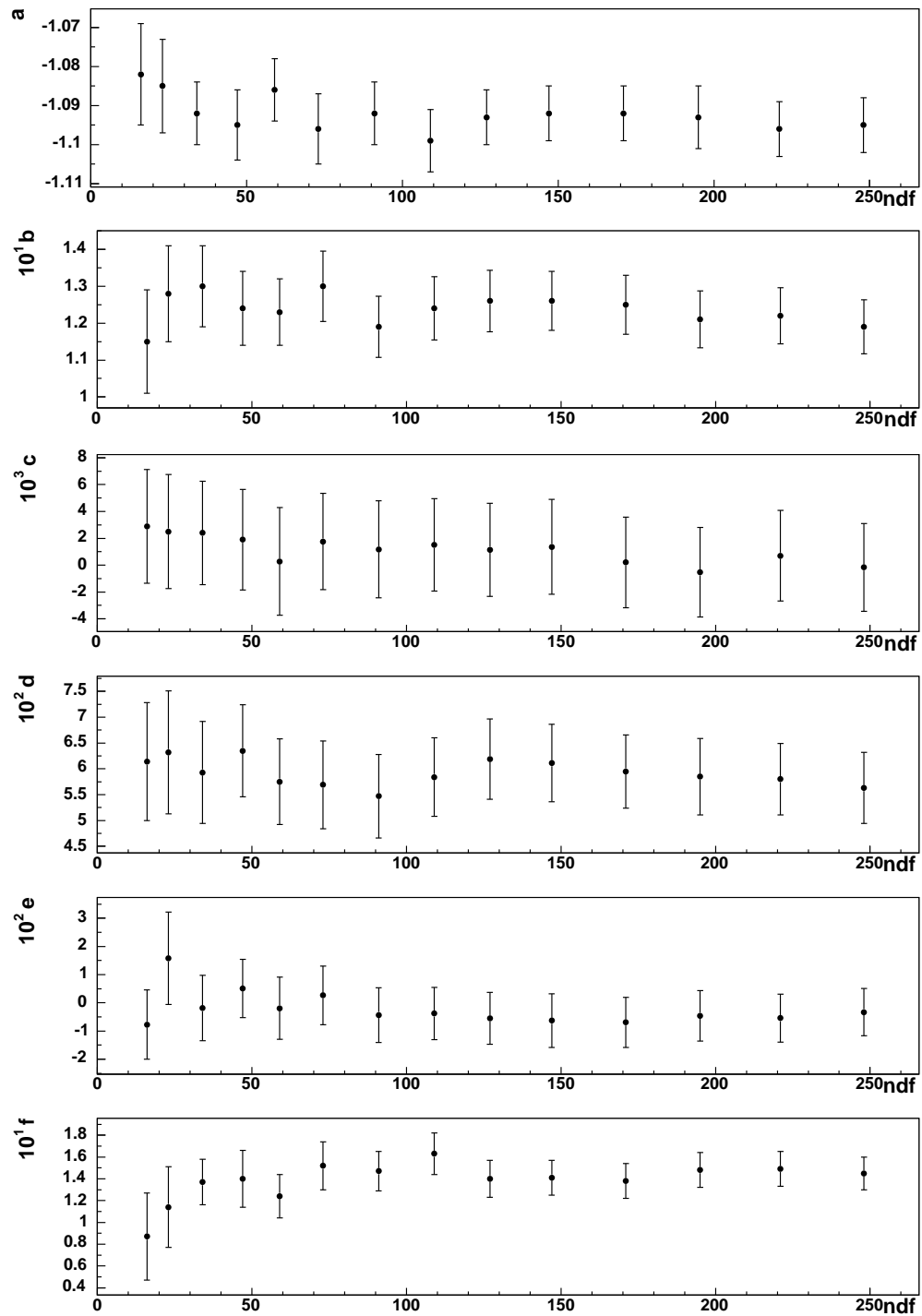


Figure 5.4: Results of the Dalitz-plot fit for different ndf . The results refer to a parametrization for the decay amplitude $|A(X, Y)|^2 \simeq 1 + aY + bY^2 + cX + dX^2 + eXY + fY^3$.

values is observed.

Fig. 5.5 shows a comparison between the efficiency corrected data and the fitted function as a function of the bin number, while in fig.5.6 as a function of the Dalitz plot variables.

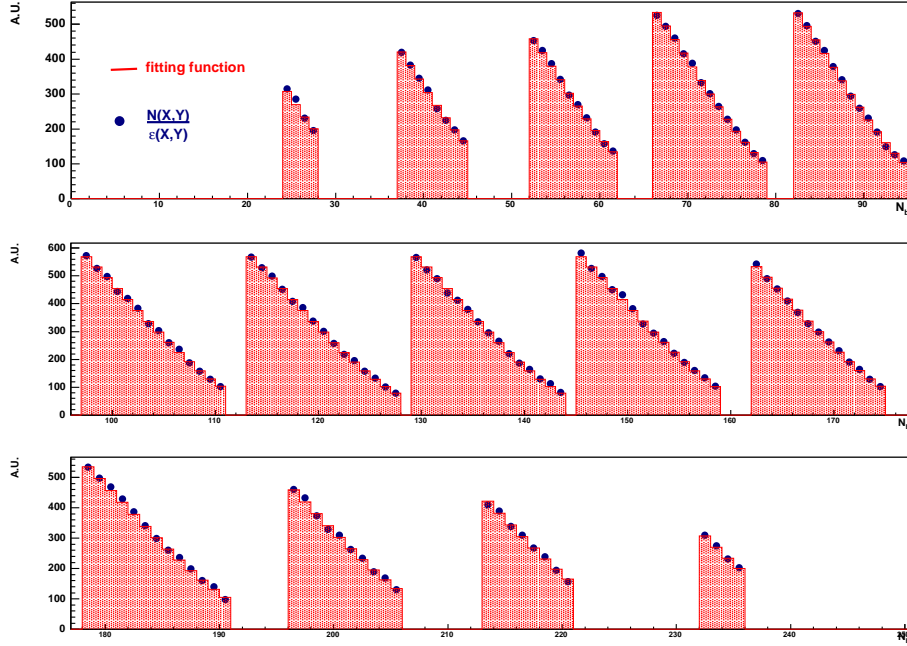


Figure 5.5: In correspondence of $N_{bin}^{eff} = 154$ a comparison between data and fitted function, $|A(X, Y)|^2 \simeq 1 + aY + bY^2 + cX + dX^2 + eXY + fY^3$, as a function of the bin number. The observed structure corresponds to Y distributions corresponding to slices in X . Blue points are data and the histogram is the function.

5.3.1 Check on cubic term 'f'

We have performed some checks to investigate if the sensitivity to the cubic slope in Y on data is a possible effect of efficiency.

Neglecting resolution effects (cfr. fig.4.12) the fitted function is actually the following:

$$\frac{1}{\varepsilon^{MC}(X, Y)} \frac{dN(X, Y)}{dXdY} \Big|_{fit} = \frac{\varepsilon^{REAL}(X, Y)}{\varepsilon^{MC}(X, Y)} \cdot |A(X, Y)|^2 \quad (5.5)$$

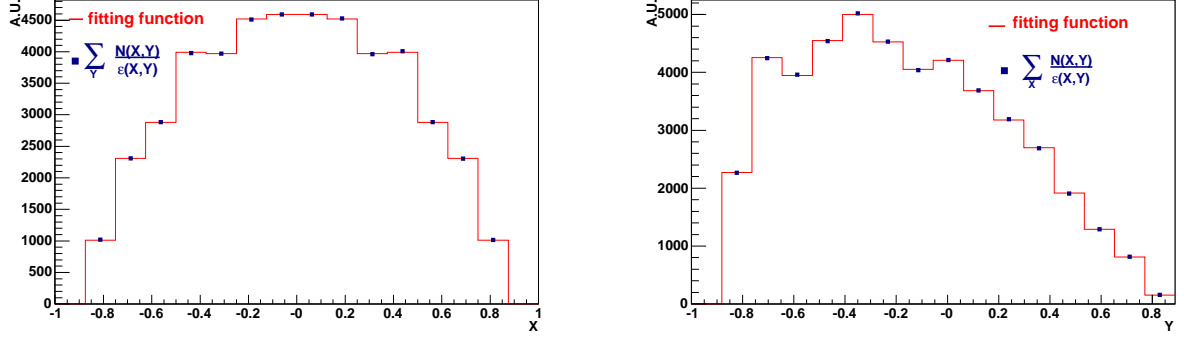


Figure 5.6: In correspondence of $N_{bin}^{eff} = 154$ a comparison between data and fitted function, $|A(X, Y)|^2 \simeq 1 + aY + bY^2 + cX + dX^2 + eXY + fY^3$, as a function of Dalitz plot variables. Left: X variable. Right: Y variable. Blue points are data and the histogram is the function.

If we assume the cubic term is actually a fake induced by our fitting procedure, the true expansion for $|A(X, Y)|^2$ is:

$$|A(X, Y)|^2 \simeq 1 + aY + bY^2 + dX^2. \quad (5.6)$$

in which we have neglected the cubic dependency in Y and the odd powers² of X .

Now, from the fit we obtain:

$$\frac{1}{\varepsilon^{MC}(X, Y)} \frac{dN(X, Y)}{dXdY}_{fit} \simeq 1 + a'Y + b'Y^2 + d'X^2 + f'Y^3 \quad (5.7)$$

we can thus define:

$$R(X, Y) \equiv \frac{\varepsilon^{REAL}(X, Y)}{\varepsilon^{MC}(X, Y)} = \frac{1 + a'Y + b'Y^2 + d'X^2 + f'Y^3}{1 + aY + bY^2 + dX^2}. \quad (5.8)$$

The ratio of the “real” efficiency to the MC one is of course a function of the Dalitz variables X and Y , which in case of perfect MC description should be just a constant equal to 1. We can assume that this function may be expanded itself in powers of X and Y around 1, and we have considered two different cases:

1. $R(X, Y) = 1 + \alpha Y + \beta X^2$.

From the eq. 5.8, equating the coefficients of the same order up to third order

²As seen, cfr. tab.5.2, the odd power of X are null.

one has this equation system:

$$\begin{cases} a' = a + \alpha; \\ b' = b + a\alpha; \\ d' = d + \beta; \\ f' = \alpha b; \\ \beta a + \alpha d = 0. \end{cases} \quad (5.9)$$

Resolving the system in the reasonable hypothesis $\alpha < a$, (since we know that a is of order 1) we found:

$$\alpha = 0.3, \quad \beta = 0.01. \quad (5.10)$$

Using these values to reweight the efficiency on MonteCarlo we can compare if the data - MC agreement is improved by this efficiency correction.

Fig.5.7 shows the data MonteCarlo discrepancy bin by bin normalized, with efficiency weighed and no. The disagreement observed tells us that the cubic term cannot be accounted for an efficiency correction of the type discussed above.

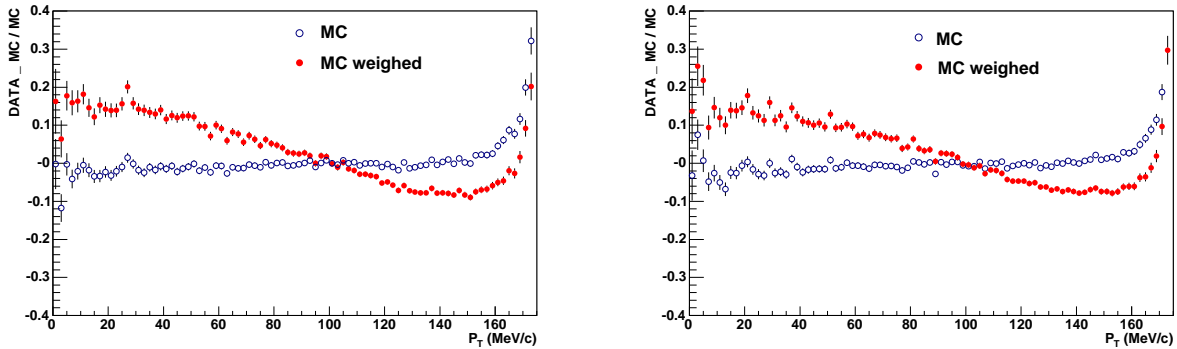


Figure 5.7: Data vs. MonteCarlo discrepancy bin by bin normalized as function of P_T . With full circles (open circles) efficiency weighed using parameters from eq. 5.10 (not weighed). Left: π^+ tracks. Right: π^- tracks.

$$2. R(X, Y) = 1 + \gamma Y^2.$$

In the efficiency we assume to neglect the linear dependency from Y . As described above we resolve the equation system:

$$\begin{cases} a' = a; \\ b' = b + \gamma; \\ d' = d; \\ f' = \gamma a; \end{cases} \quad (5.11)$$

From the fit we obtain for f' and a' respectively a positive and negative value, consequently γ can only assume negative values. We reweight the efficiency using the found value $\gamma = -0.14$. Again, the comparison between MonteCarlo weighed and unweighed, see fig. 5.8, confirm the our sensitivity to the cubic slope in Y on data.

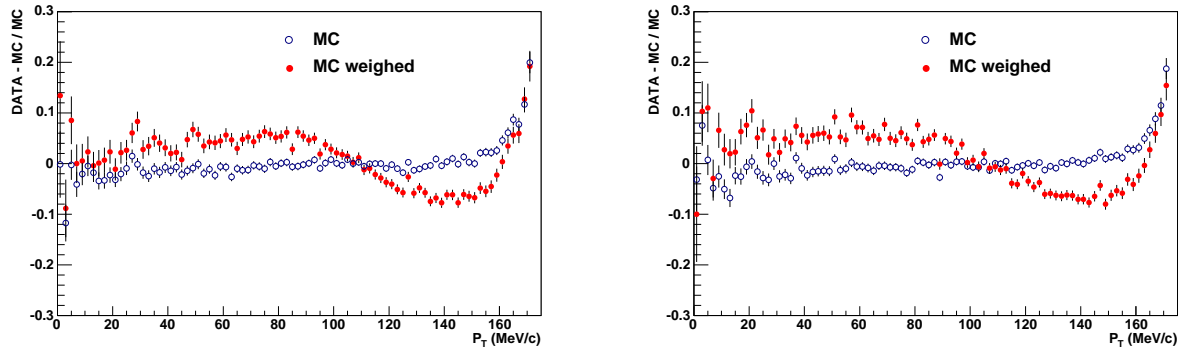


Figure 5.8: Data vs. MonteCarlo discrepancy bin by bin normalized as function of P_T . With full circles (open circles) efficiency weighed using parameter γ (not weighed). Left: π^+ tracks. Right: π^- tracks.

5.4 Systematic uncertainties

We have grouped the sources of sistematics on the parameter estimations in:

- resolution and binning
- efficiency evaluation
- background contamination
- effect of EVCL procedure
- stability with respect to data taking conditions

Finally the possible effects of the presence of radiated photons, i.e., radiative corrections, have been considered.

We measured the sistematics in each of these cases and the final results are summarized in table 5.3.

Source	Δa	Δb	Δd	Δf
BKG	-0.001 +0.006	-0.008 +0.006	-0.007 +0.007	-0.01
BIN	-0.008 +0.006	-0.006 +0.006	-0.007 +0.001	-0.02 +0.02
EVCL	-0.017	0.005	-0.012	0.01

Table 5.3: For each of the fit parameters a summary of the systematic errors.

5.4.1 Resolution and binning

The $\eta \rightarrow \pi^+ \pi^- \pi^0$ events selected as described in the previous section are used to study the energy response and resolution of the calorimeter. We therefore have defined:

$$\frac{\Delta E}{E} = \frac{E_{cl,i}^\gamma - E_{true,i}^\gamma}{E_{true,i}^\gamma} \quad (5.12)$$

where for i^{th} photon, E_{true}^γ is the energy in the output of kinematic fit and E_{cl}^γ is the energy measured by calorimeter and we have analyzed its distribution as function

of E_{true}^γ . In particular, we have analysed the distribution of $\frac{\Delta E}{E}$ as function of E_{true}^γ dividing the spectrum in bins of 20 MeV. The mean value and the sigma obtained from a gaussian fit are plotted in fig. 5.9 both for data and MonteCarlo. The dependence

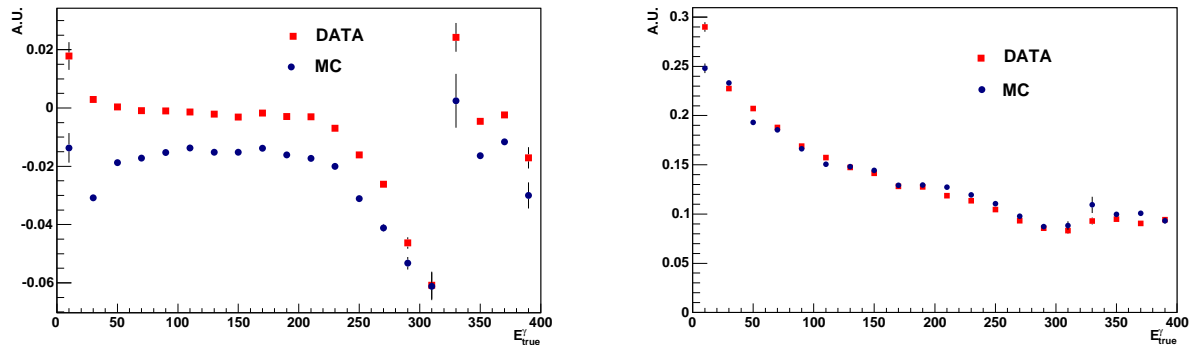


Figure 5.9: Left: distribution of the mean of the gaussian fit to $\frac{\Delta E}{E}$ as a function of E_{true}^γ . Right: distribution of the sigma of the gaussian fit to $\frac{\Delta E}{E}$ as a function of E_{true}^γ

of the mean value of $\frac{\Delta E}{E}$ on E_{true}^γ is weak for both data and MonteCarlo. In data, the photon energy tends to be slightly overestimated, while in MonteCarlo, the photon energy tends to be slightly underestimated; in either case, a drop in response of about 1.5% is observed.

This miscalibration decrease to increasing of the energy. The jitters in the distribution of $\langle \frac{\Delta E}{E} \rangle$ are essentially due to the shape of the photon energy spectrum.

Indeed, since the resolution function is almost symmetric around zero, we expect that in the region where the number of events is increasing as function of E_γ , we get an average correction $\Delta E > 0$, while the opposite applies to region where $N(E_\gamma)$ is decreasing.

This is just related to the fact that the fraction of events in a bin i for which energy has been underestimated (overestimated) is roughly proportional to the number of events in bin $i + 1$ ($i - 1$).

A reasonable agreement is observed on resolution, see also fig.5.10 in which the RMS in bins of E_{true}^γ is plotted. For this reason no attempt to fold the theoretical function with a resolution or smearing matrix has been done, moreover the linear dimensions of bin chosen to give the final evaluation for the slope parameters ($\Delta X = \Delta Y = 0.13$)

are much larger than the X and Y resolutions ($\delta X = 0.020, \delta Y = 0.019$).

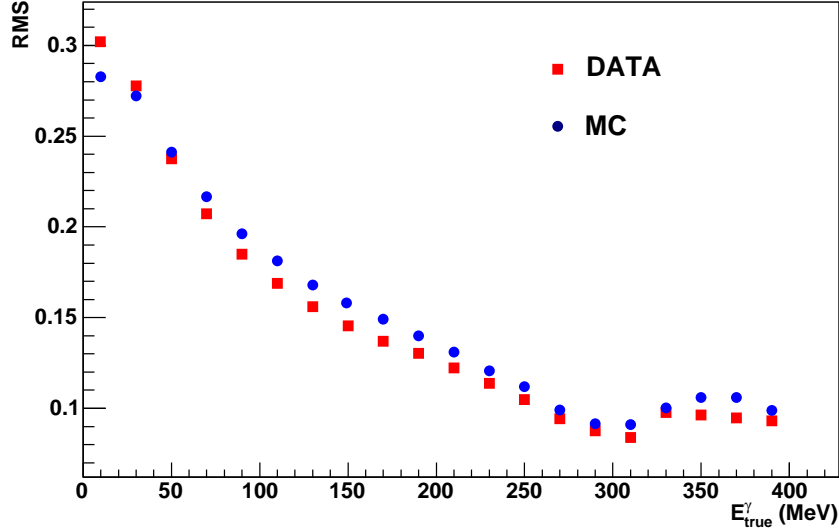


Figure 5.10: Distribution of the rms in bins of E_{true}^{γ} .

The systematic effect associated to this choice has been evaluated considering for each of the parameter values the maximum and minimum spread in the plateau region (cfr. fig.5.4) characterized from $N_{bin}^{eff} \in [54, 202]$. A summary of the results is shown in tab.5.4.

a	b	c	d	e	f
-0.008 +0.006	-0.006 +0.006	-0.001 +0.0	-0.007 +0.001	-0.002 +0.008	-0.02 +0.02
-0.008 +0.006	-0.006 +0.006		-0.007 +0.001		-0.02 +0.02

Table 5.4: For each of the fit parameters the maximum and minimum spread in the region $N_{bin}^{eff} \in [54, 202]$ or $\Delta X = \Delta Y \in [0.20, 0.11]$ is reported.

5.4.2 Efficiency evaluation

Since only the shape of the efficiency is relevant for this analysis a reliability check of the MonteCarlo simulation in reproducing the profile of the efficiency has been performed. Anyway, as stated before, the agreement between the observed and the expected overall number of events is within 1.2% (and within errors).

Figs. 5.11 and 5.12 show a data vs. MonteCarlo comparison of P_T , P_Z , $\cos\theta$ distributions for tracks, minimum P_T and minimum P_Z among the two charged pions and E_γ for photons.

Note that we have used the shift ~ 500 KeV, associated to the different value of the η mass in the MonteCarlo simulation respect to the data (cfr. fig.4.9), to correct the MonteCarlo P_T distributions.

All the variables used in the comparisons are evaluated in the η rest frame. Some discrepancies in the tails of P_T and P_Z distributions are observed. Cutting on the sidebands of these distributions no significant change in the parameter values has been observed. For the same variables a data MonteCarlo ratio has been evaluated, see figs. 5.13, 5.14 and 5.15.

It is evident a slight slope in P_Z distributions. This slope has been used in correcting the MonteCarlo efficiency, resulting in a negligible effect on the final results.

We use as an estimate of the systematic error the observed discrepancy: $\Delta\epsilon = 0.03\%$. A correction to low energy photon efficiency is applied weighting the MonteCarlo events. For the photon efficiency we have used a Fermi-Dirac function obtained fitting the photon energy Data-MC discrepancy, see fig. 5.15. For X and Y variables the ratio between the efficiency weighed and no is shown in fig. 5.16. There is an effect at level of per mill but this is negligible for the parameters evaluation.

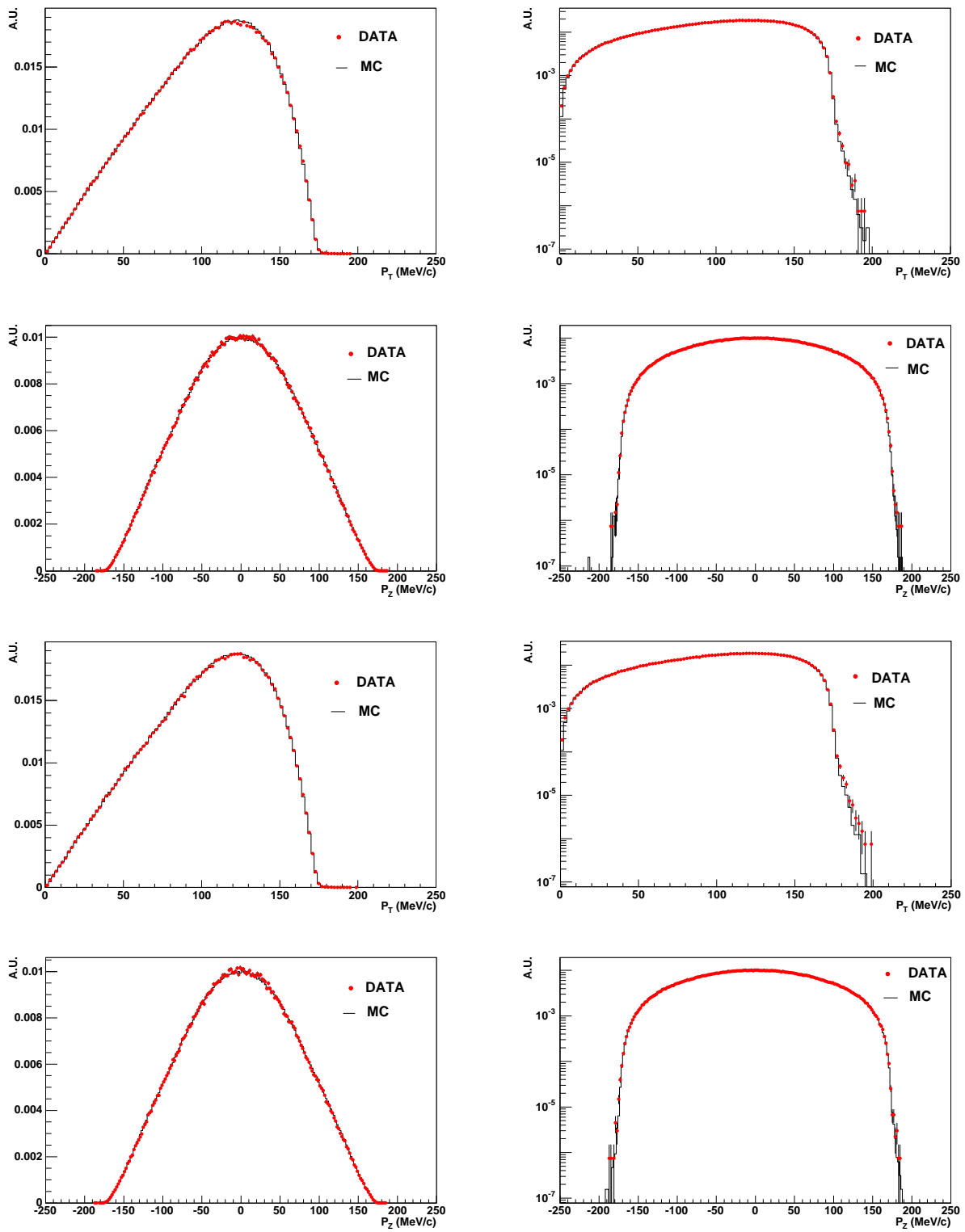


Figure 5.11: Data vs MonteCarlo comparisons. From top to bottom: P_T , P_Z for π^+ and P_T , P_Z for π^- . Left: linear scale. Right: log scale.

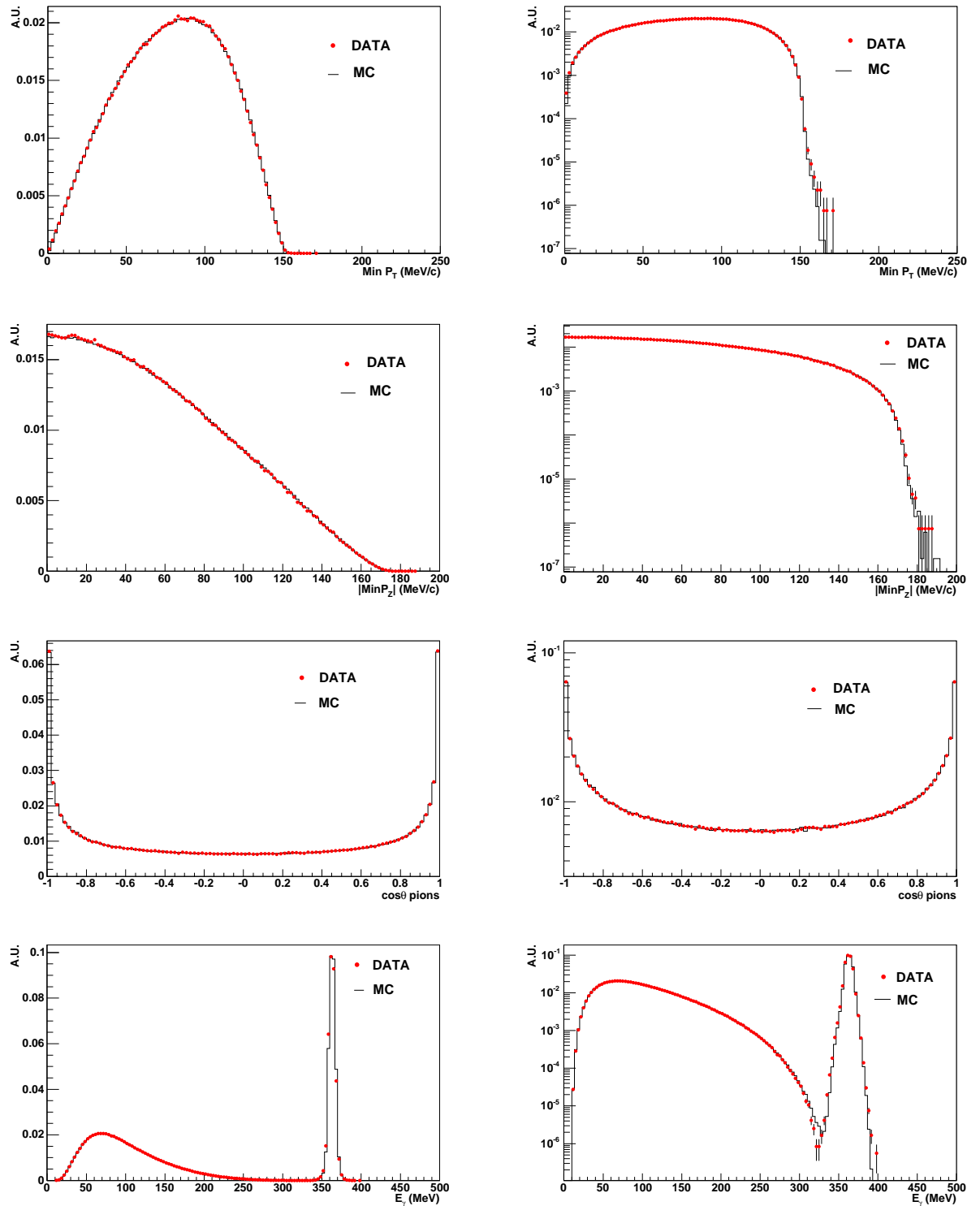


Figure 5.12: Data vs MonteCarlo comparisons. From top to bottom: minimum P_T and P_Z , $\cos \theta$ between pion tracks and E_γ for photons. Left: linear scale. Right: log scale.

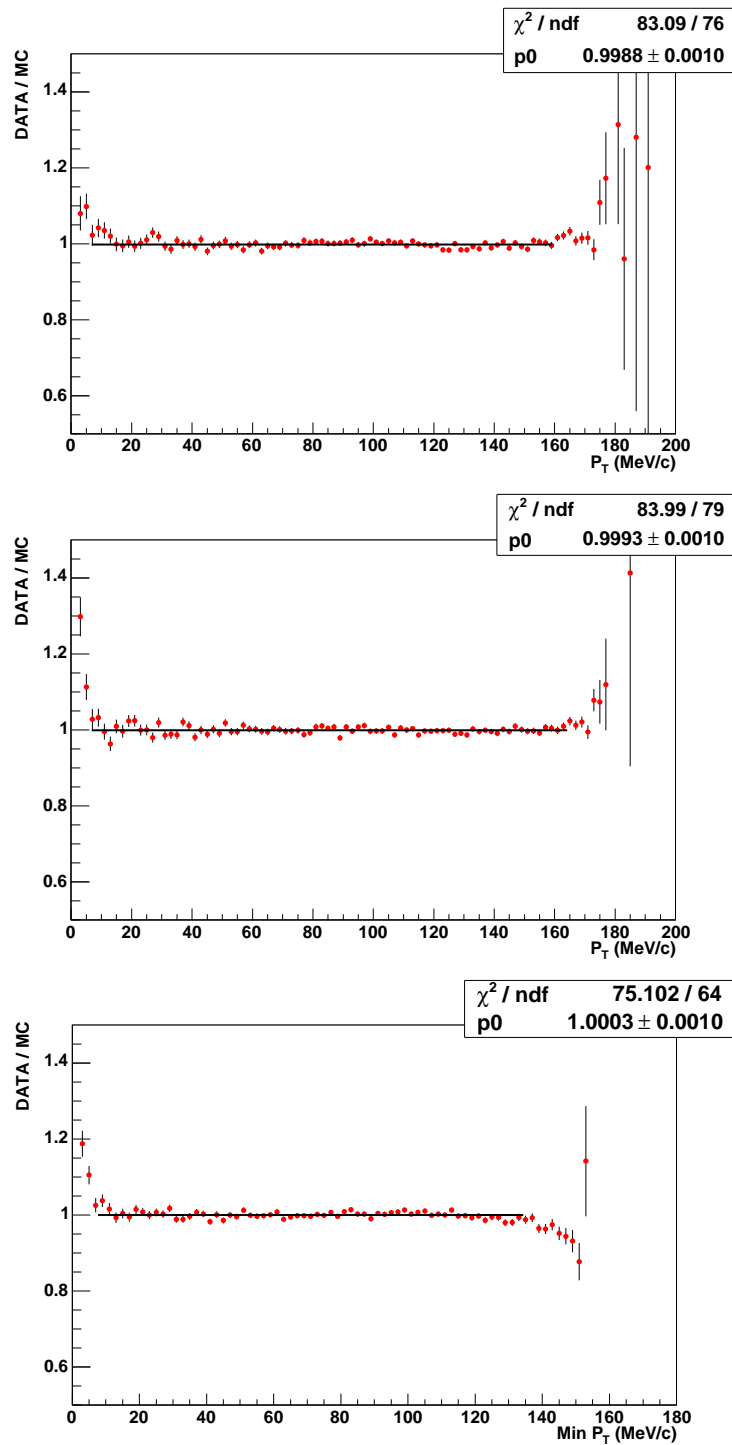


Figure 5.13: Bin by bin normalized Data-MC discrepancy. The MonteCarlo histograms are normalized to the same number of events of the data sample. From top to bottom: P_T , for π^+ and π^- , minimum P_T .

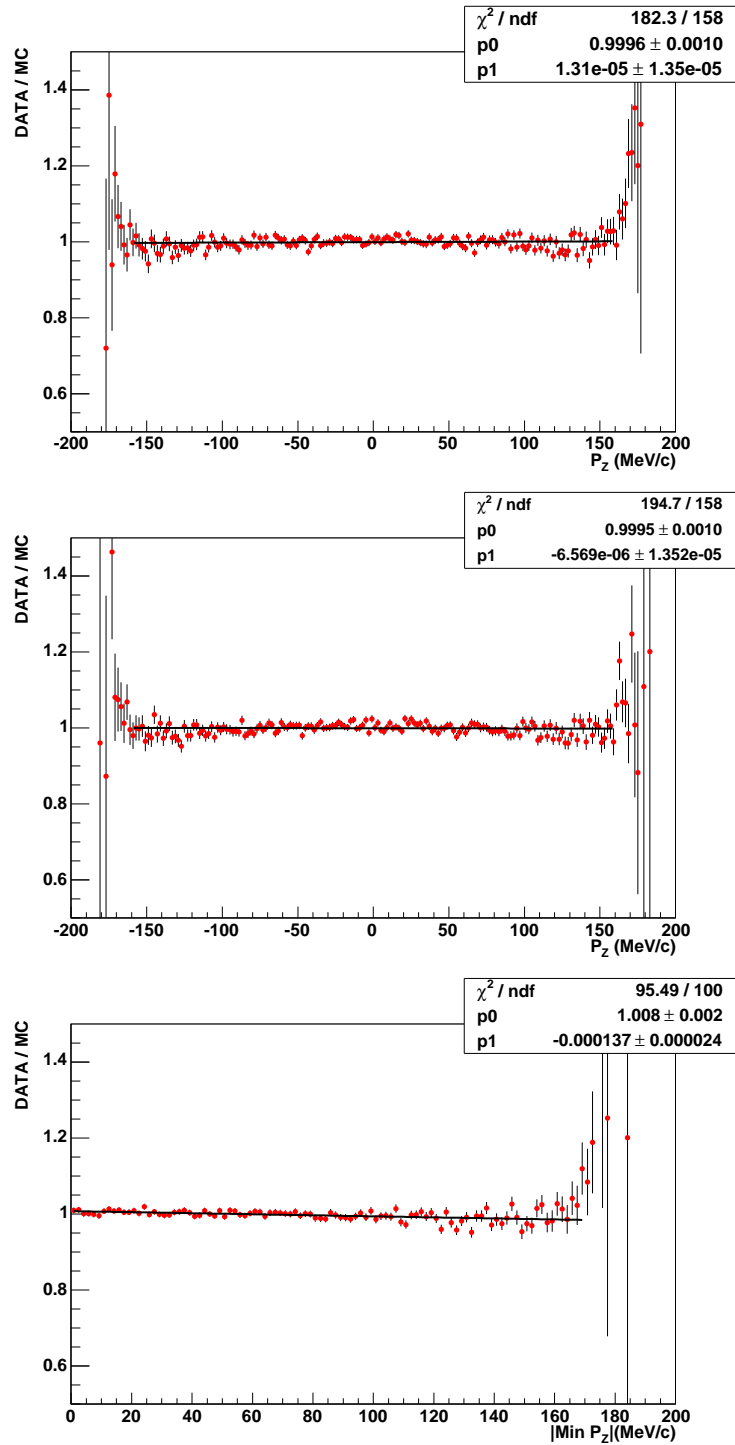


Figure 5.14: Bin by bin normalized DATA-MC discrepancy. The MonteCarlo histograms are normalized to the same number of events of the data sample. From top to bottom: P_z for π^+ and π^- , $|\text{minimum } P_z|$.

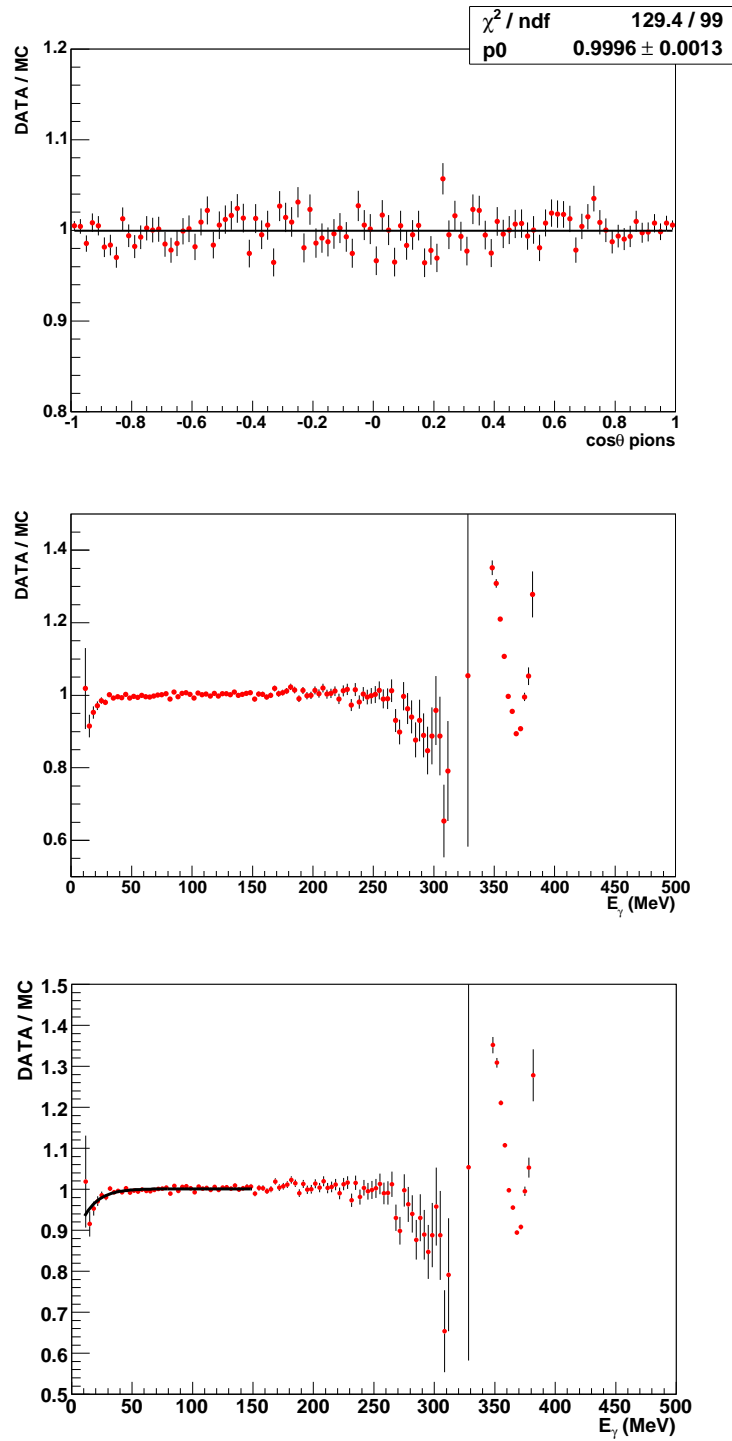


Figure 5.15: Bin by bin normalized Data-MC discrepancy. The MonteCarlo histograms are normalized to the same number of events in the data sample. From top to bottom: $\cos\theta$ between pion tracks, E_γ for photons and E_γ for photons with the fit to the Fermi-Dirac function superimposed.

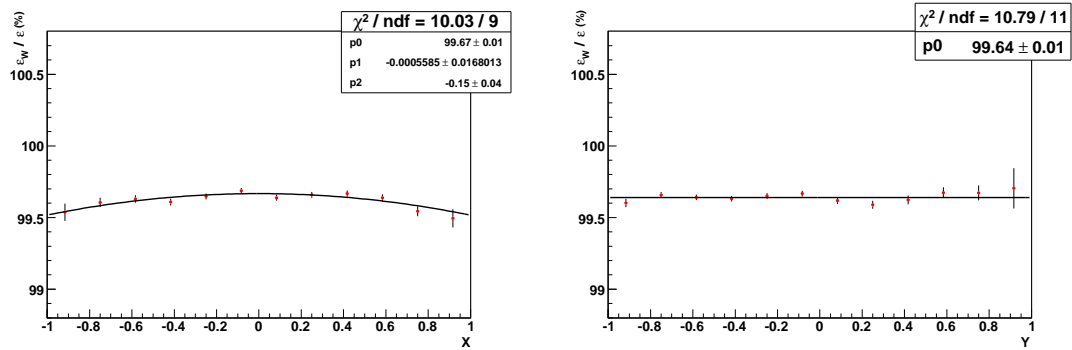


Figure 5.16: Ratio between weighed and not weighed efficiencies as function of X (Left) and Y (Right). The errors take into account the correlations between the efficiencies.

5.4.3 Background contamination

In order to evaluate the systematic error due to background evaluation we have used the official MonteCarlo "ALL PHYS" production. The data-MonteCarlo comparison for the Y variable (see fig.5.17) evidences the presence of background. In particular, the background-signal ratio estimated by MonteCarlo is $\sim 0.3\%$.

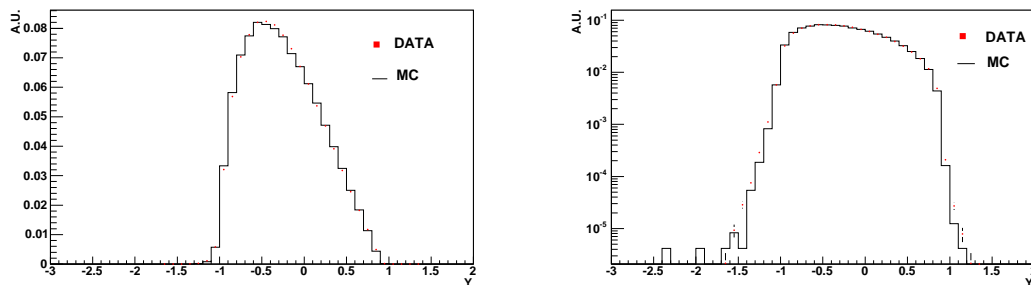


Figure 5.17: Data vs. MonteCarlo comparison for the Y variable. Left: linear scale. Right: log scale. The MonteCarlo histograms are normalized to the same number of events of the data sample.

The main source of backgrounds considered are:

1. $\phi \rightarrow \eta\gamma$ with $\eta \rightarrow \pi^+ \pi^- \pi^0$ and $\pi^0 \rightarrow e^+ e^- \gamma$;
2. $\phi \rightarrow \omega\pi^0$ with $\omega \rightarrow \pi^+ \pi^- \pi^0$;

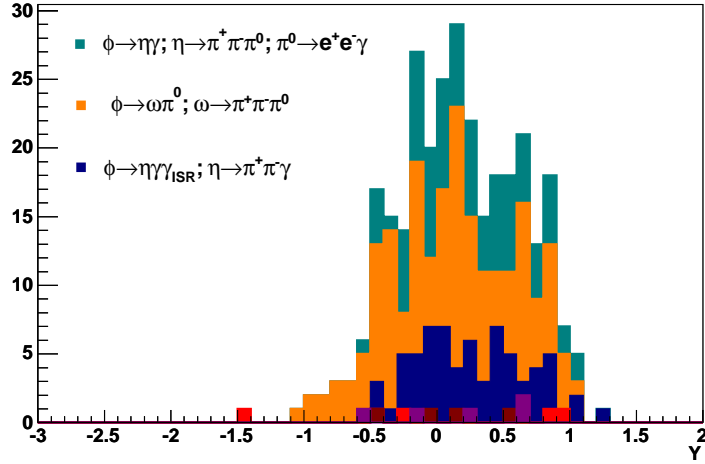


Figure 5.18: The different contributions to the background evaluation.

Fig.5.18 shows the estimated amount of these background at the final stage of this analysis. Special care has been devoted in understanding the dependence of background on the cut value for the variable $M_{\gamma\gamma}$ ³ where significant discrepancies in the tails are observed between data and MonteCarlo (see fig.4.3).

The different amounts of background (estimated from MonteCarlo) obtained changing the values of the cut are reported in tab.5.5.

$M_{\gamma\gamma}(\text{MeV}/c^2)$	$\frac{B}{S}(\%)$
<i>no cut</i>	0.7
$\in [80, 190]$	0.4
$\in [90, 180]$	0.4
$\in [100, 170]$	0.3
$\in [110, 160]$	0.3
$\in [115, 155]$	0.2
$\in [120, 150]$	0.2

Table 5.5: For different cuts applied on $M_{\gamma\gamma}$ the related background.

³ $M_{\gamma\gamma}$ is the invariant mass of the two softest photons in $\pi^+ \pi^- \gamma\gamma$ events.

In particular, $\frac{B}{S}$ ratio after the cut $M_{\gamma\gamma} \in [110, 160]$ improves of at least a factor 2, and the background in the region $Y < -1$ is totally rejected, see fig.5.19. Therefore we apply this cut to give the final fit results.

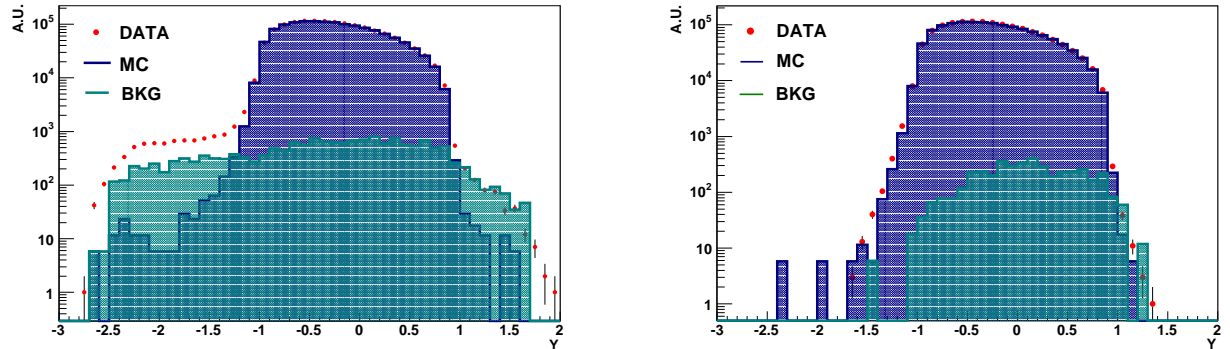


Figure 5.19: Data-MonteCarlo comparison for the Y distribution. Blue is the MC signal, red dots are the data and green is background. Left: before the cut $M_{\gamma\gamma} \in [110, 160]$. Right: after the cut $M_{\gamma\gamma} \in [110, 160]$.

We have estimated the Dalitz-plot parameters changing the values of the cut on $M_{\gamma\gamma}$, a summary of the results obtained is shown in tab.5.6.

	P_{χ^2}	a	b	d	f
(1)	82%	-1.084 ± 0.005	0.116 ± 0.006	0.050 ± 0.006	0.14 ± 0.01
(2)	82%	-1.086 ± 0.005	0.117 ± 0.006	0.052 ± 0.006	0.14 ± 0.01
(3)	75%	-1.087 ± 0.005	0.118 ± 0.006	0.053 ± 0.006	0.14 ± 0.01
(4)	74%	-1.090 ± 0.005	0.124 ± 0.006	0.057 ± 0.006	0.14 ± 0.01
(5)	71%	-1.091 ± 0.005	0.128 ± 0.006	0.060 ± 0.006	0.14 ± 0.01
(6)	58%	-1.089 ± 0.006	0.130 ± 0.006	0.064 ± 0.006	0.13 ± 0.01

Table 5.6: Results of the Dalitz plot fit after subtracting the background and for different cut on $M_{\gamma\gamma}$: (1) $M_{\gamma\gamma} \in [80, 190]$, (2) $M_{\gamma\gamma} \in [90, 180]$ (3) $M_{\gamma\gamma} \in [100, 170]$, (4) $M_{\gamma\gamma} \in [110, 160]$, (5) $M_{\gamma\gamma} \in [115, 155]$, (6) $M_{\gamma\gamma} \in [120, 150]$. The final fit results are in correspondence of (4).

Finally, for each parameter we quote as a systematic error due to the background evaluation the maximum and minimum spread between the different fits, see tab.5.7

a	b	d	f
-0.001 +0.006	-0.008 +0.006	-0.007 +0.007	-0.01

Table 5.7: For each of the fit parameters the systematic error due to the background subtraction is reported.

5.4.4 Effect of EVCL procedure

We have evaluated the systematic uncertainty induced by the EVCL procedure using a data sample of 23 pb^{-1} (Minimum Bias sample) selected as described in [63].

No bias in reproducing the shape of efficiency is introduced by EVCL procedure. The Dalitz plot distribution has been fitted both without requiring the EVCL procedure (i.e. using the full Minimum Bias sample) and requiring the EVCL tag, see tab.5.8.

	a	b	d	f
Minimum Bias and evcl	-1.050 ± 0.024	0.153 ± 0.027	0.057 ± 0.026	0.080 ± 0.054
Only Minimum Bias	-1.067 ± 0.024	0.158 ± 0.027	0.045 ± 0.025	0.090 ± 0.053

Table 5.8: Results of the Dalitz plot fit on Minimum Bias sample. Top: requiring the EVCL tag. Bottom: without requiring EVCL tag.

For each parameter, we quote as systematic uncertainty the difference among the two obtained values: this is due to the fact that since the two samples are 98.5% correlated, any difference between the two fits is statistically significant.

5.4.5 Time stability

We have checked the stability of the parameter values with respect to the data taking conditions.

We have checked both large scale uniformity and small scale uniformity.

On a *large scale* we have split the full data sample in 9 bunches of about 50 pb^{-1} each and repeated the fit procedure in order to estimate all parameters. The results, together with the fit to a constant function, are shown in fig. 5.20.

On a *small scale* the data sample has been split in subsamples of almost equal integrated luminosity, 5 pb^{-1} , and for each of these we have fitted the Dalitz plot distribution. Since we have low statistics in each sample we have fitted using a one dimensional fit procedure (see Appendix) where we are sensitive only to the linear and quadratic slopes in Y . For both parameters the time dependency is compatible with a constant function, see fig. 5.21.

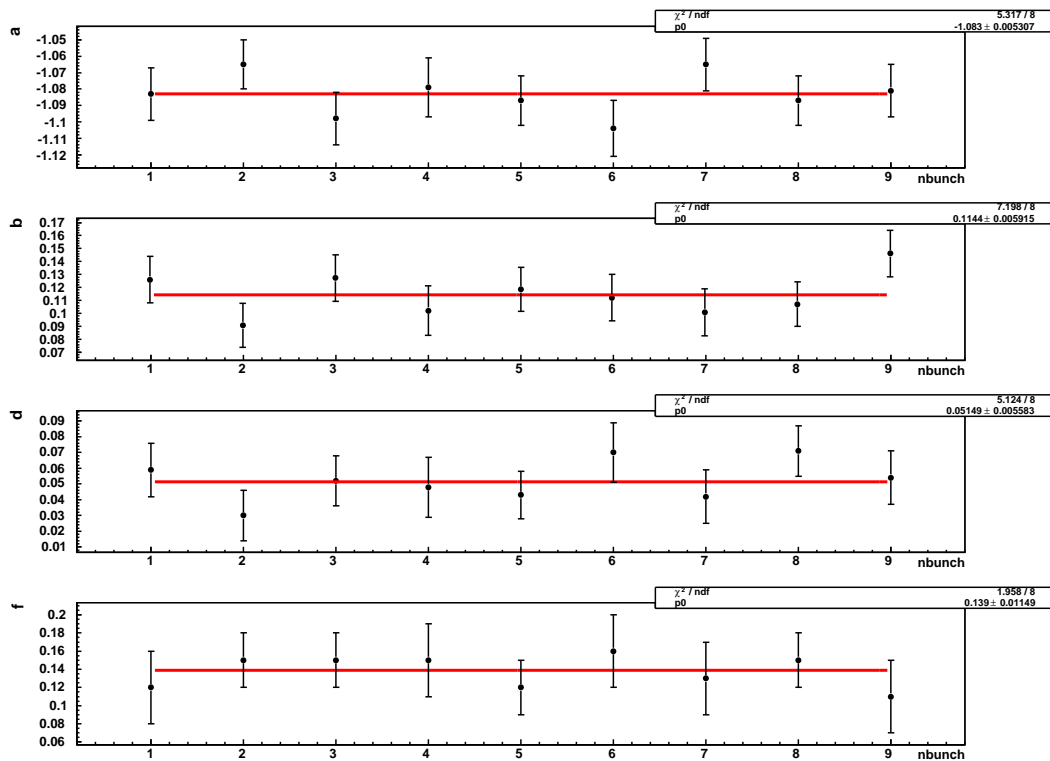


Figure 5.20: Fit parameters as function of time along data taking. The data sample has been split in subsample having the same integrated luminosity. The results of a fit with constant function is reported.

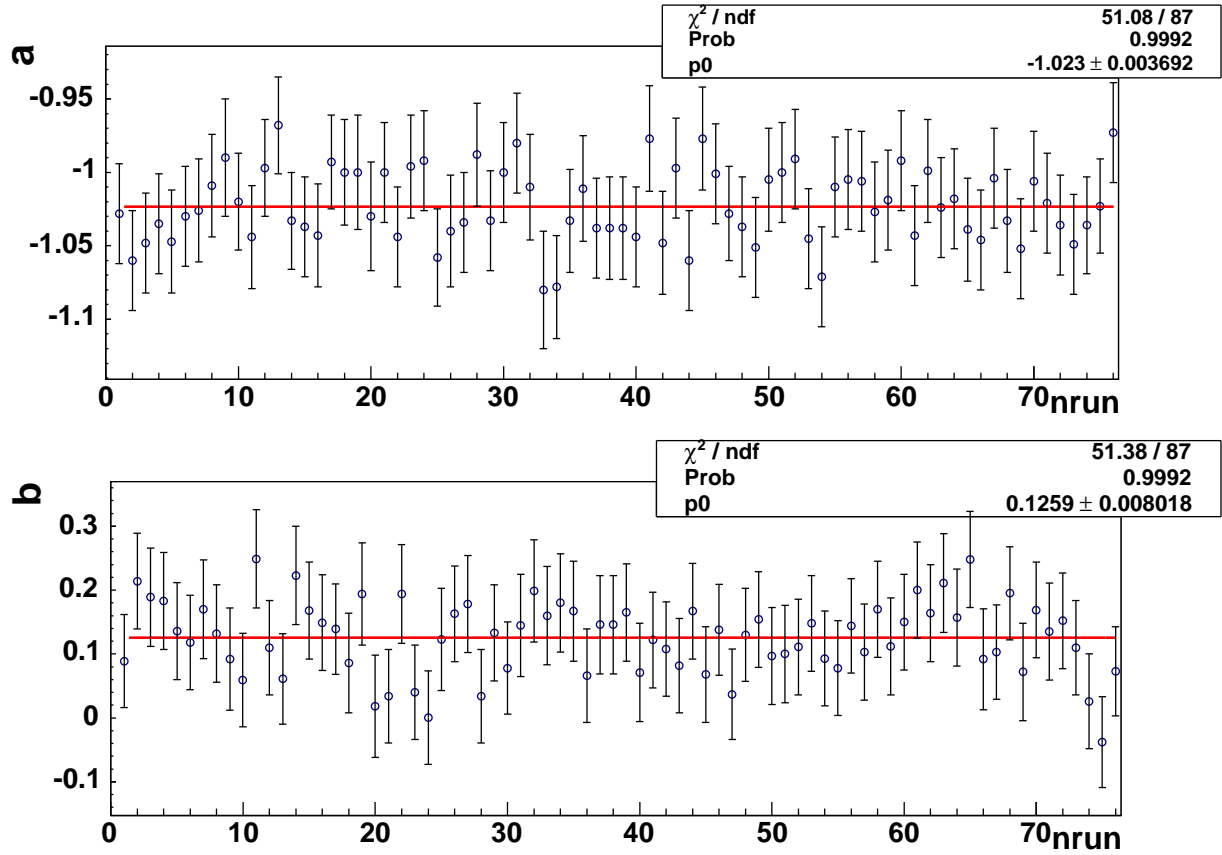


Figure 5.21: Behaviour of the linear and quadratic slopes in Y as function of the time. The data sample has been split in subsample having the same integrated luminosity. The results of a fit with constant function is reported.

5.4.6 Radiative correction

Finally we have studied also the possible effects of the radiative corrections in the final state to the Dalitz plot density. To include the radiative correction in the MonteCarlo simulation we have used a generator $\eta \rightarrow \pi^+ \pi^- \pi^0 \gamma$.

In fig.5.22 is shown the distribution of Dalitz plot for the events $\eta \rightarrow \pi^+ \pi^- \pi^0 \gamma$.

In order to obtain the corrections to the parameter values we have divided bin by bin the Dalitz plot distribution for the events $\eta \rightarrow \pi^+ \pi^- \pi^0$ and $\eta \rightarrow \pi^+ \pi^- \pi^0 \gamma$, (see fig.5.22). Fitting the obtained distribution with the usual expansion we find a negligible correction to the parameter values.

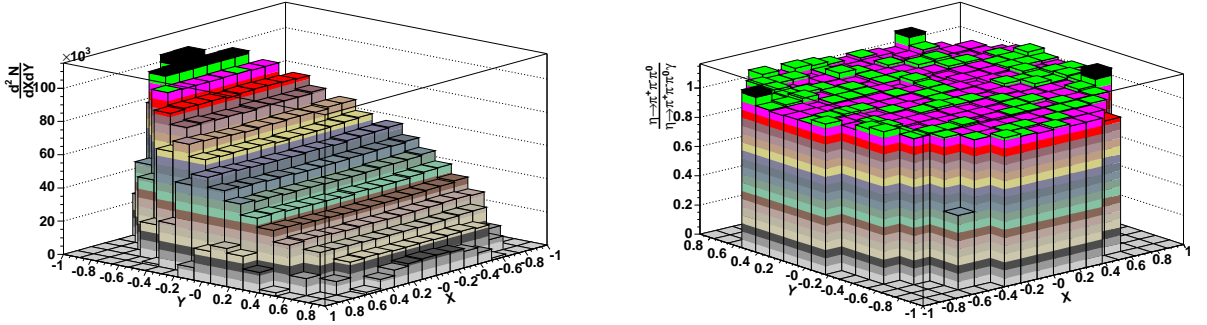


Figure 5.22: Left: Dalitz plot distribution for events $\eta \rightarrow \pi^+ \pi^- \pi^0 \gamma$. The plot contains 10.0 millions of events. Right: Bin by bin ratio of Dalitz distribution of $\eta \rightarrow \pi^+ \pi^- \pi^0$ and $\eta \rightarrow \pi^+ \pi^- \pi^0 \gamma$ events.

For each of the fit parameters a summary of the most relevant systematic errors are reported in tab. 5.3.

5.5 Results

The results including the statistical uncertainties coming from the fit and the estimate of systematics are:

$$a = -1.090 \pm 0.005(stat)_{-0.019}^{+0.008}(syst) \quad (5.13)$$

$$b = 0.124 \pm 0.006(stat) \pm 0.010(syst) \quad (5.14)$$

$$d = 0.057 \pm 0.006(stat)_{-0.016}^{+0.007}(syst) \quad (5.15)$$

$$f = 0.14 \pm 0.01(stat) \pm 0.02(syst) \quad (5.16)$$

Note that the systematic error has been obtained adding in quadrature all the con-

	a	b	d	f
a	1	-0.226	-0.405	-0.795
b		1	0.358	0.261
d			1	0.113
f				1

Table 5.9: Correlation matrix from the Dalitz-plot fit.

tributions in table 5.3.

Tab. 5.9 gives the correlation coefficients between the fitted parameters. In fig.5.23 are shown the normalized residuals as function of bin number.

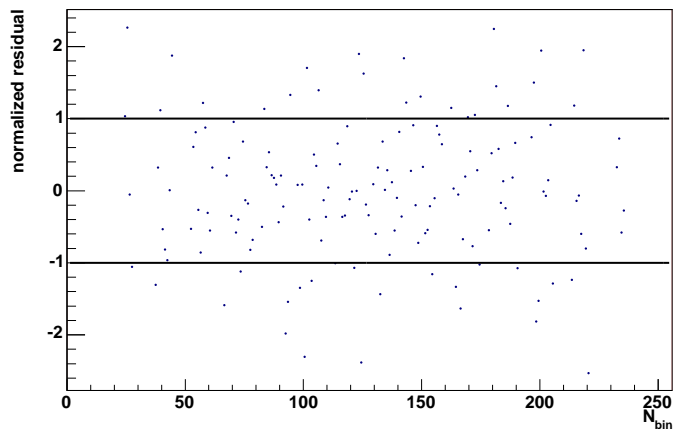


Figure 5.23: Distribution of the normalized residual. As expected, the residuals fluctuate around to the zero.

The following comments can be done:

- the fitted value for the quadratic slope in Y is almost one half of the simple Current algebra prediction ($b = a^2/4$) thus calling for important higher order corrections;
- the quadratic term in X is unambiguously found different from zero;
- the same applies for the unexpectedly large cubic term in Y ;

- the strong correlations between parameters imply that much care must be taken when integrating the polynomial over the phase space, since error propagation for the result must correctly take correlations into account;
- for the a , b , d parameters, which have not been measured here for the first time, we observe a reasonable agreement with the ones in literature, see fig. 5.5 especially taking into account that for all previous measurements only statistical errors were considered.

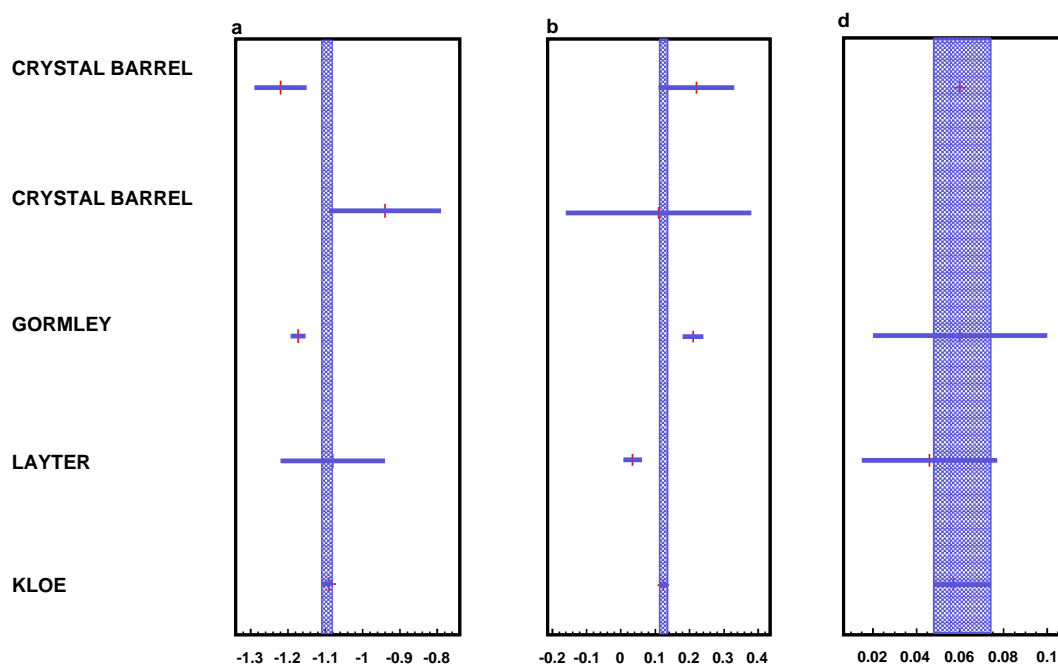


Figure 5.24: Comparison between the values of the Dalitz plot parameters obtained in the present analysis (solid squares) and in the measurements considered by the PDG [65] (red dots). In the plot the error on the parameters of this analysis has been obtained adding in quadrature the statistical and systematic error while for the other measurements only the statistical error is reported.

Conclusions

In this thesis, a precise measurement of the $\eta \rightarrow \pi^+ \pi^- \pi^0$ dynamics via the study of Dalitz plot density distribution has been presented.

Usually for a 3 body decay the Dalitz plot distribution is described in terms of two variables $X \propto T_+ - T_-$ and $Y \propto T_0$ (where T is the kinetic energy of pions in the η -rest frame) and it is parametrized as following:

$$|A(X, Y)|^2 = 1 + aY + bY^2 + cX + dX^2 + eXY + fY^3$$

A MonteCarlo sample has been used to tune the definitions of the selection criteria applied in the analysis and to give an estimate of the background contamination in the selected sample.

The efficiency as function of Dalitz plot variables is almost flat in the kinematically allowed region and its mean value is about 34.50%; while the background is at level of 0.25 per mill.

The fit to the Dalitz plot is done using a least squares approach. The procedure tested on MonteCarlo allows to find correctly the MonteCarlo input parameters independently from the number of degrees of freedom.

In order to obtain a measurement of the slope parameters the 2001–2002 KLOE statistics, corresponding to about 1.3 millions of $\eta \rightarrow \pi^+ \pi^- \pi^0$ events in the Dalitz plot, is analyzed.

A complete study of systematic uncertainties, including the effect of resolution, efficiency and background on the parameter estimations, has been achieved. The results are:

$$a = -1.090 \pm 0.005(stat)_{-0.019}^{+0.008}(syst) \quad (5.17)$$

$$b = 0.124 \pm 0.006(stat) \pm 0.010(syst) \quad (5.18)$$

$$d = 0.057 \pm 0.006(stat)_{-0.016}^{+0.007}(syst) \quad (5.19)$$

$$f = 0.14 \pm 0.01(stat) \pm 0.02(syst) \quad (5.20)$$

We clearly observe a quadratic slope in X and a cubic slope in Y never measured before; all the other cubic terms different from f are zero.

According to the C-invariance in the $\eta \rightarrow \pi^+ \pi^- \pi^0$ decay, the parameter c and e are consistent with the zero and they are removed from the fit without affecting the other parameter values.

For the a, b, d parameters, which have not been measured here for the first time, a reasonable agreement with the ones in literature is observed.

Appendix

The kinematic fit

A kinematic fit to the observed variables has been performed to improve the resolution and to suppress the background. Indeed the χ^2 of the fit can be used to cut away events that simulated the signal but have different features.

The kinematic fit procedure is based on the minimisation of the least squares function:

$$X^2 = \sum_{i=1}^N \frac{(P_i - P_i^{meas})^2}{\sigma_i^2}$$

where P_i^{meas} are the measured values for the parameters. The minimum of this function is expected to be distributed as a χ^2 function.

The minimisation is performed using Lagrange multipliers procedure, which allows us to find a constrained minimum for a function. We minimise with an iterative procedure the function:

$$Y^2 = \sum_{i=1}^N \frac{(P_i^k - P_i^{meas})^2}{\sigma_i^2} + \sum_{j=1}^M \lambda_j^k C_j(P_1^k \dots P_N^k)$$

where k is the iteration index and the λ_j 's are the M additional parameters, the Lagrange multipliers, used to insure that the minimum is found with the $P_1 \dots P_N$ parameters lying on the hyper surface defined by the M conditions (5.5):

$$C_j(P_1 \dots P_N) = 0 \quad \forall j = 1, \dots, M$$

The starting values for the fit P_i^0 are the measured values P_i^{meas} .

The number of degrees of freedom for this kind of fit is equal to the number of

constraints because the number of measured quantities is exactly equal to the number of parameters; $N_{dgf} = (\#of\ measured\ quantities) - [(\#of\ parameters) - (\#of\ constraints)] = N - (N - M) = (\#of\ constraints)$.

In the $\eta \rightarrow \pi^+ \pi^- \pi^0$ decay we have a charged vertex and three photons in the final state. The parameters used in the fit procedure are the following:

- Energy, time, and position for each photon:
 - 5 parameters for each photon;
- Curvature, ϕ angle and $\cot \theta$ for each pion track:
 - 2×3 parameters
- Position of the charged vertex:
 - 3 parameters
- Beams energies:
 - 2 parameters

for a total of $N = 26$ parameters.

The errors on these parameters are assigned as follows:

- $\sigma_E^{clu} = 5\% / \sqrt{E(\text{GeV})}$
- $\sigma_t^{clu} = 50\text{ps} / \sqrt{E(\text{GeV})}$
- $\sigma_{xy}^{clu} = 1.2\text{ cm}$
- $\sigma_z^{clu} = 1.2\text{ cm} / \sqrt{E(\text{GeV})}$
- σ_{Curv} , $\sigma_{\cot \theta}$, σ_ϕ are the square roots of the diagonal elements of the track fit covariance matrix after vertex fit
- $\sigma_{x,y,z}$ of the vertex are the square roots of the vertex fit covariance matrix diagonal elements
- $\sigma_E^{beam} = 0.7\text{ MeV}$ are the nominal spread in the beam energy of DAΦNE

The constraints applied are:

- $c \cdot t - d = 0 \quad \forall$ photons
 - 3 constraints for the two tracks and three photons final states.

- Total four momentum conservation
 - 4 constraints

No other constraints are imposed.

One dimensional fit procedure

In this appendix we show the one dimensional fit procedure.

Let $|A(Y)|^2 \simeq 1 + aY + bY^2$ the amplitude of decay in which we have neglected every dependency from X . In general, the density of points in the Dalitz-plot is proportional to the square of the invariant matrix element for the decay, then one has:

$$|A(Y)|^2 = \frac{\sum_{N_{binx}} \frac{N(X,Y)}{\varepsilon(X,Y)}}{\int_{phase\ space} dx}$$

where

- $N(X, Y)$ are the number of events in the Dalitz-plot,
- $\varepsilon(X, Y)$ is the efficiency as function of Dalitz-plot,

and when summing over X bins we have applied a phase space correction.

Thus, fitting the eq.5.5 with a polynomial we obtain an estimate of the parameters.

In fig.5.25 are shown the results of fit with two different parametrization.

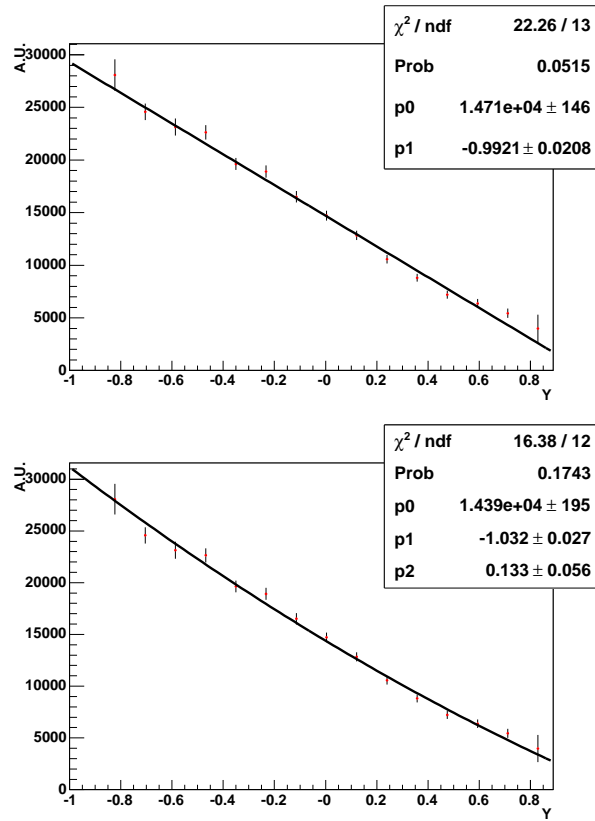


Figure 5.25: Results of fit to the Dalitz-plot density. Top: $|A(Y)|^2 \simeq N_0(1 + aY)$. Bottom: $|A(Y)|^2 \simeq N_0(1 + aY + bY^2)$.

List of Tables

1.1	Branching ratio of principal decays of ϕ [65].	4
2.1	Theoretical results for the slope parameters of the various approximations. . . .	41
2.2	Experimental results for the slope parameters.	41
4.1	Correlation matrix from the Dalitz-plot fit.	70
5.1	Results of the fit for different parametrizations of $ A ^2$ and for a total of bins $N_{bin}^{eff} = 80$ corresponding to linear dimensions of bins equal to $\Delta X = \Delta Y = 0.17$	76
5.2	Results of the fit for different parametrizations of $ A ^2$ and for a total of bins $N_{bin}^{eff} = 154$ corresponding to linear dimensions of bins equal to $\Delta X = \Delta Y = 0.13$	78
5.3	For each of the fit parameters a summary of the systematic errors.	84
5.4	For each of the fit parameters the maximum and minimum spread in the region $N_{bin}^{eff} \in [54, 202]$ or $\Delta X = \Delta Y \in [0.20, 0.11]$ is reported.	86
5.5	For different cuts applied on $M_{\gamma\gamma}$ the related background.	94
5.6	Results of the Dalitz plot fit after subtracting the background and for different cut on $M_{\gamma\gamma}$: (1) $M_{\gamma\gamma} \in [80, 190]$, (2) $M_{\gamma\gamma} \in [90, 180]$, (3) $M_{\gamma\gamma} \in [100, 170]$, (4) $M_{\gamma\gamma} \in [110, 160]$, (5) $M_{\gamma\gamma} \in [115, 155]$, (6) $M_{\gamma\gamma} \in [120, 150]$. The final fit results are in correspondence of (4).	95
5.7	For each of the fit parameters the systematic error due to the background subtraction is reported.	96
5.8	Results of the Dalitz plot fit on Minimum Bias sample. Top: requiring the EVCL tag. Bottom: without requiring EVCL tag.	96
5.9	Correlation matrix from the Dalitz-plot fit.	100

List of Figures

1.1	A sketch of the DAΦNE complex at the Laboratori Nazionali di Frascati of I.N.F.N.	8
1.2	Integrated luminosity in pb^{-1} as function of the number of days of data taking for the years 2001 ÷ 2005.	9
1.3	Section of the KLOE detector	10
1.4	A detail of the configuration of the drift cell at $z = 0$, in a region between the small cells and the big ones. The empty circles represent the field wires, full dots are the sense wires.	11
1.5	Photograph of the KLOE drift chamber after assembly and stringing.	12
1.6	Momentum resolution as function of polar angle	12
1.7	Software (left) and hardware (right) efficiencies as functions of the drift distance.	13
1.8	A picture of the KLOE electromagnetic calorimeter before inserting the drift chamber.	14
1.9	Schematic view of the fiber-lead modules in the KLOE electromagnetic calorimeter.	15
1.10	Up: plot of $(E_{clu} - E_\gamma)/E_\gamma$ for radiative Bhabha events. Down: energy resolution $\sigma(E)/E$. The solid line is the fit to the usual $a/\sqrt{E(\text{GeV})} + b$ parametrization.	16
1.11	Time resolution versus the photon energy E_γ for radiative ϕ decays.	17
1.12	Photon detection efficiency versus the photon energy E_γ , for radiative Bhabha, $\phi \rightarrow \pi^+ \pi^- \pi^0$ and $K_L \rightarrow \pi^+ \pi^- \pi^0$ events.	18
1.13	Logic scheme of a trigger sector.	20
1.14	The architecture of the Data Acquisition System.	22

2.1	Bounds on X and Y from $SU(3)$ calculations and experimental branching fractions. The three constraints: $\frac{\Gamma(\eta' \rightarrow \gamma\gamma)}{\Gamma(\pi^0 \rightarrow \gamma\gamma)}$, $\frac{\Gamma(\eta' \rightarrow \rho\gamma)}{\Gamma(\omega \rightarrow \pi^0\gamma)}$, $\frac{\Gamma(\phi \rightarrow \eta'\gamma)}{\Gamma(\phi \rightarrow \eta\gamma)}$	28
2.2	Left: $m_{\gamma\gamma}$ distribution used to determine the background content; Right: $m_{4\gamma}$ distribution: DATA, dots with error bars, MC signal and MC background are normalised according the fit result.	30
2.3	Left: Dalitz plot of the 3γ final state, the cut chosen to reject background is shown, Right: $m_{\gamma\gamma}$ distribution.	31
2.4	η mass measurement in the several periods. The systematic band, red rectangle, is shown.	32
2.5	Relevant phase-space for the decay $\eta \rightarrow \pi^+ \pi^- \pi^0$	40
3.1	Event Classification block scheme.	48
3.2	Scatter-plot of δE vs. P_Σ for $\pi^+\pi^-\gamma$, $\mu^+\mu^-\gamma$ and $e^+e^-(\gamma)$ events. The MC generation of $\pi^+\pi^-\gamma$ and $\mu^+\mu^-\gamma$ is done only for events with $E_\gamma < 100$ MeV, so the 2 bands are clearly artificially cut. The low P_Σ tail of $\pi^+\pi^-\gamma$ events is due to $\rho^\pm\pi^\pm$ where $\rho^\pm \rightarrow \pi^\pm\gamma$ that are included in the $\pi^+\pi^-\gamma$ sample.	50
3.3	Scatter-plot of δE vs. P_Σ for $\eta\gamma$, $a_0\gamma$ and $\eta'\gamma$ events. The allowed area for radiative decays are shown. The second area for the $\eta'\gamma$ case partly overlaps the 3-pion area.	51
4.1	MonteCarlo photon energy spectrum. Left: linear scale; Right: log scale.	56
4.2	χ^2 distribution. Left: linear scale; Right: log scale.	57
4.3	Data vs MonteCarlo comparison for the invariant mass of the two softest photons in $\pi^+\pi^-\gamma\gamma\gamma$ events. Left: linear scale; Right: log scale. The arrows show the cut applied. The histograms are normalized to the same area.	58
4.4	Trigger sector multiplicity. From top to bottom: endcap East, endcap West, barrel. Left: linear scale. Right: log scale.	59
4.5	Left: Tracking (upper plot) and Vertex (lower plot) efficiency as function of minimum P_T of the two tracks. Right: Data (blue) MonteCarlo (red) ratio for the tracking (upper plot) and vertex (lower plot) efficiencies.	61
4.6	MonteCarlo distributions of resolutions: X (left) and Y (right). The curves are fitted to a sum of four gaussians.	63
4.7	MonteCarlo distributions of resolutions: Y_{ch} (left) and Y_M (right). The curves are fitted to a sum of four gaussians.	63

4.8	Data (continuous line) vs. MonteCarlo (shaded line) comparison for the variable $Y_{ch} - Y_0$. The curves are fitted to a sum of two gaussians with the same mean. The shift of ~ 1.33 MeV is estimated from the difference between the mean value of the two fitting functions.	64
4.9	Distribution of the invariant mass of three pions system ($\pi^+ \pi^- \pi^0$) for the data sample used in this analysis. The arrows show the range of fit. Right: A zoom of the region of the fit.	65
4.10	The invariant mass of the two softest photons in $\pi^+ \pi^- \gamma\gamma\gamma$ events. Left: Data distribution. Right: MonteCarlo distribution.	65
4.11	Data (continuous line) vs. MonteCarlo (shaded line) comparison for the variable $Y_{ch} - Y$ with the corrected value of M_η . Left: linear scale. Right: log scale. The shift of ~ 0.03 MeV is estimated from the difference between the mean value of the two fitting functions. The arrows show the position of the cut eq: (4.15)	66
4.12	Smearing matrix distribution. Left: X variable; Right: Y variable.	67
4.13	Efficiency as function of Dalitz-plot, before (left) and after (right) removing the bins crossed by Dalitz-plot contour.	68
4.14	Left: Efficiency versus X . Right: Efficiency versus Y	68
4.15	Results of the Dalitz-plot fit for different ndf . The results refer to a parametrization for the decay amplitude $ A(X, Y) ^2 \simeq 1 + aY + bY^2 + cX + dX^2 + eXY$. The MonteCarlo input parameters are pointed out with the straight line.	71
4.16	Results of the Dalitz-plot fit for different ndf . The results refer to a parametrization for the decay amplitude $ A(X, Y) ^2 \simeq 1 + aY + bY^2 + dX^2$. The fit is performed by setting to zero the parameter values c and e . The MonteCarlo input parameters are pointed out with the straight line.	72
5.1	Dalitz-plot distribution observed on whole data sample. The plot contains 1.39 millions of events in 256 bins.	74
5.2	Results of the Dalitz-plot fit for different values of ndf . The results refer to a parametrization for the decay amplitude $ A(X, Y) ^2 \simeq 1 + aY + bY^2 + cX + dX^2 + eXY$	75
5.3	Results of the Dalitz-plot fit on the Monte Carlo improved simulation for different values of ndf . The results refer to a parametrization for the decay amplitude $ A(X, Y) ^2 \simeq 1 + aY + bY^2 + cX + dX^2 + eXY$. The horizontal lines show the values used as input for the simulation.	77

- 5.4 Results of the Dalitz-plot fit for different ndf . The results refer to a parametrization for the decay amplitude $|A(X, Y)|^2 \simeq 1 + aY + bY^2 + cX + dX^2 + eXY + fY^3$. 79
- 5.5 In correspondence of $N_{bin}^{eff} = 154$ a comparison between data and fitted function, $|A(X, Y)|^2 \simeq 1 + aY + bY^2 + cX + dX^2 + eXY + fY^3$, as a function of the bin number. The observed structure corresponds to Y distributions corresponding to slices in X . Blue points are data and the histogram is the function. 80
- 5.6 In correspondence of $N_{bin}^{eff} = 154$ a comparison between data and fitted function, $|A(X, Y)|^2 \simeq 1 + aY + bY^2 + cX + dX^2 + eXY + fY^3$, as a function of Dalitz plot variables. Left: X variable. Right: Y variable. Blue points are data and the histogram is the function. 81
- 5.7 Data vs. MonteCarlo discrepancy bin by bin normalized as function of P_T . With full circles (open circles) efficiency weighed using parameters from eq. 5.10 (not weighed). Left: π^+ tracks. Right: π^- tracks. 82
- 5.8 Data vs. MonteCarlo discrepancy bin by bin normalized as function of P_T . With full circles (open circles) efficiency weighed using parameter γ (not weighed). Left: π^+ tracks. Right: π^- tracks. 83
- 5.9 Left: distribution of the mean of the gaussian fit to $\frac{\Delta E}{E}$ as a function of E_{true}^γ . Right: distribution of the sigma of the gaussian fit to $\frac{\Delta E}{E}$ as a function of E_{true}^γ 85
- 5.10 Distribution of the rms in bins of E_{true}^γ 86
- 5.11 Data vs MonteCarlo comparisons. From top to bottom: P_T, P_Z for π^+ and P_T, P_Z for π^- . Left: linear scale. Right: log scale. 88
- 5.12 Data vs MonteCarlo comparisons. From top to bottom: minimum P_T and P_Z , $\cos \theta$ between pion tracks and E_γ for photons. Left: linear scale. Right: log scale. 89
- 5.13 Bin by bin normalized Data-MC discrepancy. The MonteCarlo histograms are normalized to the same number of events of the data sample. From top to bottom: P_T , for π^+ and π^- , minimum P_T 90
- 5.14 Bin by bin normalized DATA-MC discrepancy. The MonteCarlo histograms are normalized to the same number of events of the data sample. From top to bottom: P_Z for π^+ and π^- , | minimum P_Z |. 91
- 5.15 Bin by bin normalized Data-MC discrepancy. The MonteCarlo histograms are normalized to the same number of events in the data sample. From top to bottom: $\cos \theta$ between pion tracks, E_γ for photons and E_γ for photons with the fit to the Fermi-Dirac function superimposed. 92

5.16	Ratio between weighed and not weighed efficiencies as function of X (Left) and Y (Right). The errors take into account the correlations between the efficiencies. . .	93
5.17	Data vs. MonteCarlo comparison for the Y variable. Left: linear scale. Right: log scale. The MonteCarlo histograms are normalized to the same number of events of the data sample.	93
5.18	The different contributions to the background evaluation.	94
5.19	Data-MonteCarlo comparison for the Y distribution. Blue is the MC signal, red dots are the data and green is background. Left: before the cut $M_{\gamma\gamma} \in [110, 160]$. Right: after the cut $M_{\gamma\gamma} \in [110, 160]$	95
5.20	Fit parameters as function of time along data taking. The data sample has been split in subsample having the same integrated luminosity. The results of a fit with costant function is reported.	97
5.21	Behaviour of the linear and quadratic slopes in Y as function of the time. The data sample has been split in subsample having the same integrated luminosity. The results of a fit with costant function is reported.	98
5.22	Left: Dalitz plot distribution for events $\eta \rightarrow \pi^+ \pi^- \pi^0 \gamma$. The plot contains 10.0 millions of events. Right: Bin by bin ratio of Dalitz distribution of $\eta \rightarrow \pi^+ \pi^- \pi^0$ and $\eta \rightarrow \pi^+ \pi^- \pi^0 \gamma$ events.	99
5.23	Distribution of the normalized residual. As expected, the residuals fluctuate around to the zero.	100
5.24	Comparison between the values of the Dalitz plot parameters obtained in the present analysis (solid squares) and in the measurements considered by the PDG [65] (red dots). In the plot the error on the parameters of this analysis has been obtained adding in quadrature the statistical and systematic error while for the other measurements only the statistical error is reported.	101
5.25	Results of fit to the Dalitz-plot density. Top: $ A(Y) ^2 \simeq N_0(1 + aY)$. Bottom: $ A(Y) ^2 \simeq N_0(1 + aY + bY^2)$	108

Bibliography

Bibliography

- [1] A. Aloisio *et al.*, *A general purpose detector for DAΦNE* , LNF-92/019(IR) (1992).
- [2] A. Aloisio *et al.*, *The KLOE detector. Technical Proposal*, LNF-93/002(IR) (1993).
- [3] M. Gell-Mann and A. Pais, *Phys. Rev.* **97** (1955) 1387.
- [4] J.H. Christenson, J.W. Cronin, V.L. Fitch and R. Turlay, *Phys. Rev. Lett.* **13** (1964) 138.
- [5] L.K. Gibbons *et al.*, *Phys. Rev. Lett.* **70** (1993) 1203.
- [6] G.D. Barr *et al.*, *Phys. Lett.* **317** (1993) 233.
- [7] A. Alavi-Harati *et al.*, *Phys. Lett.* **83** (1999) 22.
- [8] NA48 Collaboration, “*A precise measurement of the direct CP violation parameter $\Re(\epsilon'/\epsilon)$* ”, *Eur. Phys. J.* **C22**, (2001) 231.
- [9] L. Maiani and N. Paver, “*The second DAΦNE Physics handbook*” , I.N.F.N. L.N.F. (1995) 51.
- [10] A. Aloisio *et al.*, *Measurement of $\sigma(e^+e^- \rightarrow \pi^+\pi^-\gamma)$ and extraction of $\sigma(e^+e^- \rightarrow \pi^+\pi^-)$ below 1-GeV with the KLOE detector*, *Phys.Lett.* **B606**, 12-24 (2005).
- [11] A. BURAS *et al.*, *MPI Preprint*.
- [12] G. Isidori, L. Maiani, A. Pugliese *Preprint*, 848, Roma (1991).

- [13] M. Adinolfi *et al.* “*The QCAL tile calorimeter of KLOE*”, *Nucl. Inst. Meth. A* **483** (2002) 649.
- [14] M. Adinolfi *et al.* “*The KLOE drift chamber*”, *Nucl. Inst. Meth. A* **461** (2002) 25.
- [15] M. Adinolfi *et al.* “*The KLOE electromagnetic calorimeter*”, *Nucl. Inst. Meth. A* **482** (2002) 363-385.
- [16] M. Adinolfi *et al.* “*The Trigger of KLOE*”, *Nucl. Inst. Meth. A* **492** (2002) 134.
- [17] M. Adinolfi *et al.* “*Data acquisition and monitoring for the KLOE detector*”.
- [18] J. Goldstone, A. Salam, S. Weinberg, *Phys.Rev.* **127**, 965 (1962).
- [19] J.D.Bjorken S.D.Drell, *Relativistic Quantum Mechanics*, McGraw-hill, NewYork, (1964).
- [20] S. Gasiorowicz and D.A. Geffen, *Rev. Mod. Phys.* **41**, 531 (1969).
- [21] M. Gell-Mann, CalTech Rept. **CTSL-20** (1961); S. Okubo, *Prog. Theo. Phys.* **27** (1962) 949.
- [22] S. Weinberg, *Physica* **A96** (1979) 327.
- [23] J. Gasser and H. Leutwyler, *Ann. Phys. (NY)*, **158**, 142 (1984); *Nucl. Phys.* **B250**, 465 (1985).
- [24] S. Bertolucci *et al.* “*The LADON test beam of EMCAL:A full report on the data analysis*”, KLOE Note **62** (1993) .
- [25] <http://www-cdf.fnal.gov/offline/ybos/ybos.html>, Fermilab CDF library.
- [26] The Argus Collaboration, *ARGUS: a Universal Detector at DORIS II*, *Nucl. Inst. & Meth.* **A275**, 1-48 (1989).
- [27] Kapitza *Track Fitting at ARGUS*, (1992), not published.
- [28] F. Ambrosino *et al.* *Description of the track fit procedure using the drift chamber of the KLOE experiment* , KLOE memo 141, 1998.

- [29] F. Ambrosino *et al.* *Current status of the track reconstruction using the KLOE drift chamber* KLOE memo 177, 1999.
- [30] G. Venanzoni *Description of the procedure joining the tracks which have been split by the pattern recognition program during the track reconstruction with the KLOE Drift Chamber* Kloe memo 143, 1998.
- [31] F. Ambrosino, C. Di Donato, G. Saracino *Kink identification in the KLOE Drift Chamber track fit*, KLOE memo 151, 1998.
- [32] M. Incagli *VTXFIN: the KLOE vertex finding algorithm* KLOE memo 147, 1998.
- [33] F. Ambrosino *et al.* *The event classification procedures* KLOE memo 225.
- [34] M. Moulson, S. Muller *FILFO revisited: A new look at the offline reconstruction filter and event classification*", KLOE memo 288, 2004.
- [35] G. Finocchiaro, A. Menicucci, "Cosmic rays rejection in KLOE" KLOE memo 203. **33**, (2006).
- [36] F. E. Close: *The DAΦNE physics handbook vol. II*, ed. L. Maiani, G. Pancheri and N. Paver, Frascati 1992.
- [37] A. Bramon, R. Escribano, M.D. Scadron, Eur. Phys. J. C7 (1999) 271.
- [38] A. Bramon, R. Escribano and M.D. Scadron, Phys. Lett. **B 503**, 271 (2001)
- [39] C. Bloise *et al.*, ACTA Phys.Slov.**56**, 341-344, 2005.
- [40] S.Eidelman *et al.* Phys. Lett. **B 592**, 2004, 1.
- [41] Alde *et al.* Z. Phys. **C 25**, 225, 1984.
- [42] S. Prakhov *et al.* Phys. Rev.**C 72**, 025201, 2005.
- [43] Knecht *et al.* Phys. Lett.**B 589**, 14, 2005.
- [44] E. Oset, J. R. Peláez, L. Roca Phys. Rev.**D 67**, 073013, 2003.
- [45] L. Ametller, J. Bijnens, A. Bramon, F. Cornet Phys. Lett. **B 276**, 185, 2002.

- [46] M. Abdel-Bary *et al.* Phys. Lett. **B 619**, 281, 2005.
- [47] A. Lai *et al.* Phys. Lett. **B 533**, 196, 2002.
- [48] D.G. Sutherland, Phys.Lett. **23**, 384 (1966)
- [49] R. Baur, J. Kambor and D. Wyler Nucl. Phys. **B460**, 127 (1966)
- [50] J. Bijnens and J. Gasser, Physica Scripta **T99**, 34 - 44 (2002)
- [51] R. Dashen, Phys.Rev. **183**, 1245 (1969).
- [52] B. Holstein, Physica Scripta **T99**, 55 - 67, (2002)
- [53] J. Gasser and H. Leutwyler, Ann.Phys.(NY) **150** 142, (1984); Nucl.Phys.**B250** 465, (1985).
- [54] J. Kambor, C. Wiesendanger and D. Wyler, Nucl.Phys. **B465**, 215 (1996).
- [55] J.G. Layter *et al.*, Phys.Rev. **D7**, 2565 (1973).
- [56] M. Gormley *et al.*, Phys.Rev **D2**, 501 (1970).
- [57] Crystal Barrel Collaboration, Phys.Lett. **B346**, 203 (1995).
- [58] Crystal Barrel Collaboration, Phys.Lett. **B417**, 197 (1998).
- [59] F. Ambrosino *et al.*, KLOE memo 225 (2000).
- [60] M. Adinolfi *et al.*, [KLOE Collaboration] Nucl. Instrum. Meth. **A461**, 344 (2001)
- [61] M. Martini, S. Miscetti, KLOE memo 303 (2005).
- [62] F. Ambrosino, KLOE note 179 (2002).
- [63] C. Di Donato, KLOE memo 306 (2005).
- [64] C. Di Donato, KLOE memo 327 (2006).
- [65] K. Hagiwara, *et al.*, *J. Phys. G: Nucl. Part. Phys.* **33**, (2006).
- [66] M. Dreucci , “*Phi lineshape*” presented at KLOE workshop, Capri (2003).

- [67] S. Giovannella, S. Miscetti, KLOE note 177 (2002).
- [68] Physica Scripta T99, 140 - 142, (2002)